U-Pb geochronology and REE geochemistry of the pulsed Cretaceous magmatism in High Arctic Canada: implications for lithospheric evolution and magma genesis

by

David Michael Dockman

A thesis submitted in partial fulfillment of the requirements for the degree of

Master of Science

Department of Earth and Atmospheric Sciences
University of Alberta

Abstract

Cretaceous magmatism in the Sverdrup Basin of Arctic Canada consists of alkalic and tholeiitic phases that are widely considered to be part of the circum-Arctic High Arctic large igneous province (HALIP). The emplacement of large igneous provinces is commonly attributed to mantle plumes. However, recent studies have questioned the validity of a plume model for the HALIP, as well as questioned whether the younger magmatic phases of the province should be included as part of the same LIP. A paucity of U-Pb ages of mafic intrusions and robust Ar/Ar ages has hindered tectonomagmatic interpretations of this geographically remote province.

This study presents new major- and trace-element geochemical data plus Sr-Nd isotope systematics for mafic intrusions and lavas collected from Ellesmere and Axel Heiberg Islands, accompanied by new U-Pb and Ar/Ar ages to better constrain the temporal evolution of the HALIP and the controls on its magma chemistry. After accounting for the effects of crustal contamination, Sr-Nd isotope systematics indicate that tholeiitic and alkalic magmas are derived from similar mantle sources, with no evidence for the input of enriched lithospheric mantle. Therefore, variations in REE geochemistry between the two magma types are interpreted as being primarily controlled by differences in the lithospheric 'lid' thickness. REE inversion modeling revealed a bimodal distribution in 'lid' thickness (65 ± 5 and 45 ± 4 km). Correlation of magma chemistry with regional structural analysis indicates that the production and emplacement of alkalic and tholeiitic magmas are spatially segregated by the tectonic domains of the Sverdrup Basin.

Six U-Pb and four Ar/Ar ages obtained in the present study range from 122 ± 2 Ma to 78.5 ± 1.8 Ma, within the range of previously published results for the HALIP. The U-Pb ages are the first reported on mafic intrusive sheets on Axel Heiberg and Ellesmere Islands, including two coincident age determinations at ~117 Ma, which is an age that previous studies have yet to report. In addition, the discovery of a xenocrystic zircon, within a diabase intrusive, that crystallized from a mafic melt at 184.6 ± 1.8 Ma documents the first reported evidence of

Jurassic magmatism in the Sverdrup Basin. These new age results, combined with all modern (post-2000) published ages, detail a >50 Myr duration of magma emplacement that occurred in at least three pulses, around 122 Ma, 95 Ma, and 81 Ma, with gaps of 21 and 6 Myr between pulses.

We suggest that the ~122 Ma pulse, which is exclusively tholeiitic, may be primarily plume-generated and should be correlated to the other circum-Arctic tholeiites within the HALIP. However, in the younger magmatism, the contemporaneous production of alkalic and tholeiitic magmas, their spatial distribution, and the periodicity of the last two pulses (~95 and 81 Ma) indicate that alternating modes of edge-driven mantle convection (EDC) might be the primary control on magma genesis. A distal plume could intensify EDC magma production, but the influence of a mantle plume on the ~95 and 81 Ma pulses would be secondary to EDC and thus these younger magmas should not be considered part of the HALIP.

Acknowledgements

This study was funded through a Canada Excellence Research Chair award to Dr. Pearson as well as a substantial grant from NRCan through the Geo-mapping for Energy and Minerals (GEM II) initiative. The Canadian Foundation for Innovation and GEM II funded the instrumentation used in this study. The 2013 field expedition to Axel Heiberg and Ellesmere Islands was partially supported by CASP (formerly the Cambridge Arctic Shelf Program), who also donated a previously collected sample suite. I thank the Polar Continental Shelf Program for helicopter support and the Eureka Weather Station for their logistical support and accommodation.

I would like to thank my supervisor, Graham Pearson, for his mentorship, feedback, and support. Our meetings were collaborative and insightful; I appreciate all the time and effort you invested into all stages of this project. This thesis would not have been possible without Larry Heaman, who was enthusiastic about the sample set from the start, who provided endless hours of training on the techniques of Zr-bearing mineral analysis, and who was always available when I needed input. I would also like to thank Sally Gibson, of the University of Cambridge, for her help and enthusiasm on getting this project off the ground and for the indpeth REE inversion modeling she performed.

The analytical results published here would not have been possible without the endless technical support of Sarah Woodland and Chiranjeeb Sarkar, of the Canadian Centre for Isotopic Microanalysis (CCIM) at the University of Alberta. The amount of training they provided in geochemical lab techniques and analysis methods on various instruments is truly astonishing and I thank them for all of it. Thanks are due to Mark Labbe, who spearheaded the investigation into potential contamination caused by the alumina dish and was always ready to help troubleshoot when problems arose during sawing and crushing procedures. James LeBlanc, also of CCIM, was a huge help during the U-Pb TIMS analysis and I thank him for doing more than his share of filament stringing. I thank Bob Duncan and his lab group for the exceptional step heating Ar/Ar ages and Stan Mertzman and his lab group for the excellent XRF analyses. I thank Bill Davis and Carol Evenchick for providing a pre-press manuscript of their 2015 paper, as it was very insightful during my research.

I thank Helen Smyth and Steve Rippington of CASP for collecting and providing the initial samples for this thesis and for their help organizing the 2013 Field expedition. I thank Peter Hülse, also of CASP, for his friendship and for allowing an igneous geochemistry student to join his sedimentological investigation of the Sverdrup Basin. I would like to thank Tim Burton for his friendship, all his hard work running camp smoothly, and for hiking with me to every dark rock we could see on the horizon, even if that meant backpacking 80 km round trip in 3 days.

I would like to thank my Mom for inspiring creativity and for stoking my childhood curiosity of geology by having a plethora of gems and minerals around the house. I thank my Dad for his never-ending support and for insisting that I leave my hometown and go to university. The love and support of my siblings, Lisa, John, and Rachel, has been invaluable over the course of my MSc and for my whole life for that matter. They have always inspired me to question, care, and to push my limits. A special thanks goes to my friend Pedro Waterton, who always took time to help me, both academically and personally, when I needed it most. And finally, I would like to thank my life-partner Michelle Speta, who has been my greatest supporter over the course of this MSc and who critically edited all my writing. The love and home we share has kept me going over the last few years. I thank you for everything.

List of Abbreviations

amu	Atomic mass unit
BDL	Below detection limit
CED	Central Ellesmere domain
CED	Central Ellesmere domain
EDC s.s.	Edge-driven convection senso stricto
EDC w.s.	Edge-driven convection with shear
EMORB	Enriched mid-ocean ridge basalt
Fm.	Formation
HALIP	High Arctic Large Igneous Province
HFSE	High field strength elements
HREE	Heavy rare earth elements (Er to Lu)
km	Kilometer
LILE	Large ion lithophile elements
LIP	Large Igneous Province
LREE	Light rare earth elements (La to Gd)
m	Meter
Ma	Mega annum (million years before present)
Mbr.	Member
MREE	Middle rare earth elements (Gd to Er)
µl	Microliter
µm	Micrometer
MSWD	Mean square weighted deviates
Myr	Million year
NED	Northern Ellesmere domain
NED	Northern Ellesmere domain
NMORB	Normal mid-ocean ridge basalt
OIB	Ocean island basalt
pg	Picogram
ppm	Parts per million
REE	Rare earth element
SCLM	Subcontinental lithospheric mantle
SID	Sverdrup Islands domain
SID	Sverdrup Islands domain
TAS	Total alkali-silica
wt%	Weight percent

Table of Contents

List of Figures

List of Tables

Chapter 1

Introduction

1.1 Thesis Goals and Objectives

The main goal of this research is to apply high-precision U-Pb and Ar/Ar geochronology, in tandem with detailed analytical geochemistry, to a geographically expansive mafic sample suite from the High Arctic Large Igneous Province (HALIP), Canada. The study addresses the variable and prolonged eruption history of mafic magmas and considers them with respect to the changes in lithospheric thickness that took place during the Cretaceous within the Sverdrup Basin. Insights gained through this work on the age of the magmatism and the lithospheric thickness at the time of eruption will have major implications for future tectonic reconstructions of the circum-Arctic during the Cretaceous. The results of this research will also contribute to future studies investigating the thermal maturity of hydrocarbon reserves in the Sverdrup Basin and the metal potential of the magmas.

1.2 Geologic Background

Large Igneous Provinces (LIPs) generally reflect the voluminous and extremely short-lived emplacement of mafic material whose genesis can be linked to mantle processes and usually mark a shift in the regional tectonic regime (Coffin and Eldholm, 1992). Since the term LIP arrived in the literature, it has been common practice to apply it to any mafic succession with a large areal extent, without geochronological evidence indicating a short emplacement period. This misuse has led to a loss of significance of the term ‘LIP’. Bryan and Ernst (2008, references therein) argue for a revised LIP definition that adds quantitative constraints, requiring that 75% of the total magma volume (> 0.1 Mkm^3) must have erupted within approximately 1-5 Myr. This definition has put into question the status of many LIPs around the world and current research is sifting through the candidates to determine which mafic events can be defined as true LIPs.

The most common type of LIPs are those related to hot-spots or mantle plumes (e.g.

continental flood basalts and volcanic rifted margins), which often predate the formation a new spreading centre and oceanic basin (Bryan and Ernst, 2008). These plume-derived LIPs have a characteristic evolution: i) domal uplift and low volume, small-degree partial melt alkali basalts as the plume impinges on the thermal boundary layer; ii) small volume of high-temperature, high-Mg magmas (picrites); iii) main phase of the plume head, generating a voluminous tholeiitic magmatic phase, characterized by unfractionated REE patterns, predating continental breakup; and finally, iv) geographically isolated picrites of the plume tail (Campbell, 2007).

The most striking feature of plume-derived LIPs is the extremely short emplacement age of their mafic magmatism. This has been well constrained, on average, to around 1 Myr based on modern U-Pb and Ar/Ar geochronology (e.g. Deccan Traps and the Parana-Etendeka Province; Schoene et al., 2015; Thiede & Vasconcelos, 2010). Large Igneous Provinces that do not have these 'plume-derived' characteristics must form through other mantle processes such as decompression melting during rifting (White & Mckenzie, 1989), thermal incubation beneath supercontinents (Coltice et al., 2007), lithospheric delamination (Harrison et al., 1992), or edge-driven convection (King and Anderson, 1998).

Geochemical analysis of LIP magmatism can constrain the nature, chemistry, and lithospheric thickness of a given crustal block during major tectonic events. Since LIPs are the result of mantle thermal anomalies, they are accompanied by with changes in lithospheric thickness over the course of their evolution and emplacement. Variability in lithospheric thickness affects basalt trace-element geochemistry in a predictable fashion. Because the garnet-spinel transition zone ranges from 80-100 km in normal mantle geotherms, adiabatic upwelling mantle that encounters thick lithosphere will likely have abundant garnet in its source (McKenzie and O'Nions, 1991). Melt derived from a garnet-rich source would be depleted in HREE, since these elements are compatible in garnet (e.g. Ellam, 1992). This package of upwelling mantle would also experience less decompression melting than it would beneath thinner lithosphere. The outcome is LREE enrichment that indicates lower degrees of partial melting (Ellam, 1992). As LIPs are commonly

associated with continental rifting and large lithospheric attenuation factors, it is common to use REE variability during the eruption of a LIP as a proxy for the variation in lithospheric thickness (e.g. Thompson et al., 2001; Arndt et al., 1998).

1.3 Regional geology and previous work

1.3.1 The Cretaceous HALIP

Cretaceous magmatism of the circum-Arctic islands is commonly known as the High Arctic Large Igneous Province – HALIP – and spans the Canadian Arctic Archipelago, Svalbard, Franz Josef Land, and northern Greenland (Fig. 1.1; Buchan and Ernst, 2006; Bryan and Ernst, 2008; Ernst and Bleeker, 2010; Tegner et al., 2011; Corfu et al., 2013; Estrada and Henjes-Kunst,

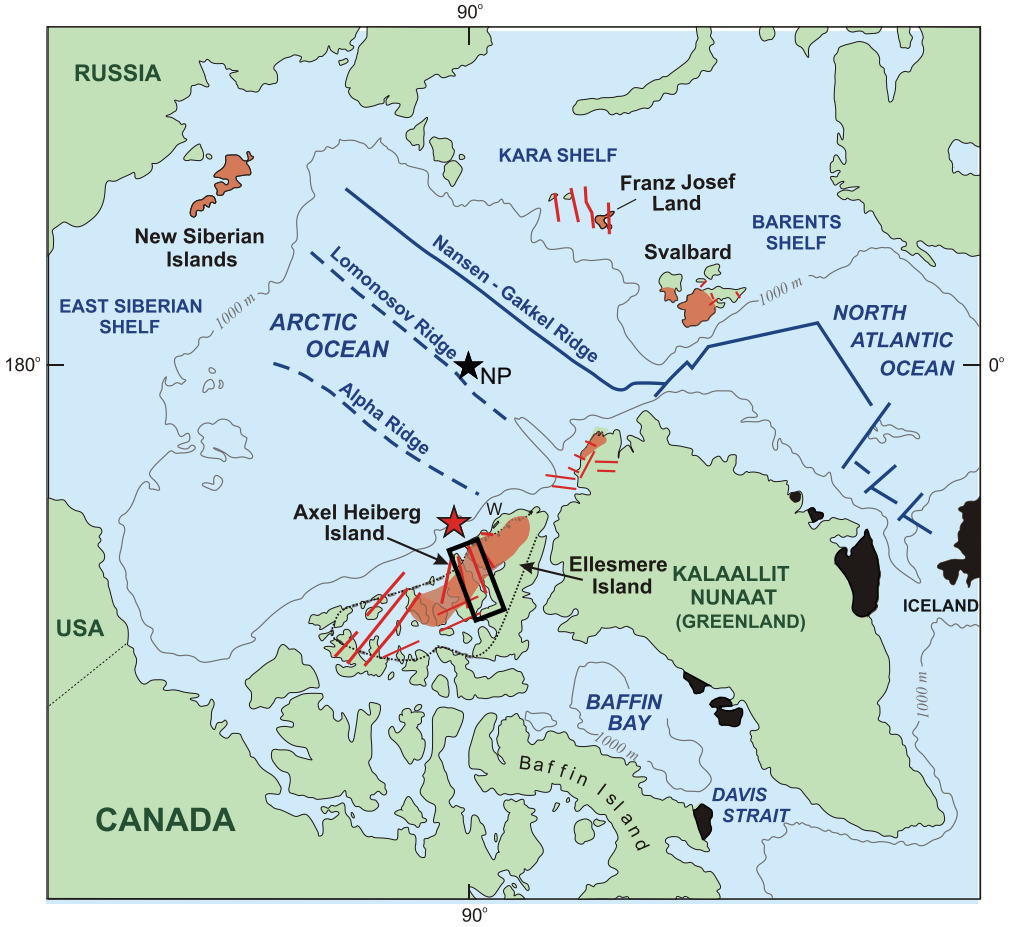

Figure 1.1 Arctic polar projection map displaying the extent of the HALIP (orange shading) modified from Jowitt et al. (2014). Study area outlined in black rectangle. Sverdrup Basin (dashed outline) hosts the Canadian Cretaceous magmatism. The 62 to 55 Ma North Atlantic LIP in black. Proposed plume head (red star) and dyke orientations (red lines) from Ernst and Buchan (2006).

2013; Estrada, 2015; Evenchick et al., 2015). Prior to the opening of the Arctic Ocean and the Baffin Sea (140 – 65 Ma; Larsen et al., 2009), these land-masses were adjacent to one-another in tectonic reconstructions. (e.g. Tegner et al., 2011).

A major volumetric component of the HALIP is the Alpha Ridge: an submarine volcanic edifice, up to 30 km thick (Grantz et al., 2011), off the northwestern coast of Ellesmere Island that bisects the Amerasian Basin, beneath the Arctic Ocean off the northern coast of the Canadian Arctic Archipelago (Fig. 1.1). Seafloor magnetic anomaly patterns constrain the age of the Alpha Ridge to 120-78 Ma (Weber and Sweeney, 1990) and a $^{40}Ar/^{39}Ar$ step-heating age, with a plateau comprising 82% of the total argon, defines the minimum age of the Alpha Ridge to 89 ± 1 Ma (Jokat et al., 2013). It is unclear whether the Alpha Ridge volcanic rocks are underlain by heavily attenuated continental crust or whether it is an oceanic plateau (Forsyth et al., 1986; Jokat, 2003; Grantz et al., 2011). Immobile trace-element concentrations from dredged volcanic samples indicate that the waning eruptions of the Alpha Ridge were alkali basalt (Van Wagoner et al., 1986), similar to ca. 90-75 Ma eruptions located on Ellesmere Island. The Alpha Ridge was emplaced perpendicular to the ancient spreading axis whose Euler pole is located in the Mackenzie Delta, Yukon, Canada (approximately 67°30'N and 130°50'W; Grantz et al., 2011). Sea-floor spreading created oceanic crust between 131 – 127.5 Ma, forming approximately 400 km of oceanic crust and the Amerasian Basin transform fault that now lies beneath the Alpha Ridge (Grantz et al., 2011). Basin-wide uplift and erosion occurred at the same time as MORB eruption initiated in the Amerasian Basin (Embry, 1991), leading to the development of a basin-wide unconformity in the Sverdrup Basin known as the "breakup unconformity" (Embry and Dixon, 1990).

The Canadian manifestation of the HALIP is hosted in the Sverdrup Basin, which straddles the Queen Elizabeth Islands, NU, Canada (Fig. 1.1). Cretaceous rifting coincided with extrusive volcanism in the centre of Sverdrup Basin, which reaches an aggregate thickness of 900 m in Strand Fjord, Axel Heiberg Island (Fig. 1.1; Ricketts et al., 1985). On the northern basin margin,

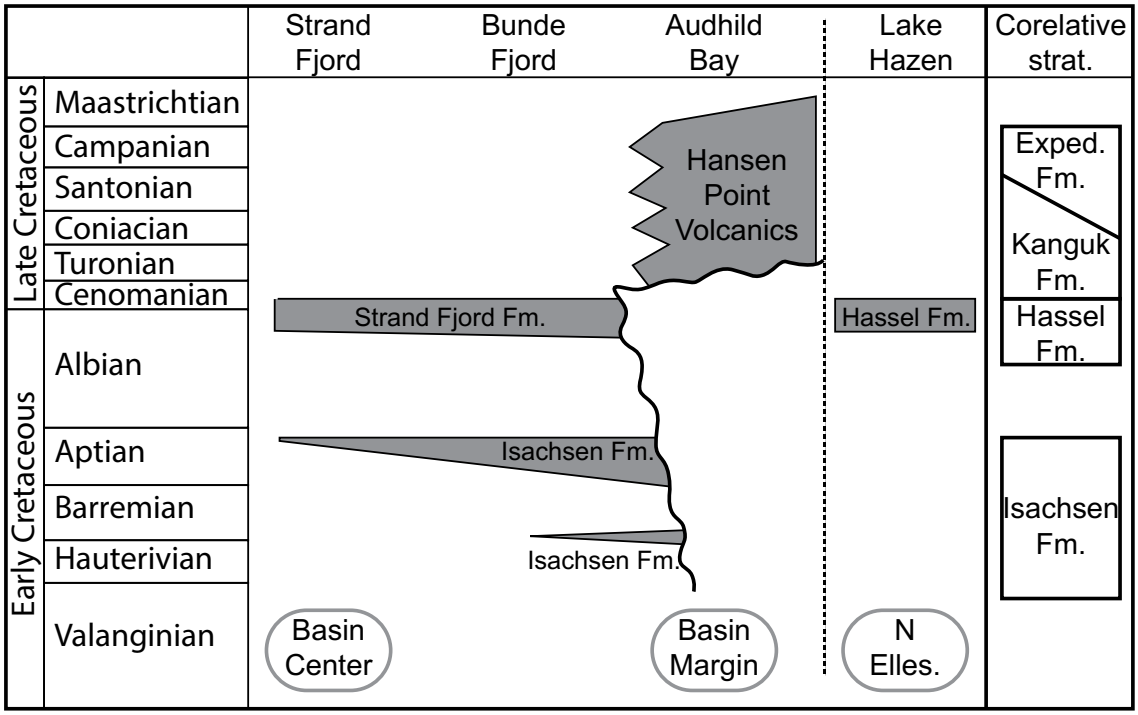

Figure 1.2 Schematic stratigraphy column with basalt formations of the Sverdrup Basin modified from Embry and Osadetz (1988). Hassel Formation basalts are correlative to Strand Fjord Formation basalts, but outcrop mostly on northern Ellesmere Island.

the Hassel Formation has an extrusive thickness of 68 m (Osadetz and Moore, 1988). Hypabyssal intrusive sheets are present across the entire basin and their aggregate thickness exceeds 1500 m in the basin centre (Embry, 1991), which amounts to nearly 12% of the total thickness of the Sverdrup Basin. Uplift and erosion lead to widespread unconformities that correlate to periods of intra-basin magmatism (Balkwill & Fox, 1982). Sandstone formations that relate to the peaks in magmatism (Fig. 1.2) are Isachsen Fm. (latest Valanginian to earliest Albian; 135 – 110 Ma), Hassel Fm. (Cenomanian to earliest Turonian; 100 – 93 Ma), and the Expedition Fm. (Campanian to early Paleocene; 82 – 65 Ma; Embry and Beauchamp, 2008).

1.3.2 Sverdrup Basin formation and tectonics

The Sverdrup Basin is a Carboniferous to Paleogene rift basin comprising 13 km of shelf carbonate and marine siliciclastics that overlie the deformed Precambrian to Devonian passive margin carbonates of the Franklin Mobile Belt (Embry and Beauchamp, 2008). Rifting initiated in the Early Carboniferous and ceased in the Late Cretaceous, with several periods of

quiescence and subsidence (Embry and Beauchamp, 2008). Sediments of the Sverdrup Basin are derived from the erosion of the stable cratons to the south (continental North America) and east (Greenland and eastern Ellesmere Island) as determined through stratigraphy and paleoflow studies (Embry, 1991). Sedimentation was withheld from the proto-Amerasian basin by the Sverdrup Rim, a rift shoulder parallel to the continental margin (Embry & Beauchamp, 2008). During the Cretaceous, renewed rifting caused extensional faults, active subsidence, and initiated a fluvio-deltaic depositional regime that persisted into the Paleogene. During the Eocene (~55 to 35 Ma), a compresional regime dominated, reactivating rift structures and forming the Eurekan Orogeny (Oakey and Stephenson, 2008, and references therein).

Four hydrocarbon source shales have been noted in the Sverdrup stratigraphy, containing up to 10% total organic carbon (Embry, 1991). With several reservoir units and Paleogene structural traps the Sverdrup Basin is host both oil and gas fields. However, the thermal maturity of the basin has been greatly affected by magmatism, rendering hydrocarbons in the centre of the basin over-mature (Embry and Beauchamp, 2008).

1.3.3 Geochemistry

Early geochemical studies of volcanic rocks in the Sverdrup Basin noted the presence of two differing magma types: tholeiitic and alkalic basalts (Ricketts et al., 1985; Trettin and Parrish, 1987; Williamson, 1988). Tholeiitic magmatism forms the stacked extrusive flows of the Strand Fjord Fm. and the Isachsen Formation in the basin centre, on western Axel Heiberg Island (Fig. 1.2). Extrusive alkaline magmatism is less voluminous and in the Hassel Formation (Fig. 1.2) on northern Ellesmere Island. Younger, bimodal volcanism erupted on western Ellesmere Island as part of the Hansen Point Volcanic Complex (HPVC - Trettin and Parrish, 1987; Estrada and Henjes-Kunst, 2013). All magma types occur as both extrusive sequences and hypabyssal intrusions.

Tholeiites form at lower pressure, which is consistent with their appearance in the basin centre, where maximum extension occurred. Alkaline basalts, whose genesis requires thicker

lithosphere, all form along the basin margin. Their ranges overlap at the transition between the basin margin and the basin centre. Magmatism on Ellef Ringnes Island is exclusively tholeiitic (Evenchick et al., 2015). Studies of magmatism on other circum-Arctic islands have not found any alkaline basalts, all are tholeiitic in their major- and trace-element geochemistry (Tegner et al., 2011).

A recent renewal of interest in the geochemistry of the HALIP has resulted in the acquisition of modern high quality ICP-MS trace-element data from a suite of rocks collected by the Geological Survey of Canada (GSC) in the late 1980s (Williamson, 1988; Jowitt et al., 2014). Other recent studies have focused on the Hassel Formation (Estrada, 2015) and the analysis of a few geochronological samples from Ellef Ringnes Island (Evenchick et al., 2015). Recent ICP-MS studies have also been undertaken on basaltic magmas from Svalbard (Corfu et al., 2013; Polteau et al., 2016) and Northern Greenland (Kontak et al., 2001).

1.3.4 Geochronology

Few dedicated geochronological studies have been undertaken in the Canadian HALIP due to its geographic isolation and associated challenging field logistics. Early analyses used whole-rock K/Ar analysis and constrained the range in ages from 93 to 152 Ma (Kerr, 1976; Balkwill and Haimila, 1978; Stevens et al., 1982). With the development of the Ar/Ar step-heating technique, more ages were added, increasing the range in ages from 59 to 152 Ma (Williamson, 1988; Tarduno et al., 1998). Both of the above age ranges do not fit the revised definition of a LIP with their 59 Ma and 93 Myr respective eruption ranges. Noting the wide spread in eruption ages, Villeneuve and Williamson (2006) reassessed previous Ar/Ar results from Williamson (1988) and summarized the state of geochronological studies in the Canadian HALIP. Their review confirmed two peaks of magmatism: a predominantly intrusive peak from 129-127 Ma and an extrusive flood basalt phase between 98-92 Ma.

Biostratigraphic methods have been used to delineate the age range of the extrusive formations of the Sverdrup Basin. Using that method, the oldest units are the extrusive basalts of the

Isachsen Formation on Axel Heiberg Island (Fig. 1.2). This formation is sub-divided into two members: the Paterson Island Member (~135 – 130 Ma) and the Walker Island Member (~127 – 120 Ma). Both members are interbedded with coarse-grained, fluvial sandstone of the Isachsen Formation (Embry and Osadetz, 1988). Analytical geochronology has confirmed the age of the Walker Island Member, but no age results obtained via modern analytical techniques have been published that match the older Paterson Island Member. Widespread volcanism occurred between 105 and 90 Ma, with more than 15 extrusive sequence localities across Axel Heiberg Island and minor occurrences on Ellesmere Island. This is the most voluminous phase with stratigraphic thicknesses ranging from 100-800 m. Tholeiites of the Strand Fjord Formation dominate magmatic activity on Axel Heiberg at this time, with the palynology of interbedded and correlative shales indicating Albian to earliest Cenomanian (Balkwill, 1983; Embry and Osadetz, 1988). Contemporaneous extrusive alkaline basalts interlayer with Hassel Formation sandstones near Lake Hazen, northern Ellesmere Island. The differences between the contemporaneous Strand Fjord Fm. and Hassel Fm. basalts indicates differing magma genesis in different areas of the Sverdrup Basin. The last peak of magmatism is the Hansen Point Volcanic Complex, constrained by biostratigraphy to 95 – 70 Ma. Located on the northwestern coast of Ellesmere Island (Fig. 1.1), the HPVC has composite sections ranging between 600 – 1000 m of subaerial interbedded basalt, basanite, rhyolite, and dacite (Embry and Osadetz, 1988).

Prior to 2013, one zircon U-Pb analysis was published for a quartz diorite pluton in the Canadian HALIP, yielding an age of 92 ± 1 Ma (Trettin and Parrish, 1987). This was later confirmed by numerous U-Pb results for the hornblende gabbros and felsic plutons of the Wooton Intrusive Complex (Estrada and Henjes-Kunst, 2013). These outcrops are in the same vicinity as the HPVC. Trettin and Parrish (1987) also reported the first of three U-Pb ages of gabbroic rock in the Canadian HALIP, taken from the HPVC. Their results show strong discordance and a upper intercept $^{207}Pb/^{206}Pb$ age of 88 $^{+20}/_{-21}$ Ma, likely having suffered Pb loss along fractures (modern thermal annealing and chemical abrasion techniques that can mitigate this problem were developed by Mattinson (2005) nearly 20 years after their study). An additional two U-Pb ages of

gabbros have been published recently by Evenchick et al. (2015), who dated tholeiitic intrusions from Ellef Ringnes Island (~121 and 127 Ma). Across the rest of the circum-Arctic HALIP, only Corfu et al. (2013) have produced U-Pb results on the mafic sheets. They published five U-Pb ages of the tholeiitic sills on Svalbard (124.5 – 121.5 Ma). These recent studies indicate that the coarse-grained hypabyssal intrusions are suitable for U-Pb geochronology, yet very few U-Pb ages have been determined in the Candian HALIP. Other than the one result from Trettin & Parrish (1987), there were no U-Pb ages for the latest Albian mafic magmatism peak in the Sverdrup Basin or elsewhere in the HALIP prior to the present study.

1.4 Research Objectives

The research presented in this thesis describes the geographic spread, geochronology, and geochemistry of 74 HALIP samples from across Axel Heiberg and Ellesmere Islands, NU, Canada, and 2 basanite samples from Bathurst Island (obtained from Mitchell and Platt, 1984) that are genetically related to the above samples. The samples were collected during fieldwork in the summer of 2013.

1.4.1 REE inversion modeling of Cretaceous lithospheric thickness

Major-elements analysed by XRF (x-ray fluorescence) and trace-elements analysed by ICP-MS (inductively coupled plasma mas spectrometry) were conducted on 72 samples from the Canadian HALIP, as well as 24 Sr-Nd tracer isotope systematics measured by TIMS (thermal ionization mass spectrometry). The results are compared to the only other ICP-MS trace-element studies (Kontak et al., 2001; Jowitt et al., 2014; Estrada, 2015). The most primitive and least crustally contaminated samples are used as inputs for an REE inversion model (McKenzie and O'Nions, 1991; White and McKenzie, 1995) that calculates the depth to melt initiation and the thickness of the lithosphere at the time of melt generation. This model is applied at varying mantle potential temperatures to investigate the mantle processes that generated the voluminous and geochemically diverse HALIP.

1.4.2 U-Pb and Ar/Ar geochronology of the distinct magma types

High-precision U-Pb and $^{40}Ar/^{39}Ar$ analyses were performed on 10 samples from the centre of the Sverdrup Basin to its margin. Prior to this study, only twenty-three ages for mafic samples had been published using modern Ar/Ar techniques and two samples were dated using high-precision U-Pb geochronology, providing a very broad age range of 73.5 to 128.2 Ma for the HALIP magmatism of the Sverdrup Basin. More than half of these samples, detailed in section 1.3.4, were analysed before the year 2000, using older – less sensitive techniques. Developments of geochronological methods over the past two decades have resulted in significant improvements in precision. The new geochronology database presented here represents a major new contribution to understanding the timing and duration of HALIP mafic magmatism.

1.5 Thesis Layout

The main body of this thesis is laid out as two stand-alone papers. It is undecided whether these two chapters will define seperate manuscripts or be combined into one manuscript that will be submitted for publication in a peer-reviewed journal.

Chapter 2: REE inversion modelling (McKenzie and O'Nions, 1991; White and McKenzie, 1995) is applied to 24 samples across the Sverdrup Basin, both from the present study and previously published ICP-MS studies, to ascertain the thickness of the lithosphere during the eruption of the Cretaceous HALIP. Authors are D.M. Dockman, D.G. Pearson, and S.A. Gibson.

Chapter 3: U-Pb and Ar/Ar geochronology applied to 10 mafic samples of the Canadian HALIP in order to better constrain the eruption history of the magma pulses and gain insight on a model for magma genesis. Authors are D.M. Dockman, D.G. Pearson, L.M. Heaman, and C. Sarkar.

Chapter 4: A brief summary of the thesis and conclusions of study are detailed in the final chapter.

References

Arndt, N., Chauvel, C., Czamanske, G., and Fedorenko, V., 1998, Two mantle sources, two plumbing systems: tholeiitic and alkaline magmatism of the Maymecha River basin, Siberian flood volcanic province, *Contributions to Mineralogy and Petrology*, v. 133, no. 3, p. 297–313.

Balkwill, H.R., 1983, *Geology of Amund Ringnes, Cornwall and Haig-Thomas Islands, District of Franklin*, Geological Survey of Canada Memoir 390, 76 p.

Balkwill, H.R., and Fox, F.G., 1982, Incipient rift zone, western Sverdrup Basin, Arctic Canada, in: Embry, A.F. and Balkwill, H.R. (Eds.), *Arctic Geology and Geophysics*, Canadian Society of Petroleum Geologists Memoir 8, p. 171–187.

Balkwill, H.R., and Haimila, N.E., 1978, K/Ar ages and significance of mafic rocks, Sabine Peninsula, Melville Island, District of Franklin, in: Blackadar, R., Griffin, P., Dumych, H., and Neale, E. (Eds.), *Current Research, Part C*, Geological Survey of Canada Paper No. 78-1C, p. 35-38.

Bryan, S.E., and Ernst, R.E., 2008, Revised definition of Large Igneous Provinces (LIPs), *Earth-Science Reviews*, v. 86, p. 175–202.

Buchan, K.L., and Ernst, R., 2006, Giant dyke swarms and the reconstruction of the Canadian Arctic islands, Greenland, Svalbard and Franz Josef Land, in: Hanski, E., Mertanen, S., Rämö, T., and Vuollo, J. (Eds.), *Dyke Swarms: Time Markers of Crustal Evolution*, Taylor and Francis Group, London, UK, p. 27–48.

Campbell, I.H., 2007, Testing the plume theory, *Chemical Geology*, v. 241, p. 153–176.

Coffin, M.F., and Eldholm, O., 1992, Volcanism and continental break-up: A global compilation of large igneous provinces, in: Storey, B.C., Alabaster, T., and Pankhurst, R.J. (Eds.), *Magmatism and the Causes of Continental Break-up*, The Geological Society of London Special Publication No. 68, p. 17–30.

Coltice, N., Phillips, B.R., Bertrand, H., Ricard, Y., and Rey, P., 2007, Global warming of the mantle at the origin of flood basalts over supercontinents, *Geology*, v. 35, no. 5, p. 391–394.

Corfu, F., Polteau, S., Planke, S., Faleide, J.I., Svensen, H., Zayoncheck, A., and Stolbov, N., 2013, U-Pb geochronology of Cretaceous magmatism on Svalbard and Franz Josef Land, Barents Sea Large Igneous Province, *Geological Magazine*, v. 150, no. 6, p. 1127–1135.

Ellam, R.M., 1992, Lithospheric thickness as a control on basalt geochemistry, *Geology*, v. 20, p. 153–156.

Embry, A.F., 1991, Mesozoic history of the Arctic Islands, in: Trettin, H.P. (Ed.), *Geology of the Innuitian Orogen and Arctic Platform of Canada and Greenland*, Geological Survey of Canada, p. 369-433.

Embry, A., and Beauchamp, B., 2008, Sverdrup Basin, in: Miall, A. (Ed.), *Sedimentary Basins of the World*, *Volume 5*, Elsevier Ltd., p. 451–471.

Embry, A.F., and Dixon, J., 1990, The breakup unconformity of the Amerasia Basin, Arctic Ocean: Evidence from Arctic Canada, *GSA Bulletin*, v. 102, p. 1526–1534.

Embry, A.F., and Osadetz, K.G., 1988, Stratigraphy and tectonic significance of Cretaceous volcanism in the Queen Elizabeth Islands, Canadian Arctic Archipelago, *Canadian Journal of Earth Sciences*, v. 25, p. 1209–1219.

Ernst, R., and Bleeker, W., 2010, Large igneous provinces (LIPs), giant dyke swarms, and mantle plumes: Significance for breakup events within Canada and adjacent regions from 2.5 Ga to the present, *Canadian Journal of Earth Sciences*, v. 47, p. 695–739.

Estrada, S., 2015, Geochemical and Sr-Nd isotope variations within Cretaceous continental flood-basalt suites of the Canadian High Arctic, with a focus on the Hassel Formation basalts of northeast Ellesmere Island, *International Journal of Earth Sciences*, v. 104, no. 8, p. 1981–2005.

Estrada, S., and Henjes-Kunst, F., 2013, ^{40}Ar-^{39}Ar and U-Pb dating of Cretaceous continental rift-related magmatism on the northeast Canadian Arctic margin, *Zeitschrift der Deutschen Gesellschaft für Geowissenschaften*, v. 164, p. 107–130.

Evenchick, C.A., Davis, W.J., Bedard, J.H., Hayward, N., and Friedman, R.M., 2015, Evidence for protracted High Arctic large igneous province magmatism in the central Sverdrup Basin from stratigraphy, geochronology, and paleodepths of saucer-shaped sills, *GSA Bulletin*, v. 127, no. 9/10, p. 1366–1390.

Forsyth, D.A., Morel-A-L'Huissier, P., Asudeh, I., and Green, A.G., 1986, Alpha Ridge and Iceland - Products of the same plume? *Journal of Geodynamics*, v. 6, p. 197–214.

Grantz, A., Hart, P.E., and Childers, V.A., 2011, Geology and tectonic development of the Amerasia and Canada Basins, Arctic Ocean, in: Spencer, A.M., Embry, A.F., Gautier, D.L., Stoupakova, A.V., and Sorensen, K. (Eds.), *Arctic Petroleum Geology*, The Geological Society of London Memoir 35, p. 771–799.

Harrison, T.M., Copeland, P., Kidd, W.S.F., and Yin, A.N., 1992, Raising Tibet, *Science*, v. 255, no. 5052, p. 1663–1670.

Jokat, W., 2003, Seismic investigations along the western sector of Alpha Ridge, Central Arctic Ocean, *Geophysical Journal International*, v. 152, no. 1, p. 185–201.

Jokat, W., Ickrath, M., and O'Connor, J., 2013, Seismic transect across the Lomonosov and Mendeleev Ridges: Constraints on the geological evolution of the Amerasia Basin, Arctic Ocean, *Geophysical Research Letters*, v. 40, no. 19, p. 5047–5051.

Jowitt, S.M., Williamson, M.-C., and Ernst, R.E., 2014, Geochemistry of the 130 to 80 Ma Canadian High Arctic large igneous province (HALIP) event and implications for Ni-Cu-PGE prospectivity, *Economic Geology*, v. 109, no. 2, p. 281–307.

Kerr, J.W., 1976, Geology of outstanding Arctic aerial photographs: 3. Margin of Sverdrup Basin, Lyall River, Devon Island, *Bulletin of Canadian Petroleum Geology*, v. 24, no. 2, p. 139–153.

King, S.D., and Anderson, D.L., 1998, Edge-driven convection, *Earth and Planetary Science Letters*, v. 160, p. 289–296.

Kontak, D.J., Jensen, S.M., Dostal, J., Archibald, D.A., and Kyser, T.K., 2001, Cretaceous mafic dyke swarm, Peary Land, northernmost Greenland: Geochronology and petrology, *The Canadian Mineralogist*, v. 39, no. 4, p. 997–1020.

Larsen, L.M., Heaman, L.M., Creaser, R.A., Duncan, R.A., Frei, R., and Hutchison, M., 2009, Tectonomagmatic events during stretching and basin formation in the Labrador Sea and the Davis Strait: Evidence from age and composition of Mesozoic to Palaeogene dyke swarms in West Greenland, *Journal of the Geological Society*, v. 166, p. 999–1012.

Mattinson, J.M., 2005, Zircon U-Pb chemical abrasion ("CA-TIMS") method: Combined annealing and multi-step partial dissolution analysis for improved precision and accuracy of zircon ages, *Chemical Geology*, v. 220, no. 1-2, p. 47–66.

McKenzie, D., and O'Nions, R.K., 1991, Partial melt distributions from inversion of rare earth element concentrations, *Journal of Petrology*, v. 32, no. 5, p. 1021–1091.

Mitchell, R.H., and Platt, R.G., 1984, The Freemans Cove volcanic suite: Field relations, petrochemistry, and tectonic setting of nephelinite–basanite volcanism associated with rifting in the Canadian Arctic Archipelago, *Canadian Journal of Earth Sciences*, v. 21, no. 4, p. 428–436.

Oakey, G.N., and Stephenson, R., 2008, Crustal structure of the Innuitian region of Arctic Canada and Greenland from gravity modelling: Implications for the Palaeogene Eurekan Orogen, *Geophysical Journal International*, v. 173, no. 3, p. 1039–1063.

Osadetz, K.G., and Moore, P.R., 1988, Basic volcanics in the Hassel Formation (mid-Cretaceous) and associated intrusives, Ellesmere Island, District of Franklin, Northwest Territories, Geological Survey of Canada Paper 87-21, 19 p.

Polteau, S., Hendriks, B.W.H., Planke, S., Ganerød, M., Corfu, F., Faleide, J.I., Midtkandal, I., Svensen, H., and Myklebust, R., 2016, The Early Cretaceous Barents Sea Sill Complex: Distribution, $^{40}Ar/^{39}Ar$ geochronology, and implications for carbon gas formation, *Palaeogeography, Palaeoclimatology, Palaeoecology*, v. 441, p. 83–95.

Ricketts, B., Osadetz, K.G., and Embry, A.F., 1985, Volcanic style in the Strand Fiord Formation (Upper Cretaceous), Axel Heiberg Island, Canadian Arctic Archipelago, *Polar Research*, v. 3, p. 107–122.

Schoene, B., Samperton, K.M., Eddy, M.P., Keller, G., Adatte, T., Bowring, S.A., Khadri, S.F.R., and Gertsch, B., 2015, U-Pb geochronology of the Deccan Traps and relation to the end-Cretaceous mass extinction, *Science*, v. 347, no. 6218, p. 182–184.

Stevens, R.D., Delabio, R.N., and Lachance, G.R., 1982, Age determinations and geological studies: K-Ar isotopic ages, Report 15, Geological Survey of Canada Paper 81-2, 56 p.

Tarduno, J.A., Brinkman, D.B., Renne, P.R., Cottrell, R.D., Scher, H., and Castillo, P., 1998, Evidence for extreme climatic warmth from Late Cretaceous Arctic vertebrates, *Science*, v. 282, no. 5397, p. 2241–2244.

Tegner, C., Storey, M., Holm, P.M., Thorarinsson, S.B., Zhao, X., Lo, C.H., and Knudsen, M.F., 2011, Magmatism and Eurekan deformation in the High Arctic Large Igneous Province: ^{40}Ar-^{39}Ar age of Kap Washington Group volcanics, North Greenland, *Earth and Planetary Science Letters,* v. 303, no. 3-4, p. 203–214.

Thiede, D.S., and Vasconcelos, P.M., 2010, Paraná flood basalts: Rapid extrusion hypothesis confirmed by new 40Ar/39Ar results, *Geology*, v. 38, no. 8, p. 747–750.

Trettin, H.P., and Parrish, R., 1987, Late Cretaceous bimodal magmatism, northern Ellesmere Island: Isotopic age and origin, *Canadian Journal of Earth Sciences*, v. 24, no. 2, p. 257–265.

Villeneuve, M., and Williamson, M.-C., 2006, ^{40}Ar-^{39}Ar dating of mafic magmatism from the Sverdrup Basin Magmatic Province, in: Scott, R.A. and Thurston, D.K. (Eds.), *ICAM IV Proceedings*, Dartmouth, Nova Scotia, p. 206–215.

Van Wagoner, N.A., Williamson, M.-C., Robinson, P.T., and Gibson, I.L., 1986, First samples of acoustic basement recovered from the Alpha Ridge, Arctic Ocean: New constraints for the origin of the ridge, *Journal of Geodynamics*, v. 6, p. 177–196.

Weber, J.R., and Sweeney, J.F., 1990, Ridges and basins in the central Arctic Ocean, in: Grantz, A.L., Johnson, L., and Sweeney, J.F. (Eds.), *The Geology of North America, Volume L, The Arctic Ocean Region*, The Geological Society of America, p. 305-336.

White, R., and McKenzie, D., 1989, Magmatism at rift zones: The generation of volcanic continental margins and flood basalts, *Journal of Geophysical Research*, v. 94, no. B6, p. 7685–7729.

White, R.S., and McKenzie, D., 1995, Mantle plumes and flood basalts, *Journal of Geophysical Research*, v. 100, no. B9, p. 17,543–17,585.

Williamson, M.-C., 1988, The Cretaceous igneous province of the Sverdrup Basin, Canadian Arctic: Field relations and petrochemical studies, PhD thesis, Dalhousie University, Halifax, NS, 417 p.

Chapter 2

Geochemistry and REE inversion modelling

2.1 Introduction

Large Igneous Provinces (LIPs) represent the voluminous and extremely short-lived emplacement of mantle-derived mafic magma into Earth's crust, usually marked by a shift in the regional tectonic regime (Coffin and Eldholm, 1992). The most common type of LIPs are those related to hot-spots or mantle plumes, such as continental flood basalts or volcanic rifted margins, which often predate the formation of a new spreading centre and oceanic basin (Bryan and Ernst, 2008). Plume-derived LIPs have a standard geochemical evolution characterized by early, small volume alkali basalts and picrites followed by a high-volume tholeiitic phase (e.g., Campbell, 2007). To be classified as a plume-derived LIP, this high-volume phase must represent greater than 75% of the total erupted volume and, by definition, be emplaced rapidly (in 1 – 5 Myr; Bryan and Ernst, 2008). Emplacement age determination of LIPs must be undertaken using modern U-Pb and Ar/Ar geochronology to obtain the precision necessary to constrain such a short eruption timescale (e.g. Parana-Etendeka and Siberian Traps: Schoene et al., 2015; Thiede and Vasconcelos, 2010).

The abundant Cretaceous magmatism of the circum-Arctic islands is commonly known as the High Arctic Large Igneous Province – HALIP – and spans the Canadian Arctic Archipelago, Svalbard, Franz Josef Land, and northern Greenland (Fig. 2.1; Bryan and Ernst, 2008; Buchan and Ernst, 2006; Corfu et al., 2013; Ernst and Bleeker, 2010; Estrada and Henjes-Kunst, 2013; Estrada, 2014; Evenchick et al., 2015; Tegner et al., 2011). Recently, the HALIP's designation as a single LIP has been questioned, as geochronological studies and biostratigraphy indicate at least two magmatic pulses over a 50 Myr eruption timespan (Jowitt et al., 2014; Tegner et al., 2011). Furthermore, the complicated geochemical and geographic distribution of the HALIP does not comply with standard plume-derived LIP criteria. A key feature of the plume model is that the thickness of the lithospheric 'lid' (e.g., Ellam, 1992; Mckenzie and Bickle,

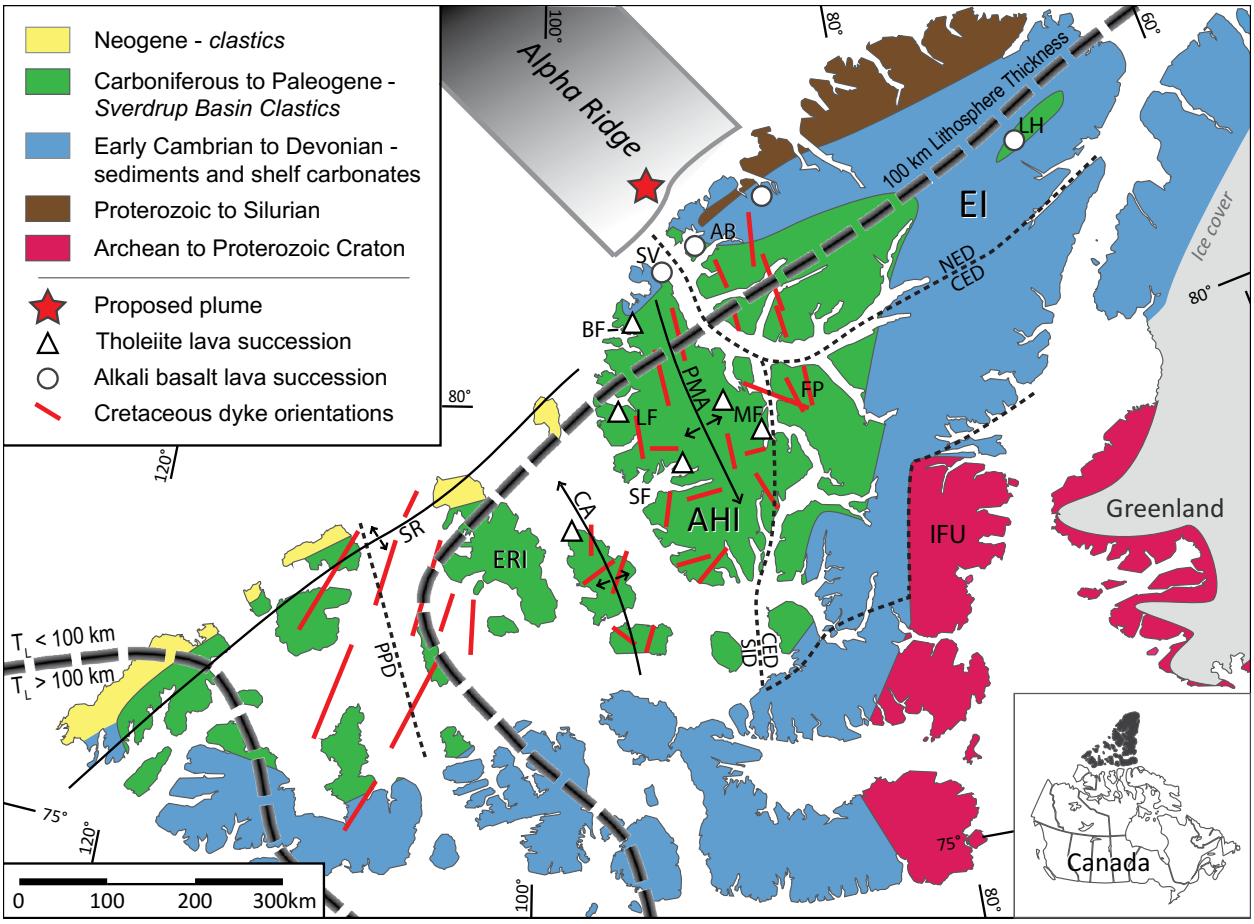

Figure 2.1 Regional map of the Queen Elizabeth Islands, High Arctic Canada, showing: i) Regional geology, with the Sverdrup Basin in green (based on Okulitch, 1991) and sampling range circled in light grey; ii) Lava succession locations (Embry and Osadetz, 1988); iii) dyke orientations and proposed plume location (Buchan and Ernst, 2006); iv) four tectonic domains of the Sverdrup Basin (SID – Sverdrup Islands Domain; PPD – Prince Patrick Domain; NED – Northern Ellesmere Domain, CED – Central Ellesmere Domain) and relevant structural highs (PMA – Princess Margret Arch; CA – Cornwallis Arch; SR – Sverdrup Rim) from Trettin (1991); v) surface trace (heavy dashed line) of the +4% S-wave seismic anomaly (Schaeffer and Lebedev, 2014), which approximates the 100 km T_L (modern thickness of the lithosphere). Geographic locations: Alpha Ridge – offshore volcanic edifice; EI – Ellesmere Island; AHI – Axel Heiberg Island; ERI – Ellef Ringnes Island; AB – Audhild Bay; BF – Bunde Fjord; FP – Fosheim Penninsula; LH – Lake Hazen; MF – Mokka Fjord; SF – Strand Fjord; SV – Svarteveeg Cliffs; IFU – Inglefield Uplift.

1988) exerts control on the magma geochemistry generated in the upwelling mantle. Here, we investigate through quantitative modelling the effect of lithospheric thickness on magma geochemistry within the Sverdrup Basin, and use radiogenic isotopes (Sr-Nd) to evaluate both crustal contamination and constrain magma source regions. In doing so, we aim to add numerical constraints on the thickness of the syn-rift Cretaceous lithosphere of the HALIP, which will better constrain a tectono-magmatic interpretation of the Canadian HALIP.

2.2 Geologic Background

The Canadian manifestation of the HALIP is hosted in the Sverdrup Basin, which straddles the Queen Elizabeth Islands, NU, Canada (Fig. 2.1). Cretaceous rifting coincided with extrusive volcanism in the centre of Sverdrup Basin, which reaches an aggregate thickness of 900 m in Strand Fjord, Axel Heiberg Island (Fig. 2.1; Ricketts et al., 1985). Hypabyssal intrusive sheets are present across the entire basin and their aggregate thickness exceeds 1500 m in the basin centre (Trettin, 1991). Combined, the Cretaceous magmatism of the Sverdrup Basin approaches ~19% of the basin thickness. Two magma types have been described in the HALIP: tholeiitic basalt and mildly alkalic basalts, both typically present within any LIP. Both magma geochemistries are expressed as extrusives and hypabyssal intrusions and appear to be emplaced over a total duration of at least 50 Myr (130 to 80 Ma; Jowitt et al., 2014; Tegner et al., 2011). The tholeiites and mildly alkalic basalts are juxtaposed in geographically and temporally, putting into question the plume-derived hypothesis for the HALIP accepted by many authors (Buchan and Ernst, 2006). Recently, Tegner et al. (2011) and Thorarinsson et al. (2011) challenged the idea that both the tholeiitic and mildly alkalic rocks are part of the same large igneous province.

2.3 Controls on magma geochemistry

LIPs are the result of mantle thermal anomalies, which impinge on the thermal boundary layer and are therefore associated with changes in lithospheric thickness over the course of their evolution and emplacement (Hamilton et al., 1998; Kerr, 1994). Variability in lithospheric thickness affects basalt trace-element geochemistry in a predictable fashion (e.g., Ellam, 1992; Gibson and Geist, 2010; Fig. 2.2). Heavy rare earth elements (HREEs) are compatible in garnet during partial melting, so basalts derived from deeper sources, where garnet is stable in the melting residue, will be depleted in HREEs. Light rare earth elements (LREEs) are more incompatible than their heavier counterparts and are therefore more concentrated in the initial, smaller-degree melt-fractions. Hence, enrichment in LREE relative to HREE can therefore be used as a proxy for the amount of partial melting of the mantle peridotite that occurred to

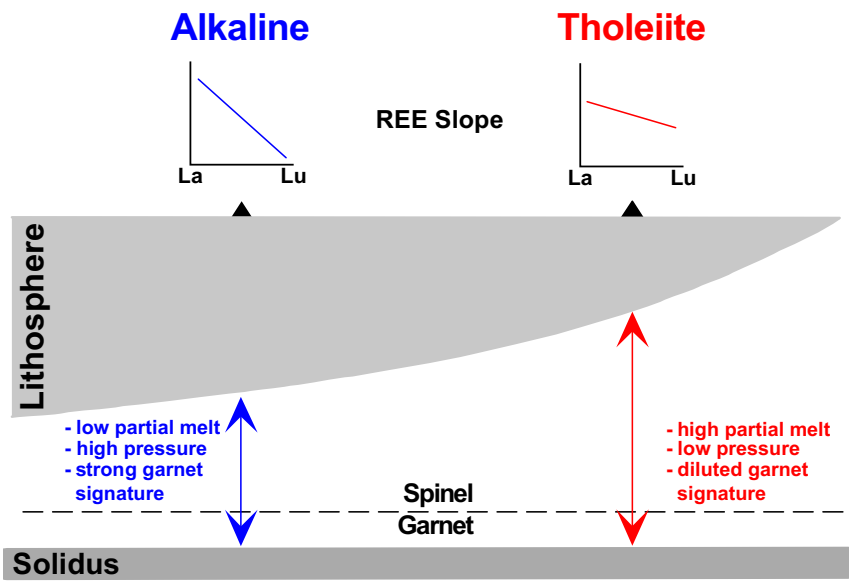

Figure 2.2 Cartoon illustrating the effect of lithosphereic "lid" thickness on REE geochemistry modified from Ellam (1992). Low percentage partial melting at high pressures, in the garnet stability field, produces alkalic basalt. Large degree partial melting dilutes the initial concentration of LREE, overall flattening out the REE pattern and generating tholeiites.

produce the basalt in question and also the thickness of the mechanically ridged lithosphere—the lithospheric 'lid' (McKenzie and O'Nions, 1991). As LIPs are commonly associated with continental rifting and large lithospheric attenuation factors, REE variability can be used as a proxy for pre- and post-LIP lithospheric thickness (e.g. Hole et al., 2015). In this contribution, we attempt to quantify the lithospheric thickness variation in the magma source regions of Sverdrup Basin HALIP magmas via inversion of REE to yield the variation in melt fraction with depth (e.g., Gibson et al., 2015; McKenzie and O'Nions, 1991)

2.4 Analytical Methods

2.4.1 Field area and samples

The study area covers a length of 400 km NW to SE between eastern Axel Heiberg and western Ellesmere Islands, centered on Nansen and Eureka Sounds between the islands (Fig. 2.1). This area was chosen in order to sample both the high magma volume in the basin centre, near the proposed plume head (Ernst and Buchan, 2001), as well as the eastern basin margin where only intrusive sheets are present.

Samples were collected from 74 discrete locations (geographic coordinates found in Appendix A); two were lava successions and the rest were intrusive sheets, ranging from 0.5-25 m thick. A minimum of two samples was collected for each of the thick (>5 m) intrusions: one sample from close to the intrusive margin to obtain a quenched sample that had undergone minimal in-situ fractionation, for bulk-rock geochemistry and a second sample from the more coarsely crystalline intrusion centre, for potential U-Pb and Ar/Ar geochronology (see Chapter 3). Two lava successions were sampled, each with five distinct flows delineated by amygdale abundance and size, as well as by paleosol development between flows. The flows ranged from 4-8 m thick. Geochemistry samples ranged from 0.5-2 kg and geochronology samples from 2-5 kg.

Six samples of the sedimentary country rock were also collected: shale, siltstone, mudstone and carbonate rich siltstone. These samples were taken from the same locations as some of the volcanic rocks and were analysed for trace-elements and Sr-Nd isotopic signatures to help in constraining the degree of wall rock assimilation during magma emplacement into the crust.

2.4.2 Whole-rock Geochemistry

The following procedures were applied to a sample subset assessed petrographically to have low alteration and fine to aphanitic crystal size. Crushing procedures are outlined in Appendix B.

2.4.2.1 Major and Minor Elements

74 volcanic rocks were analysed for Major- and trace-elements by X-ray fluorescence at the X-ray Laboratory at Franklin and Marshall College, Pennsylvania following methods described in detail by Mertzman (2000). Major-elements were measured on fusion discs and some minor elements, notably Ni, Cr, V and Sc via powder briquettes. Major-element precision was calculated from 10 separate fusion disks of the OKUM (a certified reference komatiite standard) during a parallel analysis to this study (Waterton, *in prep.*). Precision varies by oxide (outlined in Appendix A) with the highest being CaO (0.6% relative standard deviation) and the lowest being K_2O and P_2O_5 (3.7% and 3.5% relative standard deviation, respectively). The average relative standard deviation is 1.4% for all the major-elements. As OKUM is a komatiite, oxide

concentration differences effect the precision. For example, there is 10 – 50 times less K_2O and and 10 – 40 times less P_2O_5 in OKUM than the basalts of the Canadian HALIP. The higher concentrations in the basalts of this study would likely ameliorate the analytical precision of the above two major-elements. Regardless of the chemical differences between OKUM and the Canadian HALIP basalts, the results analyzed by Waterton et al. (*in preparation*) overlap the preferred values for OKUM (Jochum et al., 2005) within 95% confidence limits and are therefore accurate.

2.4.2.2 Trace-Elements

Trace-elements from 71 samples were analyzed via solution ICP-MS with a Thermo Element-2XR at the Arctic Resources Geochemistry Facility, University of Alberta. Detailed analytical methods are outlined in supplementary methods. Analytical uncertainty for the ICP-MS trace-elements were calculated based on nine separate BCR-2 dissolutions that were analyzed 15 times (1σ quoted in Appendix A). The analyzed BCR-2 results overlap with preferred values (Jochum et al., 2005) at the 95% confidence limit, using a Student's t-distribution factor (14 degrees of freedom), and are therefore accurate. All trace-elements were calibrated using dissolved rock standards BCR-2, BHVO-2, and BIR-1 with various dilution factors. A procedural blank was run with each 15 samples. Blank corrections were made to all samples but were insignificant for all elements.

2.4.3 Sr-Nd Isotopic Geochemistry

20 mafic samples and 2 sedimentary rocks from the Sverdrup Basin Magmatic Province were analyzed for their Sr and Nd isotope compositions. Analyses were performed on a Thermo Triton Plus Thermal Ionization Mass Spectrometer (TIMS) at the University of Alberta Arctic Resources Geochemistry Facility. Ratios were measured on Faraday cups with 10^{11} Ω amplifiers. Detailed analytical methods are outlined in the supplementary methods.

Sr isotope measurements were made using 3.5 µL of TaF_5 as an activator and were mass fractionation corrected using a $^{88}Sr/^{86}Sr$ ratio of 8.3752. Six separate analyses of 100 ng of

SRM987 reference material run during the course of the analytical campaign gave a mean $^{87}Sr/^{86}Sr$ value of 0.710252 ± 16 (2σ), which is within error of the preferred value of 0.710246 (Jochum et al., 2005). Two BCR-2 and two BHVO-2 basalt certified reference materials were dissolved and run as to assess accuracy and their $^{87}Sr/^{86}Sr$ values overlap the preferred values within error. Measured unknowns are not corrected to the standard value.

For Nd analysis, 150-400 ng of Nd was dried down with 1.5 µL of 0.1 M H_3PO_4 and run as Nd metal ions. All $^{143}Nd/^{144}Nd$ ratios were fractionation corrected to a $^{146}Nd/^{144}Nd$ ratio of 0.7219 using an exponential law. Seven separate analyses of the JNdi certified reference material (200 ng) gave a mean of 0.512094 ± 1, which is within error of the preferred value of 0.512104 ± 10 (n = 276; Jochum et al., 2005). The two BCR-2 values obtained during this analytical campaign are within 3σ of the preferred value (0.512636 ± 4) while the two BHVO-2 samples are within 2σ error of the preferred value (0.512980 ± 24). It is likely that our BCR-2 values lie just out of error simply due to the excellent precision of the preferred value.

Ratios were corrected to an initial ratio at a time of 90 Ma using Sm and Nd CHUR values of Bouvier et al. (2008) and those of DePaolo and Wasserburg (1976) for Sr and Rb CHUR values. The ^{87}Rb decay constant ($1.3968 \times 10^{-11} \pm 2.7 \times 10^{-14}$) was from from Rotenberg et al. (2012) and the ^{147}Sm decay constant ($6.539 \times 10^{-12} \pm 9.9 \times 10^{-14}$) from Lugmair and Marti (1978). Uncertainties quoted on the initial ratio include fully propagated errors from the age and Sm/Nd ratio.

2.4.4 REE Inversion Model

Rare earth element (REE) inversion modeling was undertaken following the approach of McKenzie and O'Nions (1998, 1991) and White and McKenzie (1995). This inversion method models multiple trace-element concentrations to predict compositional variations of the melt as a function of depth. Model inputs include major-element, trace-element, and REE concentrations along with initial $^{87}Sr/^{86}Sr_i$ and εNd_i isotopic ratios to assist in assessing the nature of the source mantle. Fe_2O_3 concentrations were calculated using a consistent factor of 0.1 of FeO_T for all

inverted samples, regardless of melt composition. The model outputs the depth of melt initiation, percent of partial melt, and the top of the melt column, which corresponds to the base of the lithosphere.

Since the melt column of upwelling mantle crosses from the garnet to the spinel (and potentially the plagioclase) stability fields, the model applies mineral-melt partition coefficients (outlined in Gibson and Geist, (2010), and references therein) to calculate the percentage of melting within each mantle mineral stability field. The depth of the garnet-spinel transition zone is sensitive to mantle potential temperatures (T_p). For example, a change from T_p of 1315 °C to 1500 °C alters the phase transition zone depth from 60-80 km to 80-100 km (Klemme and O'Neill, 2000). This study sets the garnet-spinel transition zone parameter to 70-90 km depth, which reflects an average T_p of ~1400 °C. This is reasonable for an extensional basin adjacent to a large cratonic mass such as the Canadian Shield (Jaupart and Mareschal, 2007).

2.5 Petrography

2.5.1 Tholeiites

All tholeiitic rocks sampled within our study are intrusive in nature, being plagioclase- and clinopyroxene-phyric dolerites, with the two phenocryst phases often occurring in glomerocrysts. Some samples have resorbed olivine and in one case subhedral plagioclase phenocrysts overgrowing the olivine, indicating two stages of phenocryst growth (DMD114M – Fig. 2.3). However, olivine phenocrysts are rare relative to the other phases. Samples with lower MgO contents are quartz-phyric, correlating with their quartz-normative nature (CIPW norms of Section 6.1). Plagioclase microphenocrysts occur in the aphanitic samples and vary in size from 50 – 200 μm. Groundmass phases include plagioclase, clinopyroxene and opaque minerals. Alteration of clinopyroxene to chlorite and plagioclase to sericite is present (Figure 2.3) and occurs in varying degrees from weak (DMD114M) to strong (DMD108M), correlating with an increase in LOI (0.49 and 1.1 wt%, respectively). In sub-gabbroic samples, where an aphanitic quenched margin of the intrusion was not able to be sampled, crystal phases are equigranular and

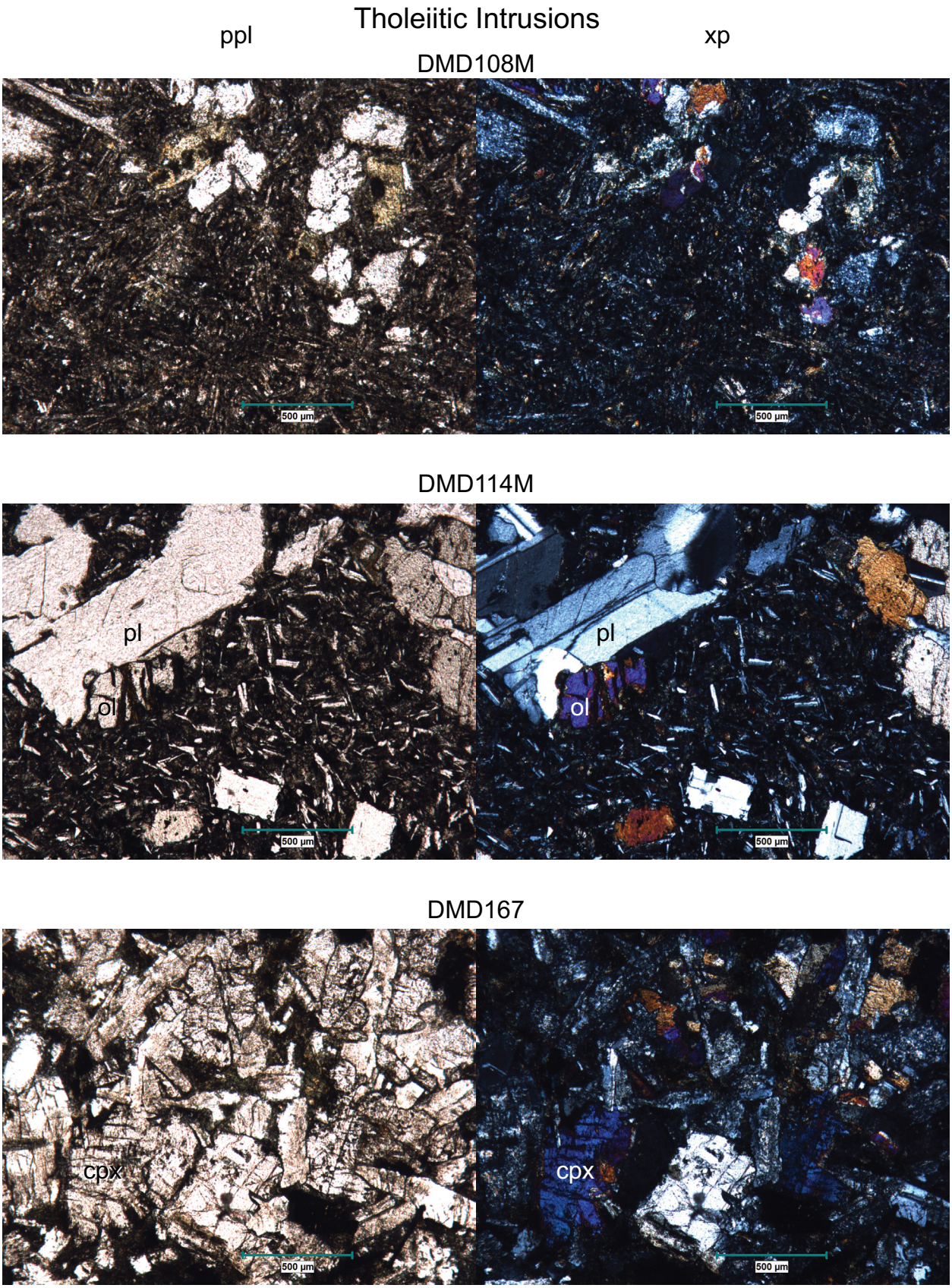

Fig 2.3 (continued on next page)

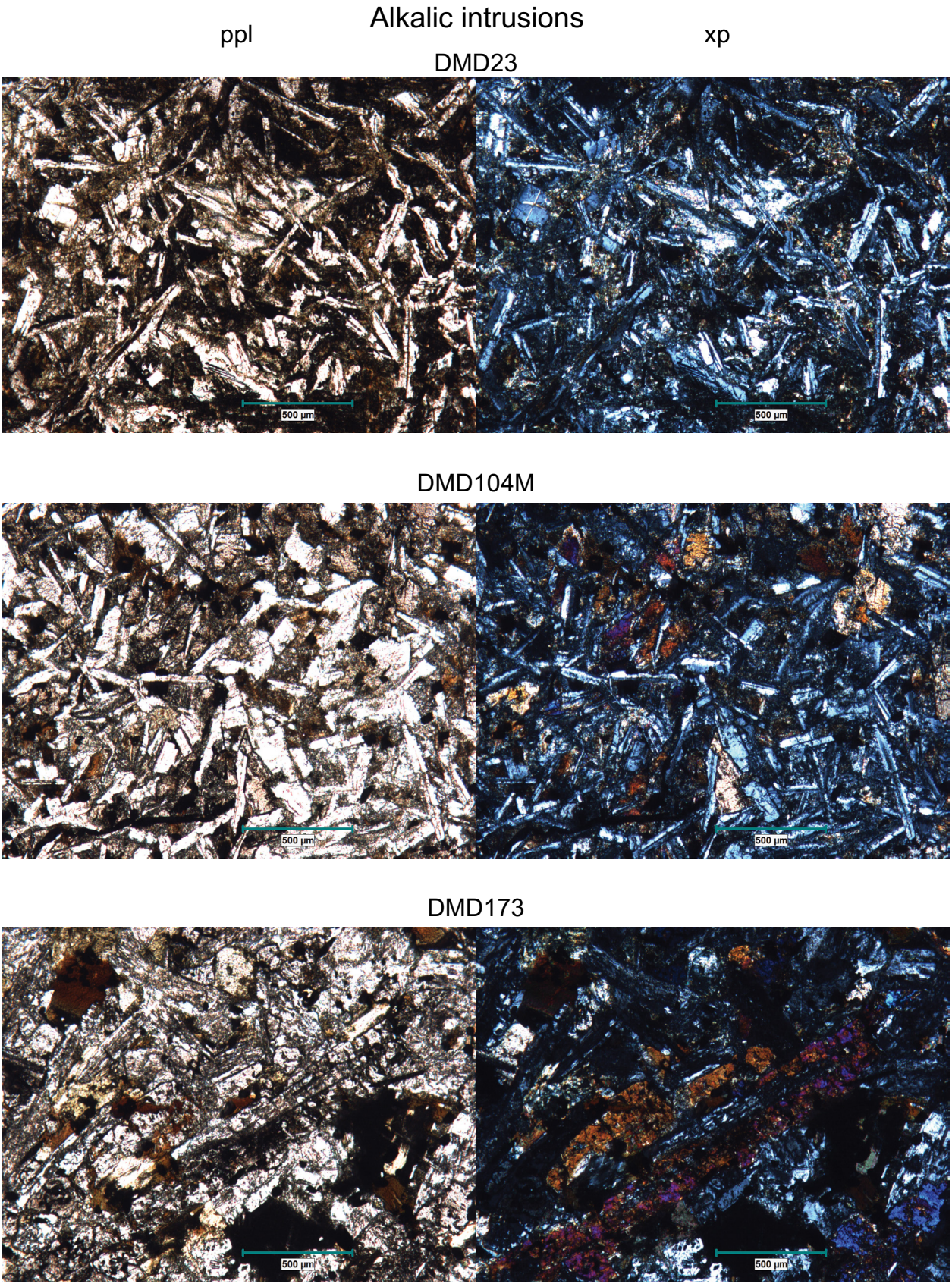

Fig 2.3 (continued on next page)

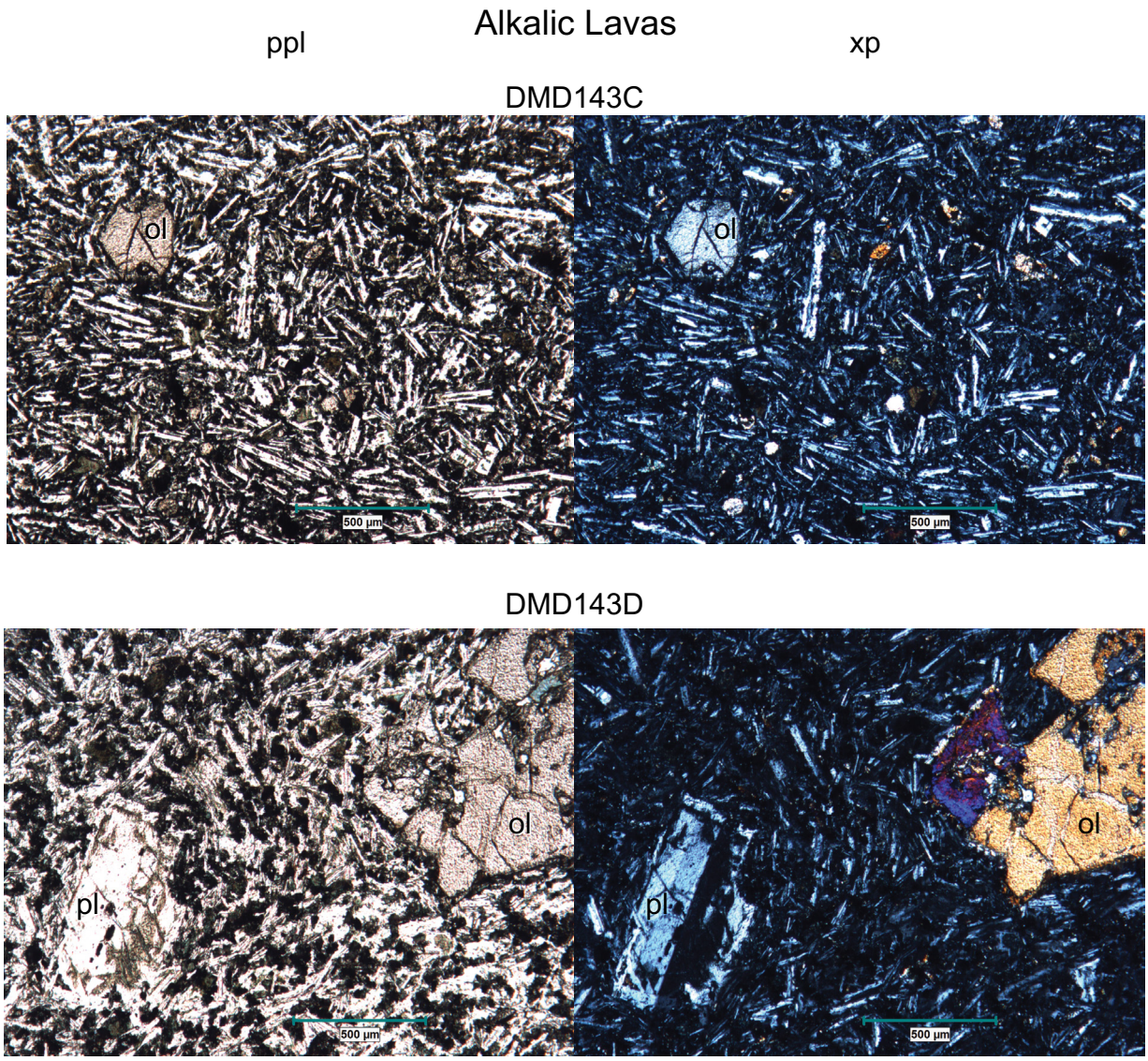

Figure 2.3 Petrographic images from the Cretaceous basalts of the Sverdrup Basin, see text for details. ppl - plain polarized light; xp - crossed plolars; pl - plagioclase; ol - olivine; cpx- clinopyroxene. Scale bar 500 µm.

range between 0.5 to 2 mm long (DMD167), with intergrowth of clinopyroxene and plagioclase as primary phases. This study did not sample any extrusive tholeiites.

2.5.2 Alkalic basalts

Alkalic basalt intrusions contain subhedral intergrowths of plagioclase and clinopyroxene (± olivine) that range in crystal size from 200 – 500 µm in finer grained samples (DMD104M and DMD23) to 0.5 – 2 mm in coarser samples (DMD173). Opaques are commonly first to crystallize as they are included in plagioclase and clinopyroxene. As with the tholeiites, alteration

of plagioclase to sericite and clinopyroxene to chlorite is weak in samples with low LOI (DMD104M; 1.3) and strong in those with higher LOI (DMD23; 2.0). DMD173 has primary biotite intergrowing with the other phases indicating a more hydrated melt. This sample also has moderate serpentinization of olivine, which, being hydrous, also increases the reported LOI (2.2 wt%).

Alkalic basalt lavas are plagioclase- and olivine-phyric, with embayed subhedral, anhedral, and skeletal olivine providing evidence of resorption. Plagioclase phenocrysts show evidence of resorption (DMD143C) and re-growth (DMD143D). Microphenocrysts of plagioclase dominate the lavas, growing between 50 – 200 μm in length and are sub-trachytic. Opaques are very abundant, as seen in plane polarized light, indicating eruption under oxidizing conditions. Groundmass is very fine crystalline, perhaps devitrified glass.

2.6 Results

2.6.1 Major-element variations

Major-elements for 71 samples (Table A in Appendix A) were plotted on a total alkali-silica plot (Fig. 2.4), with the majority of samples falling in the basalt field. A few samples lie within the trachybasalt and basaltic andesite fields, but are not classified as such, since the TAS relies on fluid-mobile elements such as Na and can therefore lead to misclassification. The tholeiite-alkali basalt delineation line from Macdonald (1968) does not adequately constrain the two magma types due to alteration issues, but indicates the presence of both magma types, in agreement with previous studies (e.g., Jowitt et al., 2014). Our classification will use immobile trace-elements (Section 2.6.2).

CIPW normative mineralogy was calculated for all samples and plotted on a basalt tetrahedron (Fig. 2.5). Fe^{3+}/Fe^{2+} was set at 0.1 for all samples. Three samples are nepheline-normative (DMD173, DMD164M, and DMD25), which is the defining characteristic of an ‘alkalic basalt’ and indicates that the HALIP contains true alkalic intrusions. However, CIPW norms also rely on

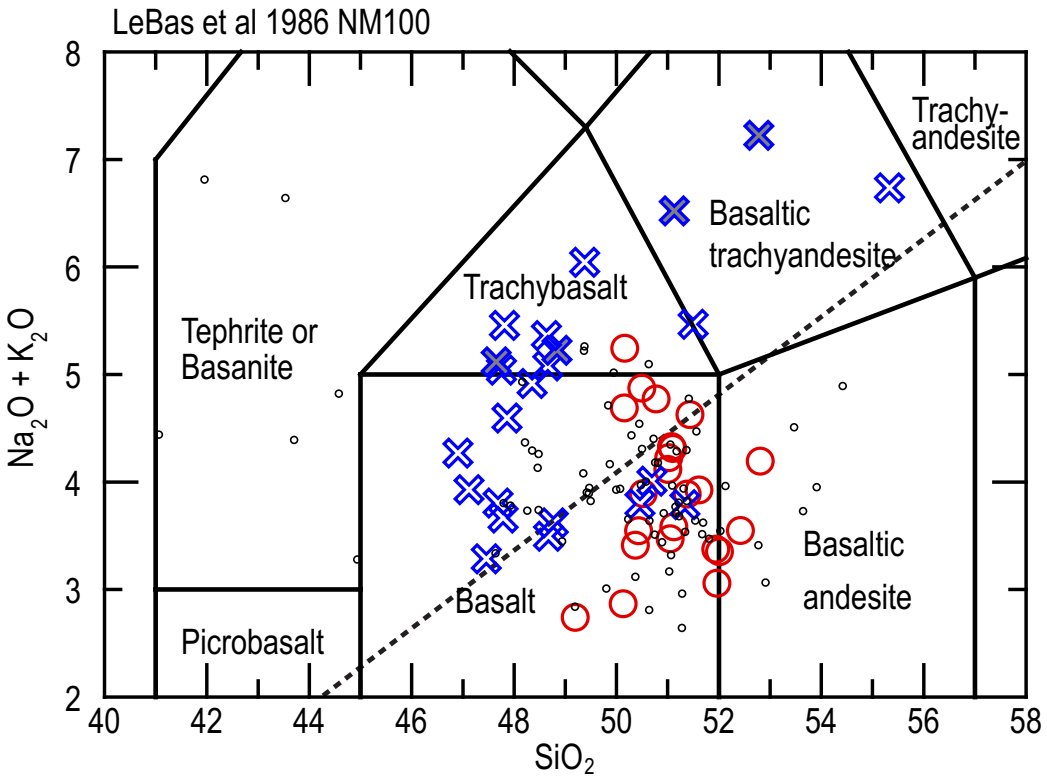

Figure 2.4 Total alkali-silica (TAS) diagram. LOI < 3 wt%. Alkali-tholeiite discrimination line from Macdonald (1968), though not used for classification as immobile trace-elements are used (see Section 2.6.2). Data from this study in blue (alkalic basalts) and red (tholeiites), classified based on immobile elements. Previously published results from Estrada and Henjes-Kunst, 2004; Estrada, 2014; Jowitt et al., 2014; Kontak et al., 2001; Mitchelle and Platt, 1984.

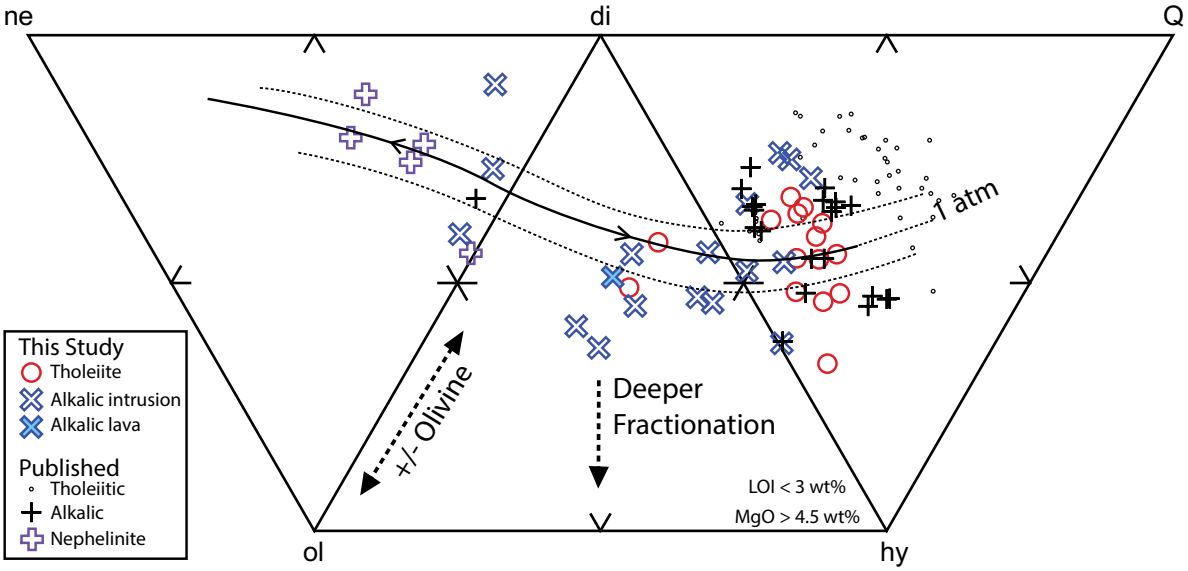

Figure 2.5 CIPW normative mineralogy plotted on a flattened basalt tetrahedron after Thompson (1982) showing 3 nepheline-normative alkalic basalts. Upper crustal fractionation drives magma evolution along the '1 atm' path. Deeper fractionation (i.e. base of the crust) drives the magma composition to the higher olivine- and hypersthene-normative portion of the central tri-plot. Fe^{3+}/Fe^{2+} set to 0.1. ne – nepheline; di – diopside; Q – quartz; ol – olivine; hy – hypersthene.

mobile major-elements and there is an inherent weakness of major-element classification systems that is well illustrated in Figure 2.5. A nepheline normative magma generated at depth can and will evolve into the quartz normative field along the one atmosphere cotectic, which evidently occurred in HALIP magmas (Fig. 2.5; Thompson, 1982). Since the present study is concerned with the source geochemical characteristics and their relation to lithospheric thickness, a immobile trace-element based magma classification scheme is used, as immobile trace-element ratios are little affected by fractionation and liquid-crystal processes (Farmer, 2014; See section 2.6.2 for classification). This classifies samples with similar REE patterns to the nepheline-normative basalts as alkalic basalts, despite their major-elements being fractionated into the hypersthene- or quartz-normative fields (Fig. 2.5).

Samples with loss on ignition (LOI) less than 3 wt% are plotted on major-element variation diagrams (Fig. 2.6). The Sverdrup Basin intrusive sheets span a relatively narrow range of MgO from 3.0 to 7.2 wt% whereas the lavas from Audhild Bay (Fig. 2.1) range from 2.0 to 4.9 wt% MgO. The low MgO of the lavas are likely due to intense fractional crystallization of a high-Mg phase (e.g. olivine) or significant alteration that results in a range of LOI from 1.2 to 8.8 wt%. The five lavas DMD153A-E are much more altered than the five lavas DMD143A-E. There is a prominent inflection point in CaO between 4.5 and 5 wt% MgO, indicating the initiation of clinopyroxene crystallization. There is an overall broad increase in Al_2O_3 (12.5 to 17.1 wt%) with increasing MgO, whereas SiO_2 (45.2 to 52.4 wt%) decreases as MgO rises. All samples are sodic basalts (Na_2O: 2.2 to 5.9 wt%; K_2O: 0.3 to 2.6 wt%). TiO_2, P_2O_5, and SiO_2 are the most effective of the major/minor elements at dividing the basalts into alkalic and tholeiitic variants, with the alkalic rocks plotting at higher TiO_2 (3.3 to 4.0 wt%) and P_2O_5 (0.40 to 1.1 wt%), with lower SiO_2 values. Tholeiitic samples have lower TiO_2 (2.0 to 3.3 wt%) and P_2O_5 (0.20 to 0.41 wt%), with higher SiO_2 values. Samples with less than 4 wt% MgO correspond to high SiO_2, Al_2O_3, and total alkalis, particularly in DMD124, which is coarse grained with felsic segregations. There is significant overlap of the samples, between the alkalic and tholeiite fields in $Na_2O + K_2O$, FeO, and MnO compositional space.

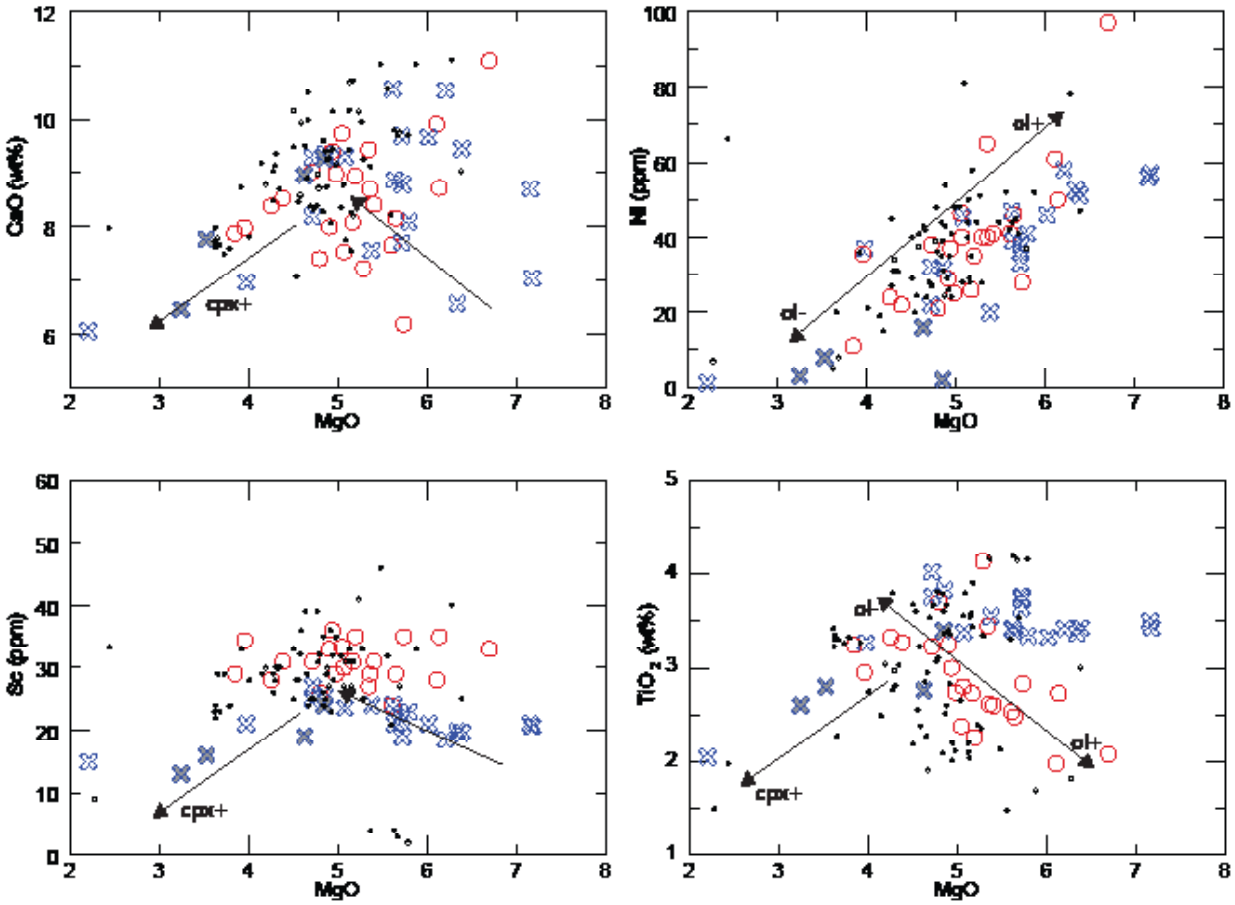

Figure 2.6 Variation of MgO with selected major and minor elements. An inflection point in the CaO concentrations at 4.5 wt% MgO (tholeiites) and 5 wt% MgO (alkalic basalts), indicates fractional crystallization of clinopyroxene at lower MgO values. These inflection points are also present in Sc. The negative correlation between Ni and MgO is indicative of olivine fractionation, which ceases between 3 – 4 wt% MgO. The increase in TiO_2 with decreasing MgO (4 – 7 wt%) indicates that no Ti-bearing oxides were co-crystalizing at the same time as olivine.

2.6.2 Immobile element magma classification

Trace-elements are used for the classification of the 71 samples from this study (Table in Appendix A). Immobile trace-elements have long been used as perhaps the most reliable form of magma classification where rocks are altered. Using Nb/Y vs $Zr/(P_2O_5 \times 10^4)$ systematics (Fig. 2.7a ; Floyd and Winchester, 1977) separates the 71 samples from this study into an approximately 50:50 split of tholeiitic (N = 36) and alkalic basalts (N = 35). The 3 nepheline-normative basalts (see Section 2.6.1) are highlighted as green symbols for reference. Plotting the classification derived from Figure 2.7a on the Pearce (1996) Zr/Ti vs. Nb/Y diagram (Fig. 2.7b) there is overlap between the alkalic basalt and the tholeiite fields. Pearce (1996) constructed this

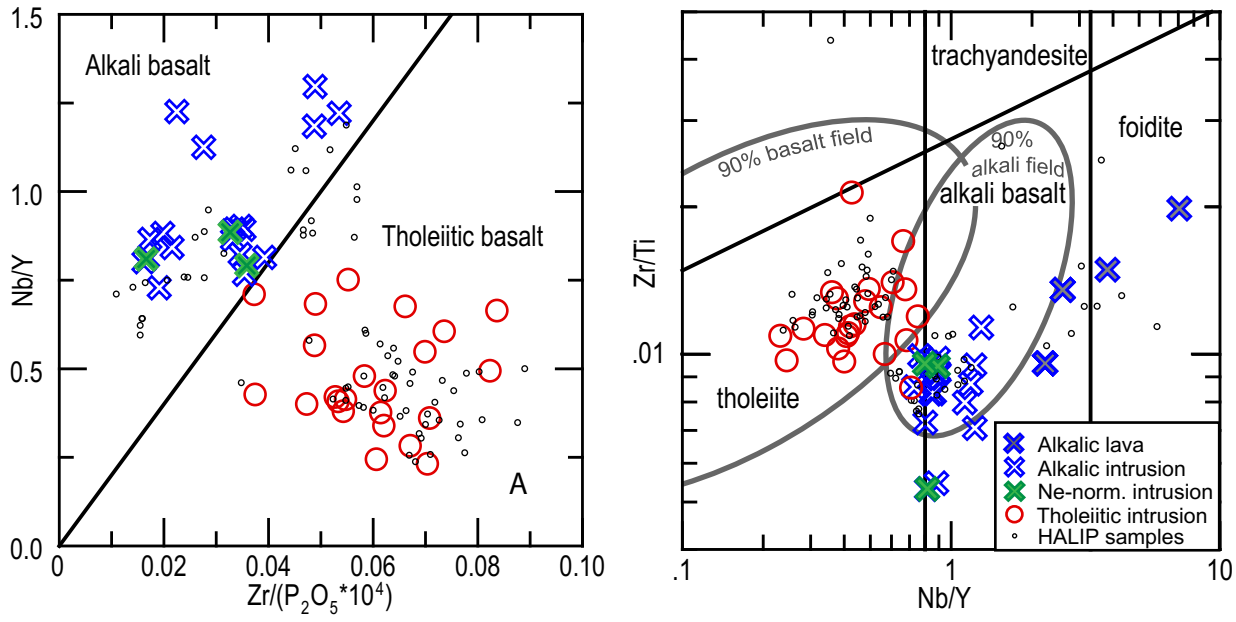

Figure 2.7 Immobile trace-element ratio plots used for rock classification. Only samples with < 3 wt% LOI are plotted. The 3 ne-normaitve samples from Fig 2.5 are plotted in green. **a)** Nb/Y versus Zr/(P_2O_5*10^4) immobile trace-element plot used to discriminate between alkalic and tholeiitic basalts. **b)** Zr/Ti vs Nb/Yb after Pearce (1996). See text for discussion on 90% confidence ovals, which better separate the rocks classified using Figure 7a. Data from this study in blue (alkalic basalts) and red (tholeiites); alkalic lavas in blue with shaded fill. Previously published HALIP data from Estrada and Henjes-Kunst, 2004; Estrada, 2014; Jowitt et al., 2014; Kontak et al., 2001; basanites from Mitchell and Platt, 1984.

diagram using 90% confidence ovals whereby 90% of all alkalic basalts lie within that oval. The 90% confidence ovals (Fig. 2.7b) better delineate the samples from the Canadian HALIP into the two different magma types classified in Figure 2.7a. Accordingly, the mildly alkaline basalts from Jowitt et al. (2014) have been included in this study as sodic alkaline basalts. Irrespective of the details of the classification schemes, the main result is that the Sverdrup Basin magmas range in composition from those that are typical hypersthene-normative tholeiites, to compositions that are significantly more alkalic and nepheline normative, indicative of a broad range in melting conditions.

2.6.3 Trace-element variations

The HALIP alkali magmas are generally more enriched in incompatible elements compared to the tholeiites. Variations in Sc concentration with respect to MgO mimic the inflection points for clinopyroxene (Section 6.1), as Sc is compatible in this phase (Fig. 2.6.1). Systematic

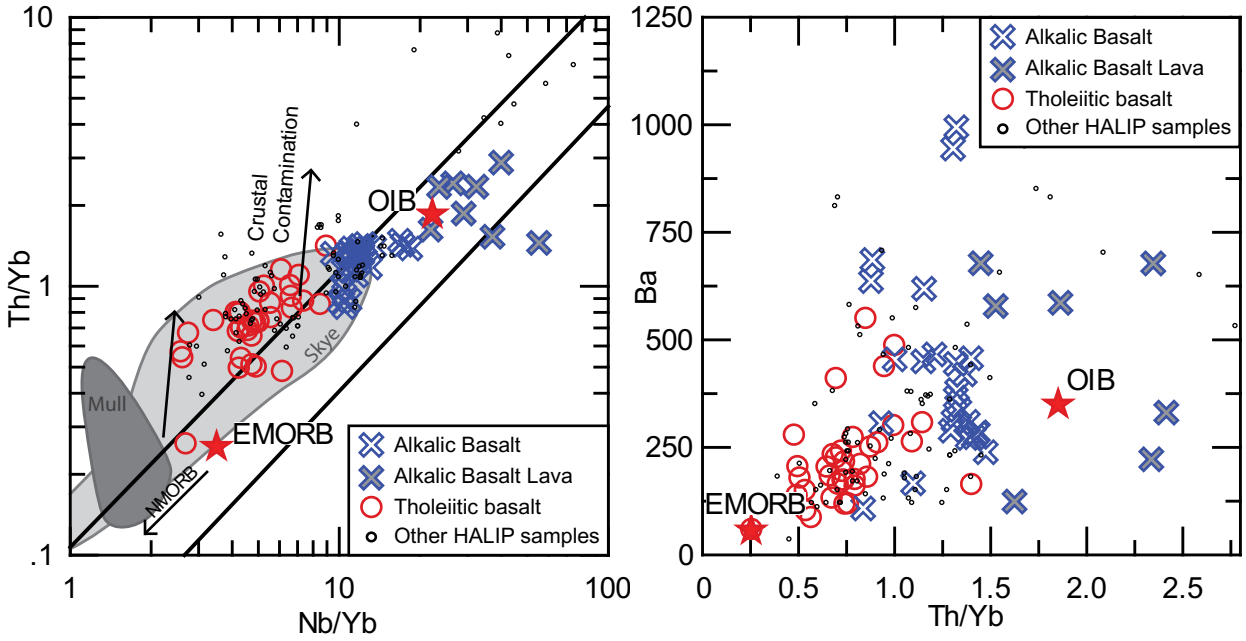

Figure 2.8 a) Th/Yb versus Nb/Yb projection for the Canadian HALIP. Uncontaminated basalts plot along the 'mantle array' between NMORB (normal MORB) and OIB. All samples are plotted, regardless of LOI, to constrain the extent of crustal contamination, which displaces a sample to higher Th/Yb values along a vector near parallel to the Th/Yb axis. Alkalic lavas from Audhild Bay plot near OIB, while some heavily altered Svartveeg Cliff lavas plot below the mantle array. Skye lavas from Thompson et al. (1986; 1982) overlap with the samples from this study, having similar compositions and assimilation of crustal components to drive the compositions off the 'mantle array'. Mull samples from the same studies are more depleted than the Canadian HALIP. **b)** Ba versus Th/Yb of Canadian HALIP samples. Previously published data from Estrada and Henjes-Kunst, 2004; Estrada, 2014; Jowitt et al., 2014; Kontak et al., 2001.

trends and relationships are probably complicated by varying degrees of crustal contamination, evident in the elevated Th/Yb in both magma types (Fig. 2.8a), yet more so for the tholeiites. Ba ranges widely across the suite (from ~ 50 to 1000 ppm), weakly correlating with MgO. Ba variation is larger in the alkali basalt suite (Fig 8b). The more elevated Ba values, which mimic the other LILEs (e.g. Cs, K, Rb, etc.), are probably indicative of contamination or hydrothermal alteration. Screening for these effects will be addressed in Section 2.6.6. Tholeiites are generally much higher in Cu (50 to 225 ppm) than alkali rocks (10 to 50 ppm). While the alkalic basalts are generally significantly more enriched in Sr (400 to 800 ppm) than the tholeiites (150 to 475 ppm), the lack of correlation with MgO is indicative of the effects of both plagioclase fractionation and crustal contamination. Ni broadly correlates with MgO in both magma series, likely due to the extent of olivine fractionation at depth.

Chondrite normalised REE plots (Fig. 2.9a) show averages of the two magma types of the

Canadian HALIP, for both intrusives and lavas. There is a strong distinction between the LREE/HREE enriched alkaline basalts and the less enriched tholeiites. Lavas from Axel Heiberg Island (Strand Fjord, Bunde Fjord, Mokka Fjord; Figure 2.1), are identical in REE pattern to the average of the tholeiitic intrusions across the Sverdrup Basin (Fig. 2.9a). The alkalic basalts of the Hassel Formation (Lake Hazen; Figure 2.1) match the average REE pattern of the alkalic basalt intrusions and are OIB-like (Fig. 2.9a). The Hansen Point Volcanic Complex (HPVC; Audhild Bay lavas from Figure 2.1) are more enriched in LREE/MREE than the average alkalic basalt, yet the mid to heavy REE pattern matches, indicating a similar amount of melting in the garnet lherzolite field (Ellam, 1992). The tholeiites have an enriched MORB pattern that has an overall LREE/HREE enrichment of a factor of 2 to 8, indicating variable amounts of olivine fractional crystallization prior to eruption. When compared to the Mull lavas from the British Paleogene igneous province, the HALIP volcanics of this study are more enriched in REEs, on average (Fig. 2.9a), indicating a likely origin via melting beneath thicker lithosphere (see below) and that the HALIP basalts are a result of more extensive olivine fractionation prior to eruption.

REE inter-element ratios such as La/Sm and Gd/Yb (Fig. 2.9c) summarise well the changes in REE patterns through the magma series. For basalts La/Sm is a good proxy for the amount of partial melting whereas the Gd/Yb ratio serves more as a proxy for the depth of melting. These proxies (Fig. 2.9c) separate the tholeiites into the lower La/Sm (higher degrees of partial melt) and lower Gd/Yb (shallower melt) quadrant. For comparison to tholeiites in other LIPs, the Mull lavas of the BPIP (Kerr, 1995) are more depleted in REE, indicative of higher degrees of partial melting than the HALIP alkalic basalt samples. However, there is considerable overlap between the Mull lavas and the HALIP tholeiites (Fig. 2.9c). There is a clear distinction between the Axel Heiberg lavas and the lavas from Ellesmere Island, with intrusions of similar affinity to the Axel Heiberg eruptives plotting near them (Fig. 2.9c), providing a potential geochemical signature with which to track the intrusive plumbing for the different lava sequences of the HALIP.

As Gd/Yb is primarily controlled by the lithospheric lid thickness during magma formation, we

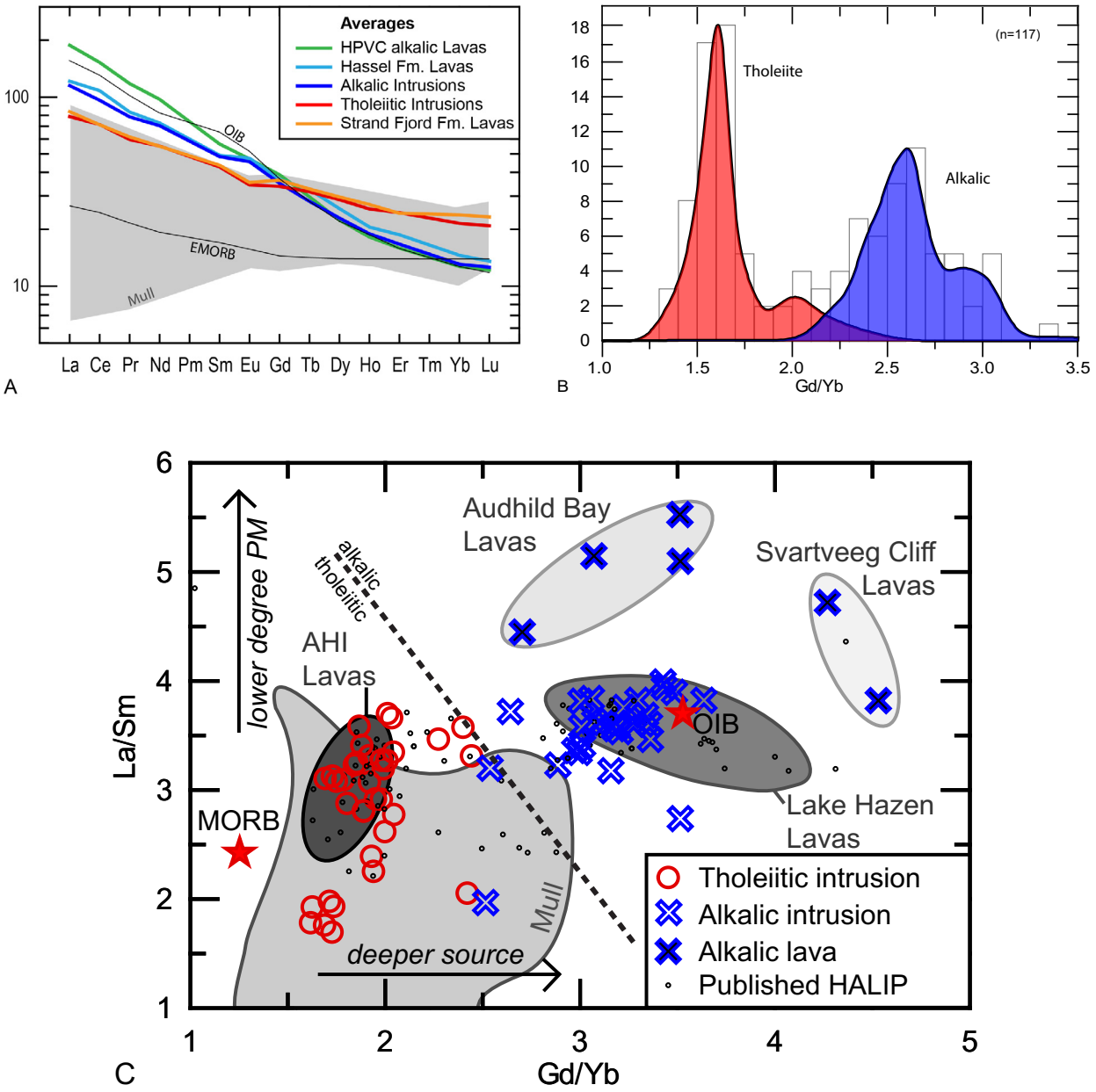

Figure 2.9 a) Calculated average REE patterns for the Canadian HALIP samples, normalized to chondrite Sun and McDonough (1989). Alkalic lavas (Hassel Fm. from Estrada 2014) and intrusions are parallel, while Audhild Bay lavas are more enriched in LREE. The average REE pattern for the tholeiite intrusions of the HALIP parallel the average of the Axel Heiberg Island lavas (e.g. Strand Fjord Fm and Isachsen Fm. basalts, from Jowitt et al. 2014). OIB and EMORB from Sun and McDonough (1989). Mull lavas from Kerr et al. (1999). **b)** Histogram and kernel density plot of Gd/Yb variations for all HALIP samples with full REE analyses. Kernel density estimator plotted using Vermeesch (2012). Data from Estrada (2014), Estrada and Henjes-Kunst (2004), Kontak (2001), and Jowitt et al. (2014). **c)** La/Sm versus Gd/Yb for all HALIP samples. Alkalic basalts are in the lower degree partial melt and deeper source quadrant, with separate fields for the ca. 80 Ma volcanics of Audhild bay and Svartveeg Cliffs. The distribution of lavas from Axel Heiberg Island (AHI) and Lake Hazen Lavas (Hassel Formation) are outlined as fields and overlap the majority of intrusive samples, indicating a common genesis. Mull lavas from (Kerr et al. 1999); HALIP data from Estrada (2014), Kontak (2001), and Jowitt et al. (2014).

make a statistical assessment of this ratio within Canadian HALIP samples (Fig. 2.9b). There are two distinct peaks (tholeiitic: $\mu = \sim 1.6 \pm 0.4$, n = 78; alkalic: $\mu = \sim 2.6 \pm 0.6$, n = 64) with minimal overlap at the 95% confidence level, indicating distinct magma generation conditions.

2.6.4 Sr-Nd tracer geochemistry

εNd_{90} values (Table 2.1; Fig. 2.10) range from 0.8 to 7.1, compositions indicative of long-term Sm/Nd depletion relative to bulk earth. $^{87}Sr/^{86}Sr_{90}$ range widely from 0.70358 to 0.70835. The less altered alkalic lava succession at Audhild Bay (DMD143D; Fig. 2.1) has the least radiogenic Sr of this sample suite and plots closest to the MORB field (Fig. 2.10). The altered lavas of Svartveeg cliffs (see Fig. 2.1) have among the most radiogenic Sr of samples analysed (Fig. 2.10). The results overlap and extend, to more depleted Nd isotopic compositions, the data recently obtained by Estrada et al. (2015) for HALIP magmas. This selective enrichment in radiogenic Sr evident in many of the Sverdrup Basin magma (Fig. 2.10) is likely due to

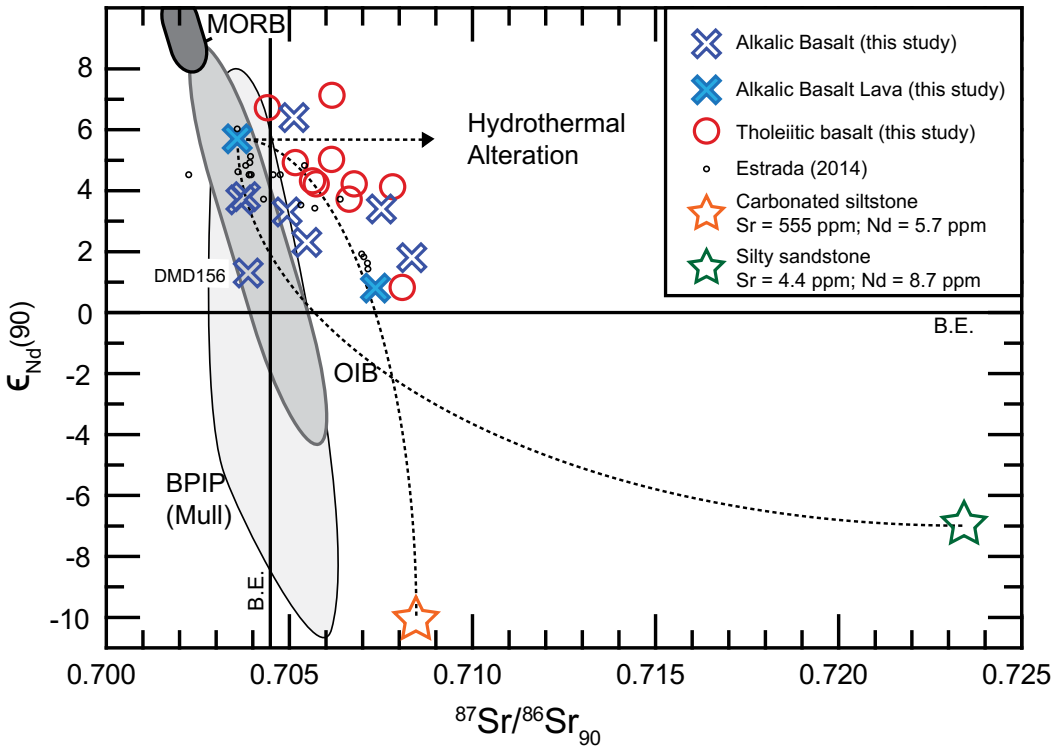

Figure 2.10 Sr-Nd isotopic variation of the Canadian HAILP samples. ϵ_{Nd} and $^{87}Sr/^{86}Sr$ both calculated to a uniform emplacement age of 90 Ma. Previously published HALIP isotopes from Estrada (2014). The mantle array defined by the MORB and OIB fields, with basalts from Mull (Hole et al., 2015; Kerr et al., 1995). Sr-Nd isotopic ratios of two Sverdrup Basin sediments also given, along with their concentrations, and potential contamination vectors. B.E. – Bulk Earth. DMD156 is this suite's most primative sample with an Mg# = 51.

Table 2.1 - Sr-Nd isotope systematics

Sample	Rb (ppm)	Sr (ppm)	$^{87}Rb/^{86}Sr$	$^{87}Sr/^{86}Sr$	$(^{87}Sr/^{86}Sr)_{90}$	Sm (ppm)	Nd (ppm)	$^{147}Sm/^{144}Nd$	Signal ^{144}Nd (V)	$^{143}Nd/^{144}Nd$	$(^{143}Nd/^{144}Nd)_{90}$	εNd	$εNd_{t=90Ma}$
Basalts (this study)													
DMD1	20.5	266	0.2173 ± *6*	0.706458 ± 10	0.706187 ± 13	6.4	25.6	0.1566	1.9	0.512970 ± *10*	0.512878 ± 30	6.5	7.1 ± 0.6
DMD2	39.9	329	0.3422 ± *4*	0.707080 ± 6	0.706650 ± 9	8.5	35.4	0.1510	0.8	0.512795 ± *9*	0.512706 ± 23	3.1	3.7 ± 0.5
DMD26	30.9	483	0.1807 ± *4*	0.705169 ± 6	0.704943 ± 8	7.7	33.9	0.1428	0.2	0.512770 ± *10*	0.512686 ± 26	2.6	3.3 ± 0.5
DMD28	18.1	570	0.0898 ± *6*	0.705243 ± 5	0.705127 ± 9	7.7	34.9	0.1396	1.0	0.512924 ± *23*	0.512842 ± 33	5.6	6.4 ± 0.6
DMD35	22.9	240	0.2693 ± *6*	0.707133 ± 14	0.706791 ± 17	6.1	23.0	0.1671	3.8	0.512827 ± *6*	0.512729 ± 30	3.7	4.2 ± 0.6
DMD107B	16.4	416	0.1110 ± *6*	0.705622 ± 9	0.705480 ± 12	5.8	26.3	0.1389	3.3	0.512714 ± *5*	0.512632 ± 31	1.5	2.3 ± 0.6
DMD113M	16.1	662	0.0686 ± *6*	0.707603 ± 4	0.707514 ± 7	11.1	46.4	0.1499	1.6	0.512778 ± *7*	0.512690 ± 18	2.7	3.4 ± 0.4
DMD114M	6.8	188	0.1023 ± *15*	0.704552 ± 20	0.704421 ± 28	4.7	15.7	0.1883	4.1	0.512968 ± *4*	0.512857 ± 39	6.4	6.7 ± 0.8
DMD133	15.3	209	0.2066 ± *8*	0.706431 ± 7	0.706170 ± 12	5.2	18.3	0.1801	1.3	0.512877 ± *12*	0.512771 ± 37	4.7	5.0 ± 0.7
DMD135	6.2	177	0.0985 ± *17*	0.705784 ± 5	0.705656 ± 22	4.2	15.3	0.1707	1.7	0.512833 ± *6*	0.512732 ± 44	3.8	4.3 ± 0.9
DMD141	33.2	471	0.1991 ± *4*	0.708353 ± 3	0.708100 ± 7	6.9	29.5	0.1468	0.1	0.512644 ± *40*	0.512558 ± 48	0.1	0.8 ± 0.9
DMD143D	46.2	777	0.1678 ± *2*	0.703787 ± 4	0.703579 ± 5	9.5	52.8	0.1136	4.9	0.512872 ± *10*	0.512805 ± 21	4.6	5.7 ± 0.4
DMD147	22.8	195	0.3301 ± *6*	0.705604 ± 10	0.705185 ± 14	6.2	23.2	0.1692	1.5	0.512865 ± *8*	0.512765 ± 30	4.4	4.9 ± 0.6
DMD153B	16.4	316	0.1461 ± *7*	0.707543 ± 4	0.707356 ± 10	7.0	34.3	0.1279	7.2	0.512631 ± *3*	0.512556 ± 26	-0.1	0.8 ± 0.5
DMD156	10.2	732	0.0395 ± *10*	0.703927 ± 6	0.703880 ± 14	7.2	37.6	0.1211	2.0	0.512652 ± *7*	0.512581 ± 26	0.3	1.3 ± 0.5
DMD157M	28.1	297	0.2667 ± *5*	0.706094 ± 6	0.705754 ± 9	6.9	28.4	0.1529	2.8	0.512818 ± *5*	0.512728 ± 26	3.5	4.2 ± 0.5
DMD160	22.7	130	0.4945 ± *8*	0.708458 ± 13	0.707838 ± 18	4.0	14.1	0.1814	2.2	0.512832 ± *8*	0.512725 ± 45	3.8	4.1 ± 0.9
DMD172	21.4	420	0.1438 ± *5*	0.708528 ± 4	0.708349 ± 8	6.3	29.0	0.1377	19.9	0.512686 ± *2*	0.512605 ± 28	0.9	1.8 ± 0.6
Crustal Rocks													
DMD160CR	53.6	4	34.52 ± *19*	0.723450 ± 9	0.723450 ± 9	1.7	8.7	0.1221	11.2	0.512232 ± *3*	0.512160 ± 105	-7.9	-6.9 ± 2.1
DMD141CR	27.2	555	0.1385 ± *4*	0.708459 ± 4	0.708459 ± 4	1.0	5.7	0.1074	0.3	0.512060 ± *20*	0.511997 ± 184	-11.3	-10.1 ± 3.6
Bathurst Nephelinites*													
BI-15	28.7	665	0.1217 ± *4*	0.703829 ± 3	0.703677 ± 6	6.8	41.8	0.1026	5.3	0.512766 ± *4*	0.512706 ± 26	2.5	3.7 ± 0.5
BI-5	33.7	629	0.1512 ± *3*	0.703993 ± 12	0.703800 ± 13	6.8	43.2	0.0988	6.0	0.512770 ± *3*	0.512712 ± 27	2.6	3.8 ± 0.5

*Samples collected and powdered by Mitchell and Platt (1984). Sr-Nd isotopes ran by the present study
All errors reported as $2\sigma_n$
Isotopic ratios calculated to a uniform 90 Ma eruption age

hydrothermal alteration and assimilation of high $^{87}Sr/^{86}Sr$ local crustal rocks (silty sandstone: 0.72345 ± 0.9), which contain between 4.4 to 555 ppm Sr (Table 2.2; Fig. 2.10). Assimilation of crustal rocks is also apparent in other parts of the HALIP (Estrada, 2015). As εNd values of Sverdrup Basin sediments range from -2.9 to -24.2 (Patchett 2004), the magnitude of the effects of crustal assimilation on Nd isotope systematics varies widely on the contaminant. There is no Nd-Sr isotopic distinction between the alkali and tholeiitic basalts, other than tholeiites having slightly more radiogenic strontium, indicating that they are derived, overall, from similar sources and that their isotopic diversity is strongly controlled by crustal assimilation.

2.6.5 Screening for Crustal Contamination

Thorough investigation of the trace-element and isotope geochemistry of the Sverdrup Basin magmas was undertaken to screen out contaminated samples with the aim of determining the least contaminated subset for REE inversion (McKenzie and O'Nions, 1991). This was accomplished in three stages. The majority of samples considered have > 5 wt% MgO and < 3 wt% loss on ignition (LOI). Notable exceptions shall be discussed.

First, the samples were assessed on a Th/Yb vs. Nb/Yb plot following Pearce (2008; Fig. 2.8a), where the least contaminated magmas plot within the 'mantle array' tramlines. Any crustal contamination creates a high angle mixing line in the positive Th/Yb direction, since assimilation of continental crust adds more Th to the magma relative to Yb and Nb (Pearce, 2008).

Samples that plot outside the 'mantle array' were marked as suspect for contamination in the second stage of screening, which focused on Nd-Sr isotopic parameters (Fig. 2.10). As expected, the contaminated samples from stage one all have enriched $^{87}Sr/^{86}Sr$ and low relative εNd, since continental crust is enriched in $^{87}Sr/^{86}Sr$. Hydrothermal alteration exchanges Sr between crustal rocks (4.4 to 555 ppm; Table 2.2) and drives this ratio in a positive direction (sub-horizontal in Nd-Sr isotope space). The isotopic diversity observed in the local crust analysed here (Fig. 2.10) indicates that crustal assimilation will generate vectors of significantly different slope. This variation, in addition to the likely operation of hydrothermal alteration

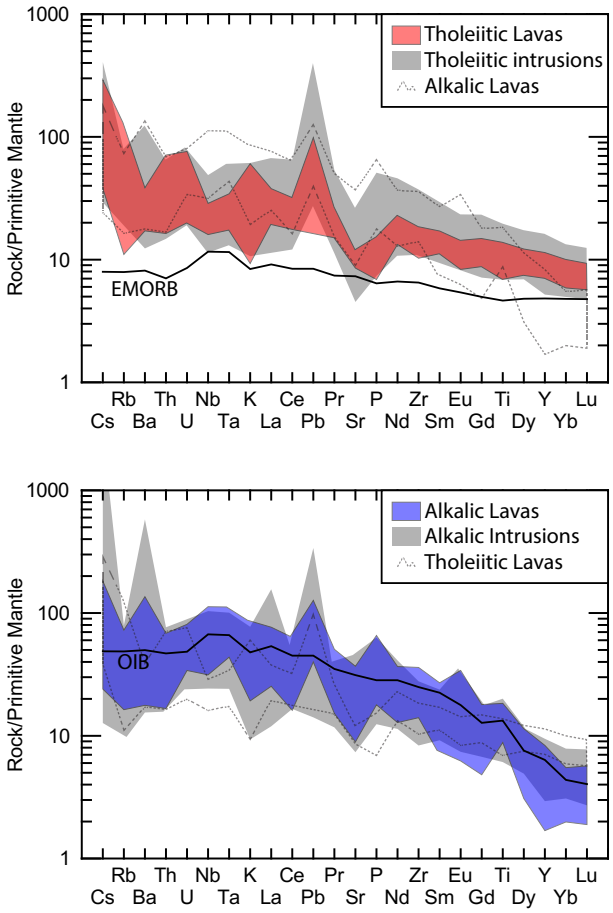

Figure 2.11 Multi-element plots normalized to primitive mantle values of Sun and McDonough (1989). Fields outline the full range of normailized compositions from this and other studies: Jowitt et al (2014); Estrada 2015; Estrada and Henjes-Kunst (2013).

Table 2.2 - Crustal sample geochemistry

	DMD134CR sandstone	DMD141CR calcified siltstone	DMD160CR silty sandstone	DMD164CR sandstone
Ba	86.4	1249	238	27.7
Ce	4.6	8.7	18.7	2.5
Hf	2.8	0.44	4.5	1.5
Nb	8.0	3.6	14.6	4.3
Nd	2.4	5.7	8.7	1.0
Pb	6.9	4.0	3.1	1.0
Rb	13.9	27.2	53.6	0.4
Sr	BDL	555	4.4	BDL
Eu	0.07	0.37	0.34	0.10
Ta	0.57	0.24	0.81	0.35
Th	1.0	1.2	3.1	1.1
U	0.32	1.2	1.9	0.34
V	73.4	52.9	158	42.8
Zr	97.1	16.8	163	57.2
εNd	-	-10.1 ± 3.6	-6.9 ± 2.1	-
$^{87}Sr/^{86}Sr$	-	0.70846 ± 0.6	0.72345 ± 0.9	-

Results by ICP-MS and reported in ppm

BDL - below detection limit

(identified petrographically as sericite and chlorite) means that precise quantitative modelling of the contamination process is not straightforward nor is it a goal of this paper. Rather we focus on modelling the least contaminated magmas to invert their conditions of melting.

All samples that clustered in the isotopically "enriched" Nd-Sr isotope quadrant were flagged as potentially contaminated by additional of crustal components. Next, all samples were plotted on a two ratio plots (LOI vs. 1/Sr; 1/Sr vs $^{87}Sr/^{86}Sr$). All flagged samples from the previous steps clustered together and were excluded from further consideration. Finally, individual multi-element diagrams, normalized to primitive mantle (Sun and McDonough, 1989), were assessed for overall smoothness. Plots of mobile elements vs Th/Yb also helped discriminate which samples were hydrothermally altered, since large deviations from the mantle array (between MORB and OIB) indicate potential alteration. The use of ratio plots to determine large relative deviations (spikes) in LILE (e.g. Fig. 2.8b) confirmed many samples as altered that were suspected through petrographic analysis.

Most of the suspect samples from previous screening stages have erratic patterns when plotted on a multi-element diagram (Fig. 2.11). The samples with the smoothest multi-element patterns were considered for REE inversion modelling. This stage identified a few additional samples as contaminated that were not suspects in previous stages of screening, on the basis of elevated large ion lithophile elements (LILE; e.g. Rb, Sr, Pb, and K), which are mobile in hydrothermal fluids, and negative Nb anomalies, indicative of crustal assimilation.

HALIP tholeiites appear to have experienced a higher degree of crustal contamination than the alkalic basalts, since they have relatively lower concentrations of incompatible trace-elements (e.g., Th and Nb) and are hence more sensitive to crustal input than alkali basalts, as noted in other LIP studies (e.g., Kerr, 1995; Farmer, 2014). As such, more alkalic basalts passed the crustal contamination screening process, resulting in more alkalic basalts are destined for inversion modelling than the tholeiitic compositions (following McKenzie and O'Nions, 1991; Section 2.6.7), although the effects of alteration and contamination are also clearly visible in some alkali magmas (e.g. Fig. 2.8b).

2.6.6 Screening for Fractional Crystallization of Clinopyroxene

As the REE inversion model of Mckenzie & O'Nions (1991) uses the primitive composition of the melt to invert for source melting parameters, a fractionation correction is required to account for any alteration of the relative REE abundances due to fractional crystallization. The effects of both olivine and clinopyroxene fractionation are clearly seen in our HALIP magmas (Fig. 2.6; Section 6.1). Based on MgO-CaO systematics, for alkalic basalts, clinopyroxene begins to fractionate at around 5 wt% MgO, while the tholeiite inflection point is at about 4.5 wt% MgO. The LREE are 2 times more compatible than Nd and 10 times more compatible than Lu in clinopyroxene (Gibson and Geist, 2010) driving the LREE concentration of the fractionated melt down and altering the overall REE ratios. We therefore only invert samples with MgO greater than these values for both tholeiites and alkaline basalts. This ensures that only olivine is the primary phase crystalizing. The model assumes that the removal of olivine does not affect

the trace-element ratios of the melt (McKenzie and O'Nions, 1991). Once these conditions are met, the fractionation correction (F) is a satisfactory estimate of the amount of olivine removal from the primary melt. The only samples that were inverted that contained less than 5 wt% MgO were the Audhild Bay lavas (DMD143A and D). This was attempted because these were the only "uncontaminated" lava samples available for inversion and comparison with the intrusives. These samples have slightly low CaO at a given MgO and relatively high $[La/Sm]_N$ that may indicate the effects of pyroxene fractionation and so any applied fractionation correction (made by the inversion calculation) will induce potential uncertainty. As such, the results from these samples will be treated as less reliable than those that have experienced olivine fractionation only.

2.6.7 REE Inversion Modelling

After rigorous screening for crustal contamination, 24 basalts from this and previous studies (Estrada, 2015; Evenchick et al., 2015; Jowitt et al., 2014; Kontak et al., 2001; Mitchell and Platt, 1984) that contained >5 wt% MgO were used for REE inversion modelling (results summarized in Table 2.3). Ten of the modelled samples are extrusives and 14 were intrusives. The purpose of the modelling, in this study, was to obtain an estimate of the depth of termination of melting, where upwelling mantle encounters the rigid lithosphere, and hence of "lid" thickness. We also constrained the extent of melting from the calculations. Examples of the graphical output for the inversion modelling for the HALIP are given in Figure 2.12. Plots in column A compare the actual and modelled concentration of each REE (1σ error bars), with plots in B showing other trace-elements of varying incompatibility. Plots in column C illustrate the estimated melt fraction versus depth curve, which indicates the depth of melt initiation, the modelled melt fraction, and the depth to the top of the melt column where the intersection of y-axis with the x-axis gives the depth to the base of the lithosphere.

One of the main uncertainties of the inversion approach for this sample set is their relatively fractionated nature. We make a correction to the REE concentrations based on the iron and magnesium content of the rock samples following McKenzie and O'Nions (1991). The estimated

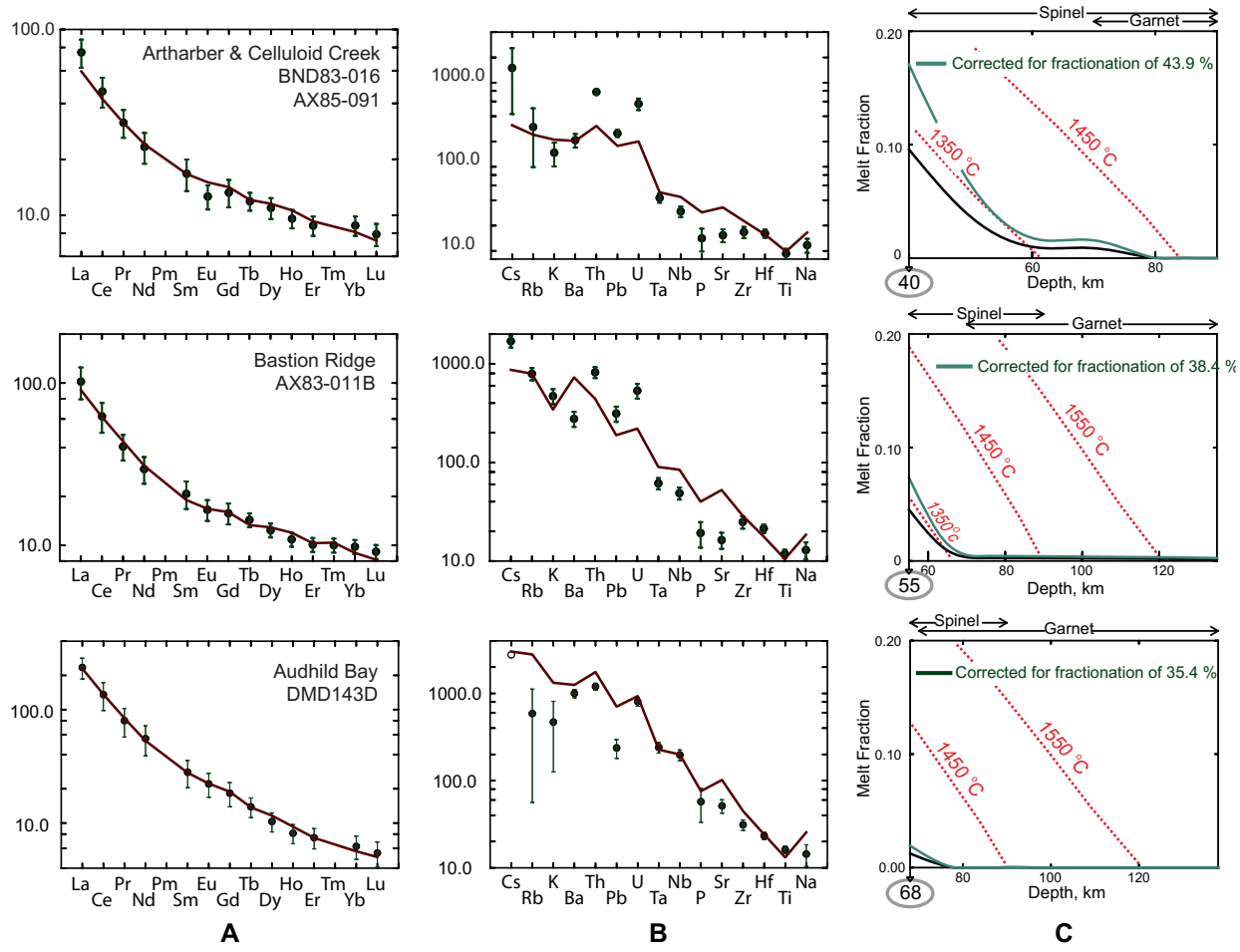

Figure 2.12 REE inversion model graphical output from INVMEL for select HALIP basalts. Plots in column A compare actual and modelled concentration of each REE (1σ error bars). Plots in column B compare actual and modelled trace-elements of varying incompatibility. Plots in column C are the melt fraction versus depth curve, which outputs the depth of melt initiation (curve leaves x-axis), the modelled melt fraction (curve intersects y-axis), and the lithospheric thickness (where the y-axis intersects the x-axis), circled in grey. Only samples greater than 5 wt% MgO were inverted to ensure that olivine is the only fractional crystallization phase. Inverted samples from this study (DMD143D), and Jowitt et al. (2014).

amounts of olivine fractionation from 35.4% to 58.4%, where the lower values correspond to the alkalic basalts and higher values to the tholeiites.

The resulting estimates for lithospheric thicknesses for magmas produced around the Canadian HALIP vary from 40 to 68 km thick (Fig. 2.13). Six strongly depleted tholeiites appear to have been generated beneath quite thin lithosphere (40-42 km). Other tholeiites formed beneath areas with lid thicknesses between 55 km and 60 km thick. As expected, all the alkalic basalts are generated beneath thicker lithosphere that ranges from 60 to 68 km thick. The base of melt

Table 2.3 - REE inversion modelling results

Sample no.	Unit type	Magma Type	Data Source	Latitude (degrees N)	Longitude (degrees W)		MgO (wt%)	$(Sm/Yb)_n$	La/Sm	Gd/Yb	Lid Thickness	Base of melt	Melt Thickness	Age (Ma)	2σ
AX85-091	Lava flow	tholeiite	1	80.5870	95.4740		5.88	1.81	3.08	1.84	40	90.00	2.20	-	
BND83-016	Lava flow	tholeiite	1	80.5390	94.8100		5.56	1.84	3.13	1.79	40	90.00	2.22	83.8	± 1.2
DMD114M	sheet	tholeiite	TS	79.8558	82.5301		6.7	1.75	1.69	1.73	42		-	-	
DMD147	sheet	tholeiite	TS	81.0912	85.7599		6.14	1.98	2.38	1.93	42		-	116.8	± 1.8
AX83-011B	Lava flow	tholeiite	1	79.3500	90.7830		4.95	2.03	3.39	1.94	55	135.00	2.24	95 ‡	
AX83-017	Lava flow	tholeiite	1	79.3500	90.7830		4.15	1.88	2.82	1.86	55	135.00	2.24	95 ‡	
AX83-028	Lava flow	tholeiite	1	79.3500	90.7830		4.28	1.90	3.06	1.90	55	135.00	2.24	95 ‡	
AX83-021	Lava flow	tholeiite	1	79.0000	90.7830		5.14	1.83	3.21	1.85	55	135.00	2.24	95 ‡	
AX85-063	dyke	tholeiite	1	79.4360	87.6640		6.28	1.65	2.24	1.82	55	135.00	-	-	
AX85-024	dyke	tholeiite	1	80.6940	91.7250		5.09	2.85	2.60	2.82	59	119.00	0.42	-	
AX85-037	dyke	tholeiite	1	80.6990	92.3020		4.78	2.78	2.45	2.50	59	119.00	0.42	128.2	± 2.1
SE 23/99	Lava flow	alkalic basalt	2	82.1477	80.6990	*	4.9	3.38	3.73	3.03	62	92.00	0.54	-	
SE 41/99	Lava flow	alkalic basalt	2	82.1477	67.9783		4.86	3.38	3.82	3.05	62	92.00	0.54	-	
SE 42/99	Lava flow	alkalic basalt	2	82.1453	67.9868		4.93	3.32	3.74	2.95	62	92.00	0.54	97.9	± 2
EL84-015	sill	alkalic basalt	1	82.1950	68.4690		5.16	3.84	3.61	3.33	63	145.00	0.40	-	
EL84-056	intrusive rock	alkalic basalt	1	82.2220	68.2890		4.85	3.52	3.82	3.17	63	145.00	0.40	-	
434009	intrusion	alkalic basalt	3	83.5000	34.0000	*	5.63	3.30	3.19	2.85	65	115.00	0.19	90.6	± 4
434011	intrusion	alkalic basalt	3	83.5000	34.0000	*	5.67	3.46	3.28	2.94	65	115.00	0.19	-	
DMD26	sheet	alkalic basalt	TS	82.0096	70.0337		4.72	3.90	3.90	3.49	65	145.00	0.19	-	
DMD28	sheet	alkalic basalt	TS	82.0049	69.9206		5.08	3.93	3.99	3.42	65	145.00	0.19	-	
DMD143D	Lava flow	alkalic basalt	TS	81.3993	90.1174		4.63	4.27	5.53	3.51	68	98.00	0.10	78.4	± 0.1
DMD156	sheet	alkalic basalt	TS	81.5658	91.3553		10.48	4.36	6.11	3.60	68	98.00	0.10	-	
BI-15	dyke	Nephelinite	4	75.1067	98.1808	*	11.788	6.32	7.91	5.38	70	150.00	0.08	50 ‡	
BI-5	dyke	Nephelinite	4	75.1056	98.2297	*	10.700	8.07	7.49	6.65	70	150.00	0.08	50 ‡	

Data source: TS - This Study; 1 - Jowitt et al. (2014) and Villeneuve and Williamson (2006); 2 - Estrada (2015); 3 - Kontak et al. (2001); 4 - Mitchell and Platt (1984); 5 - Evenchick et al. (2015)

*Lat/Long not published - estimated from positions on sample maps published with results

[I] Lid thickness infered from curve on Lid thickness vs $[Sm/Yb]_N$ **(Fig. 2.13).** Normailized to McDonough and Sun (1989)

[‡] approximate age from biostrat or unreliable geochronology

Table 2.3 - REE inversion modelling results (continued)

Sample no.	Unit type	Magma Type	Data Source	Latitude (degrees N)	Longitude (degrees W)		MgO (wt%)	$(Sm/Yb)_n$	La/Sm	Gd/Yb	Lid Thickness		Base of melt	Melt Thickness	Age (Ma)	2σ
DMD-160	sheet	tholeiite	TS	80.3443	88.4817		5.74	1.73	1.92	1.63	42	†	-	-	120.3	± 0.8
DMD170	sheet	tholeiite	TS	80.1451	85.1280		2.12	1.83	3.10	1.70	44	†	-	-	90.2	± 3.6
C 107586	Lava flow basalt	tholeiite	2	79.5701	87.4860	*	5.13	1.93	3.23	1.93	45	†	-	-	100.7	± 5.8
DMD145M	dyke	tholeiite	TS	81.0605	86.8396		4.94	1.91	3.22	1.85	45	†	-	-	121.1	± 1.9
AX83-60	-	tholeiite	1	79.4167	92.2833		-	2.10	-	-	48	†	-	-	80.7	± 1.1
056A01	sheet	tholeiite	5	78.7492	100.3881		4.87	2.01	3.11	1.89	52	†	-	-	-	
059A02	sheet	tholeiite	5	78.7576	100.4142		4.56	2.04	3.00	2.03	52	†	-	-	-	
062A01	sheet	tholeiite	5	78.8228	103.8813		4.79	2.03	2.94	2.08	52	†	-	-	120.8	± 0.8
098A01	lava	tholeiite	5	78.7810	100.7963		4.15	2.02	3.10	1.93	52	†	-	-		
DMD157M	sheet	tholeiite	TS	80.8193	91.8029		4.46	2.06	3.26	2.01	52	†	-	-	-	
DMD154M	sheet	tholeiite	TS	81.5649	91.3572		4.8	2.79	3.57	2.40	59	†	-	-	116.0	± 3.0
DMD124M	sheet	tholeiite	TS	79.8134	86.4185		2.21	2.85	3.72	2.64	60	†	-	-	91.7	± 1.1
EL84-249	sill	alkalic basalt	1	80.6330	85.3330		5.29	3.09	3.47	2.81	63	†	-	-	-	
DMD143A	lava	alkalic basalt	TS	81.3986	90.1095		3.53	3.27	4.44	2.69	64	†	-	-	78.8	± 0.1
DMD173	sheet	alkalic basalt	TS	80.0206	86.3836		5.8	3.35	3.23	2.89	64	†	-	-	91.9	± 0.8
SE 15/99	lava	alkalic basalt	2	82.3300	66.1525		4.84	3.59	3.65	3.17	65	†	-	-	97.9	± 2.0
SE 17/99	lava	alkalic basalt	2	82.3300	66.1525		4.51	3.51	3.62	3.08	65	†	-	-	94.4	± 2.2
SE 12/99	lava	alkalic basalt	2	81.9528	70.9476	*	3.79	4.29	3.43	3.68	68	†	-	-	98.2	± 2.0
SE 2/99	lava	alkalic basalt	2	82.1595	68.3945		3.68	4.26	3.44	3.67	68	†	-	-	94.1	± 2.1
DMD153B	lava	alkalic basalt	TS	81.2198	92.0361		4.27	5.10	4.72	4.28	70	†	-	-	-	

Data source: TS - This Study; 1 - Jowitt et al. (2014) and Villeneuve and Williamson (2006); 2 - Estrada (2015); 3 - Kontak et al. (2001); 4 - Mitchell and Platt (1984); 5 - Evenchick et al. (2015)

*Lat/Long not published - estimated from positions on sample maps published with results

† Lid thickness infered from curve on Lid thickness vs $[Sm/Yb]_N$ **(Fig. 2.13).** Normailized to McDonough and Sun (1989)

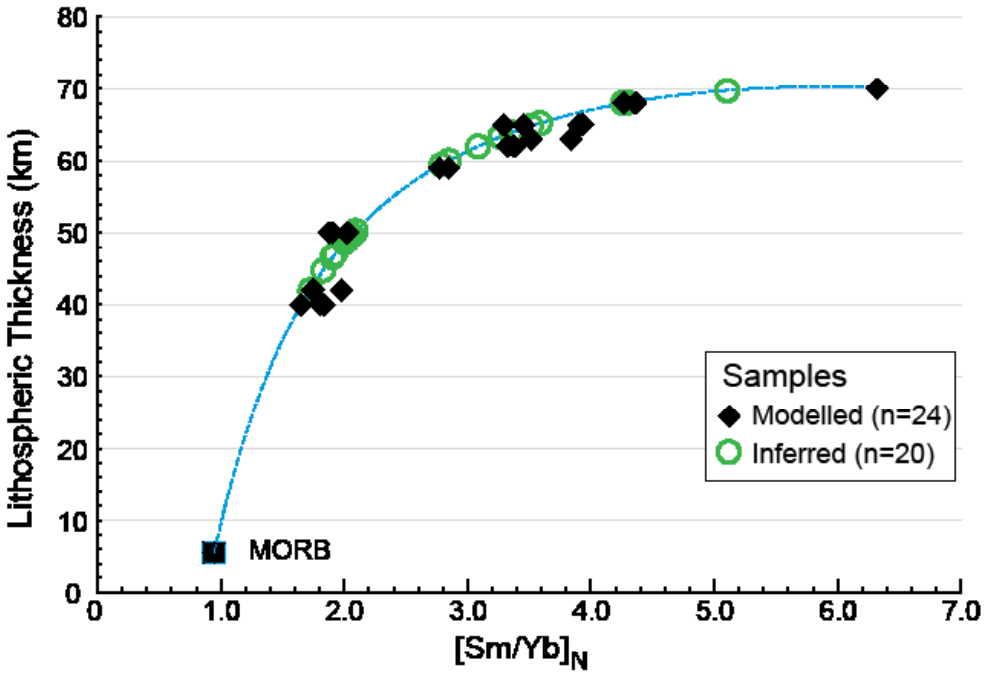

Figure 2.13 Lithospheric thickness versus Sm/Yb normalized to chondrite (Sun and McDonough, 1989). Inverted samples in black diamonds with curve fitted; samples with inferred lithospheric lid thicknesses, from the intersection of their measured Sm/Yb with the curve are plotted as green circles (See text). There is a notable gap in lithospheric thickness between about 52 and 58 km.

column (the initiation of melting) is also output by the REE inversion model, and ranges from 90 to 145 km depth, with a total melt thickness of 0.08 to 0.54 km for alkalic basalt samples and 0.42 to 2.24 km for the tholeiite samples. These estimates clearly distinguish the melting conditions for the HALIP magmas from those of MORB, which typically have basal melt columns of less than 80 km and melt thicknesses of White et al. (2001).

Unfortunately, most of the geochronology samples from the HALIP are not suitable for REE inversion modelling as they have been fractionated to significantly below 5 wt% MgO. To compensate for the paucity of age constraints on how lithospheric thickness varies in the Sverdrup Basin magmas, we use the systematic relationship between lid thickness – calculated from REE inversion – and the slope of the MREE to HREE portion of the REE pattern, expressed as $[Sm/Yb]_N$ (Fig. 2.13) to crudely estimate the lid thickness for samples not perfectly suited to full inversion. As REEs are immobile elements, and they have similar incompatibilities, fractionation and alteration will little affect their relative ratios, making this interpolation reasonable for fractionated samples. In this way, lid thickness can be estimated for samples

where geochronological information is available (red circles, Fig. 2.13 – ages with respect to lithospheric thickness addressed further in Chapter 3). With the additional low MgO samples, 43 lithospheric thickness values were obtained by interpolation of their Sm/Yb_N ratios to the curve in Fig. 2.13. Of these samples, 14 have reliable ages and the other six were chosen to extend the geographic range of the REE inversion modelling.

We also attempted to model the lid thickness, from published geochemistry, of the Alpha Ridge, a submarine volcanic edifice off the northwest coast of Ellesmere Island (Fig. 2.1), which is spatially associated with the HALIP and has been identified by some authors as being close to the site of the proposed plume head (Fig. 2.1; Ernst and Buchan, 2006). The REE geochemistry of the available Alpha Ridge samples – 3 heavily altered scoraceous basalts sampled close to each other – are incomplete and wildly scattered, with $[Sm/Yb]_N$ values of 1.3 to 3.4 (Van Wagoner et al., 1986). These samples do not allow robust estimates of the lid thickness controlling their melt production.

With a mean lithospheric thickness of 47 ± 4 km (2σ, n = 11) for the thin-lid tholeiities and 64 ± 3 km (2σ, n = 12) for the thicker-lid alkaline basalts, there is a notable lack of magmas generated beneath lithospheric thicknesses that are intermediate between these depths (between ~50 and 60 km thickness; Fig. 2.13). The consequence of this bimodality in lid thicknesses is the clear separation between magma types noted in the geochemistry of the Canadian HALIP (Section 6.3; Figure 2.9c). Although uncertainties inherent in this model are difficult to estimate, the lithospheric thickness estimates all have the same error and are therefore accurate relative to one another. Thus, regardless of errors prescribed to the results, there are two distinct depths of magma generation in the Canadian HALIP.

2.7 Discussion

2.7.1 Fractionation and pressure/depth of magma formation

When comparing the 24 sample REE inversion subset (Section 6.8) to the British Paleogene Igneous Province (BPIP; Figure 2.9a; Kerr et al., 1999, 1995), it is evident that the HALIP tholeiites experienced slightly more olivine fractionation, but are more enriched in LREE, indicating one of the following scenarios: i) a more enriched source; ii) lower degree of partial melting; iii) LREE contamination from crustal assimilation. The alkalic basalts from the two different provinces are also not similar. The slopes of the REE patterns for the alkalic intrusions are much steeper in the HALIP (Fig. 2.9a), indicating smaller volumes of melt, with their lower HREE indicating a deeper source. The lavas from this study have the most extreme LREE/HREE enrichment and overall highest residual garnet signature, with a depth of melt initiation at 98 km, with their melting extent restricted by a 70 km thick lithospheric lid (Fig. 2.13). These lavas are the thickest Cretaceous lithosphere, at the time of melting, of the Canadian HALIP.

Another indication of the effects of crystal fractionation is the presence of europium anomalies in REE patterns. Positive Eu anomalies indicate either plagioclase accumulation or the assimilation of a crustal lithology with a prominent positive Eu anomaly into the melt (through some form of assimilation-fractional crystallisation process); negative Eu anomalies indicate that plagioclase was either removed by fractional crystallization or the assimilation of crust with prominent negative Eu anomalies. Some Canadian HALIP tholeiites have a slight negative Eu anomaly (Eu* for the tholeiites between 0.83 – 1.0, $\mu = 0.91$, $n = 7$) that can be attributed to fractional crystallization and chemical segregation of plagioclase, which would have occurred at upper crustal levels, as indicated by the evolution of CIPW normative mineralogy (Fig. 2.5). On the other hand, a few alkali basalts have a positive Eu anomaly (Eu* between 0.94 – 1.12, $\mu = 1.04$, $n = 17$), the highest from the datasets of Estrada, 2014 & Kontak et al., 2001), consistent with minor plagioclase accumulation, or assimilation of crustal contaminants. Due to these samples passing the rigorous crustal contamination screening of Section 2.6.6, it is likely that these

alkalic basalts experienced minor plagioclase accumulation during a magma chamber phase prior to eruption.

2.7.2 Convecting mantle versus metasomatized lithosphere

An alternative method that explains two contemporaneously generated magma types is that the magmas showing pronounced LREE enrichment (e.g. DMD143A and -D lavas), originated via melting of a metasomatically enriched lithospheric or asthenospheric source. Melting of phlogopite and K-richterite rich veins in the sub continental lithospheric mantle (SCLM) would be evident in the trace-element concentrations of the generated magmas. K, Ba, and Rb are compatible in phlogopite while amphibole preferentially incorporates K, Ba, Sr and the middle REEs (Gd-Er). The high field strength elements (HFSE; spcifically Ti, Nd, and Ta) are also readily incorporated into both phases (Farmer, 2014; and references therein). Therefore, partial melting that completely melts the hydrous phases in these veins would generate enrichment in the aforementioned compatible elements. Partial melting that leaves at least one of these hydrous phases as a residual phase would have relative depletions in these elements. Although there are spikes of LILE for some altered samples, there is no systematic enrichment or depletion of these elements in the Cretaceous magmas of the Canadian HALIP, shown in a multi-element plot (Fig. 2.11) normalized to primitive mantle. The very wide dispersion in Cs and Ba in the alkalic magmas is not accompanied by systematic enrichment in K or Rb, indicating that low-T hydrothermal alteration is the cause of the spread in these elements. Furthermore, of the "minimally contaminated" samples showing any signs of Ba enrichment, there is no evidence of long-term time-integrated Sr or Nd isotopic enrichment that is typically the sign of incorporation of subcontinental mantle lithosphere (e.g. Peate and Hawkesworth, 1996). Finally, during REE inversion moddeling of this sample suite, no hydrous phases were evoked to fit the modelled multi-element data to the observed data (Fig 2.12), which indicates melting from an anhydrous source.

Notwithstanding the lack of geochemical evidence for the involvement of enriched lithosphere

in the source of the HALIP magmas, even the temporal relationship of the magma types are not indicative of a partially metasomatized source. During partial melting of metasomatized lithospheric mantle, where low-solidus hydrous veins are present, the first melt would be dominated by vein input to hybridised peridotite (e.g. Foley, 1992). The initial melts would be highly alkaline basalts, but in the HALIP, tholeiites were formed first, throughout the province (This study; Corfu et al., 2013; Jowitt et al., 2014; Tegner et al., 2011), with no reports of alkalic basalts in the earliest eruptions (ca. 120 Ma). One would expect that repeated melt extraction from the same veined source would produce more trace-element depleted – tholeiitic – magmas with each melting iteration. This is not observed in the overall geochemical trend in the HALIP, which begins as tholeiitic and ends with alkalic basalts over at least 2 pulses (This study; Jowitt et al., 2014). Furthermore, the pre-rifted continental lithosphere beneath the Canadian HALIP was well within Pangea. If there were metasomatized veins within the SCLM, they would have to have been from pre-Pangea formation. Due to super-continent mantle thermal incubation (Jaupart and Mareschal, 2007), the temperature of the SCLM would have been well above the stability temperature of phlogopite (~1000 to 1100 ^{0}C, depending on pressure and volatile content; Foley, 1992). Therefore, all hydrous veins would have melted long before basaltic magma generation of the Cretaceous HALIP. It is for these reasons that we argue for a convecting mantle source for basalt generation, rather than varying degrees of partial melt of a metasomatized SCLM source. As such, we then interpret the varying elemental geochemistry of the HALIP magmas as reflecting, predominantly, the varying thickness of the lithospheric lid at the site of melting.

2.7.3 Spatial variations in lithospheric thickness during magma generation and relation to regional geology

Intrusive sheets, dykes, and sills can travel more than 250 km through a sedimentary basin (LeCheminant and Heaman, 1989; Reidel et al., 2013) and so only lava flows can be used as geographic pin-points when discussing source characteristics or the thickness of the lithosphere through which the flow was emplaced. The 18 extrusive basalts that give estimates of the

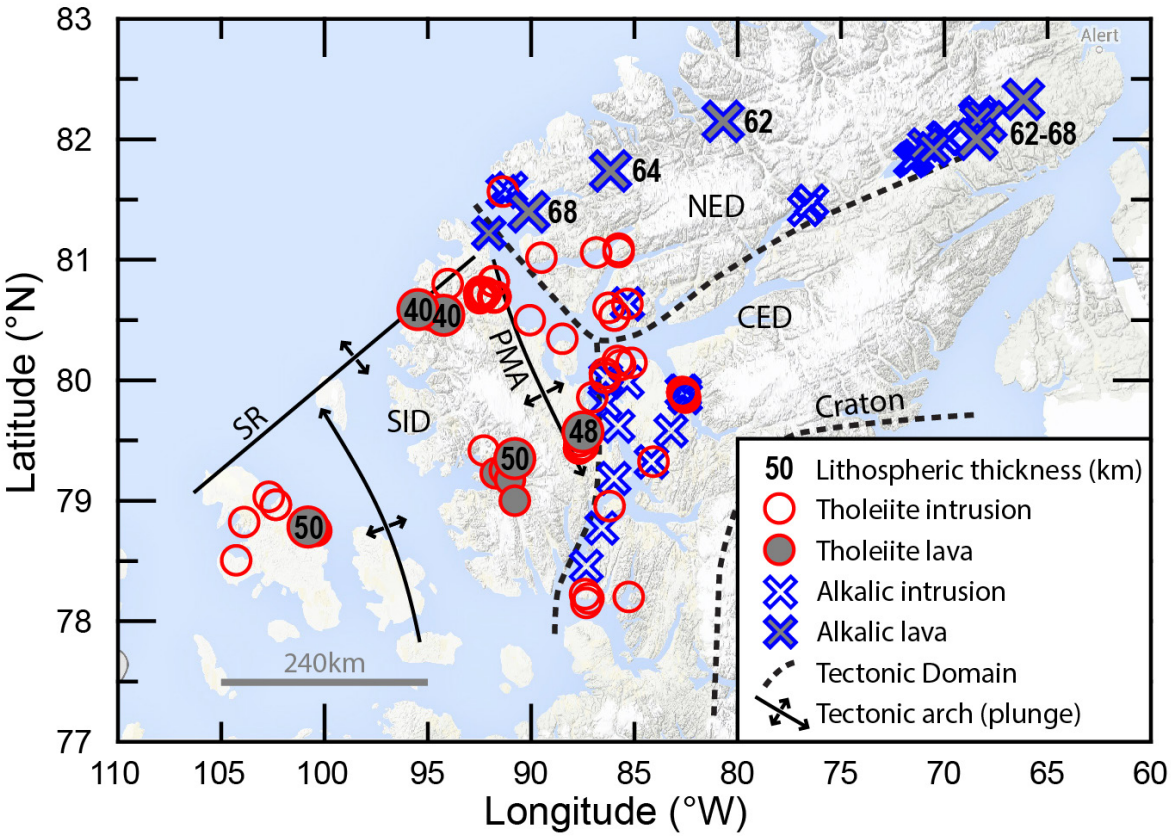

Figure 2.14 Spatial distribution map of Cretaceous Sverdrup Basin magmatic compositions, separated into lavas and intrusions, overlain with tectonic domains and structural highs (from Trettin, 1991) that separate the magma types well. Tholeiitic lavas are restricted to the Sverdrup Islands Domain (SID), where rifting was most extensive. Tholeiitic intrusions infiltrate the Northern and Central Ellesmere Island Domains (NED and CED, respectively), but no tholeiitic lavas are present to anchor their geographic source. They can therefore be generated in the SID and injected into the CED and NED. No alkalic basalts are present in the SID. The Princess Margret Arch, a broad anticlinorium bound by normal faults, may have been a structural barrier for alkalic magma migration into the SID. Relevant structural highs parallel sub-Sverdrup tectonics: PMA – Princess Margret Arch; CA – Cornwallis Arch; SR – Sverdrup Rim; IFU – Inglefield Uplift exposes Archean craton (Trettin, 1991). Terrain image from Google Maps (2016).

lithospheric lid thickness are spatially well distributed across the Sverdrup Basin (Fig. 2.14). These lavas are benchmarks for the geographic range of the Cretaceous lithospheric thickness as lavas are less likely than intrusions to travel great distances from thier source. The lavas indicate that the thickness of the Cretaceous lithosphere in the basin centre, Axel Heiberg Island, was between 40 and 55 km thick during magma generation. The lava successions from Audhild Bay and Lake Hazen on the basin margin (Fig. 2.1), Ellesmere Island, indicate Cretaceous lithospheric thickness was 62 to 68 km thick. These modelled lithospheric thicknesses are good geographic benchmarks of the depth of magma generation and are useful comparisons for the

intrusions.

The inferred lithospheric thicknesses at the site of magma generation for the intrusives are systematically distributed in the Canadian HALIP and in general follow the same trend as the lavas. On Ellesmere Island, parent magmas to the intrusions were generated beneath thick lithosphere ($\mu = 63 \pm 5$ km). The sites of HALIP magma intrusion on Ellesmere Island are located to the North of the craton margin (Fig. 2.1), along the continental margin, focussed along the southeast edge of the Sverdrup Basin. The magmas intruding crust beneath Axel Heiberg Island, in the basin centre, were produced beneath thin lithosphere ($\mu = 45 \pm 4$ km), in agreement with the lava successions of the Strand Fjord formation on western Axel Heiberg. A minority of the dykes and sills on western Ellesmere Island were generated beneath thin lithosphere, but there are no tholeiitic lava successions to constrain the proximity of their source and we view it as likely that the magma for these "thin lid" hypabyssal intrusions may have been produced beneath Axel Heiberg Island and injected into the crust of western Ellesmere Island. The location of the thinnest lithosphere (40 km) beneath Axel Heiberg Island is concurrent with the sedimentary depocenter of the Sverdrup Basin and the location of the greatest amount of rifting (Oakey and Stephenson, 2008). Hence, despite the caveats regarding magma transport, our initial survey of the spatial relationships between magma types appear to show trends that are consistent with the acknowledged evolution of the basin.

2.7.4 Tectonic highs from rifting control distribution of magma geochemistry

Previous investigations (e.g., Evenchick et al., 2015; Jowitt et al., 2014) have not focussed on explaining the geographic distribution of the two magma types of the Canadian HALIP. We assert that rift complexes in the Carboniferous to Permian strata of the Sverdrup basin, extant from the initial stages of rifting, created tectonic highs that may control the distribution of magma types in the Canadian HALIP. Rifting initiated in the Carboniferous (~ 340 Ma - Embry 2008), creating the proto-Sverdrup Basin. The four tectonic domains of the Sverdrup Basin parallel these underlying rift structures within the Franklinian Basin, and are separated into the

Northern Ellesmere (NED), Central Ellesmere (CED), Prince Patrick, and Sverdrup Islands Domains (SID; Fig. 2.14; Trettin, 1991). These domains are separated based on structural style. The CED is dominated by reverse faulting, which thrusts the younger strata of the Franklinian and Sverdrup basins on top of the stable tectonic high of the Inglefield Uplift during the Late Cretaceous Eurekan Orogeny (Trettin, 1991). However, the SID is underlain by deep rift structures, being the location of maximum extension in the basin (Oakey and Stephenson, 2008) that were not re-activated by the Eurekan Orogeny. The short timescale of thinning within the basin depocenter on Axel Heiberg Island corresponds to the transition from uplift, sandstone dominated sedimentation, and erosional unconformities (pre-120 Ma), to active subsidence and deep water shale deposition (post-120 Ma; Embry and Beauchamp, 2008) within the Sverdrup Basin.

Within the SID, a rift shoulder formed parallel to the Arctic continental margin, bounded by opposite verging normal faults (the Sverdrup Rim), isolating the Sverdrup Basin from the locus of rifting as the main rift phase began focusing on the Canadian basin (Sweeney, 1985). During rifting, two elongate and parallel horsts formed in a NW trend: Princess Margret Arch and the Cornwall Arch (Fig. 2.1). These tectonic arches have been interpreted geophysically as rifted horsts in pre-Sverdrup sedimentary sequences (Forsyth et al., 1998) and sub-parallel to the 100 km lithospheric thickness contour (Fig. 2.1) as it curves to the NW-SE. The change in orientation parallels the rifting within the Baffin Sea and is evident at the 150km seismic tomography slice (Schaeffer and Lebedev, 2014). At 150 km depth, the entirety of the Sverdrup Basin is disconnected from continental North America by thick lithospheric mantle, but convective mantle flow is connected to W. Greenland. The rift structures within the Sverdrup Basin are potentially the far-field result of extension during the ca. 60 Ma rifting of the Baffin Sea.

The Princess Margret Arch and the Sverdrup Rim mark boundaries between the tholeiitic lavas of Axel Heiberg Island, produced above thin (~45 km) lithosphere and the outpouring of alkalic basalt lavas on western Ellesmere Island above considerably thicker lithosphere (~65 km; Fig.

2.14). These tectonic highs separate the lithospheric thickness modes, and therefore the two magma types, into these geographic ranges (Fig. 2.13; Section 2.4.3). However, the magma-types evident in the intrusions are not as well confined by these tectonic boundaries, with minor intrusions of tholeiite within both the Central and Northern Ellesmere Domains (CED and NED, respectively; Figure 2.14). It is likely that the tholeiites were generated beneath the heavily rifted western margin of Axel Heiberg Island, towards the centre of the Sverdrup Basin and injected laterally into the thicker lithosphere of the CED and NED.

A tectonic model to explain this variability requires two geographically distinct magma production reservoirs, beneath varied lithospheric thickness, and the ability to inject these magmas throughout the Sverdrup Basin. To explore these relationships more, these lavas and intrusions need to be dated using precise geochronological methods to better understand the temporal interplay between the lithospheric lid control on magma production and tectonics. As an example of the complexity already evident, we estimate that a tholeiite dyke generated beneath ~ 60 km of lithosphere was emplaced on Axel Heiberg Island at 128.2 ± 2.1 Ma (AX85-037: Jowitt et al., 2014; Villeneuve and Williamson, 2006). In contrast, a tholeiite from this study (DMD147), in the same vicinity, has an inferred lithospheric lid thickness of 42 km indicating a >15 km change in lithospheric thickness for the tholeiite magma source, if the magmas came from beneath the same melt source. The temporal changes in lithospheric thickness will be addressed in Chapter 3.

2.8 Conclusions

In this study, samples of a geographically, geochemically, and temporally diverse suite of basaltic intrusions and lavas were collected on Axel Heiberg and Ellesmere Islands, Nunavut. This geographic transect was chosen to obtain samples from the margin of the Sverdrup Basin, near continental North America, and the basin center on Axel Heiberg Island, proximal to the proposed plume head off the northwest coast of Ellesmere Island (e.g. Buchan and Ernst, 2006).

The geochemical portion of the project involved a detailed study of the trace-element geochemistry of samples collected from the margins of basaltic dykes and sills, whose quenched margin best preserves the eruptive geochemistry. The HALIP is characterized by a bimodal suite of tholeiitic and alkalic basalts. Magma classification in the suite is best accomplished using immobile trace-element ratios and REE patterns due to the inherent weakness of major-element classification systems that evolve with fractionation. Three nepheline-normative samples from this suite have the same REE patterns as a sample subset classified as alkalic basalts on a Nb/Y vs $Zr/P_2O_5*10^4$ plot (Floyd and Winchester, 1975). The parental magmas of these alkali basalts were likely nepheline-normative, as their REE patterns are indicative of alkalic basalt, yet fractionation has driven these samples to hypersthene-normative. In general, tholeiitic basalts are more likely to have undergone low temperature hydrothermal alteration and assimilation of crustal components due to their lower overall trace-element abundances. Similar geochemical characteristics and levels of crustal contamination are observed in the Mull and Skye lavas of the British Paleogene (e.g. Thompson, 1982; Kerr et al., 1995).

After accounting for the effects of crustal contamination, Sr-Nd isotope systematics indicate the same mantle source was involved in generating both the alkalic and tholeiitic basalts, without the characteristics of long-term source enrichment via earlier subduction-related metosomatism of mantle peridotite. In the absence of evidence for long-term mantle enrichment, we interpret the variations in REE geochemistry as being due to differences in the physical parameters—primarily the lithospheric "lid" thickness — of the melting environment.

Samples deemed 'least contaminated' after a rigorous geochemical screening for crustal contamination were modeled for lithospheric lid thickness following McKenzie and O'Nions (1991). The derived lithospheric thicknesses (depth to top of melting column) were classified into two modes ~65 and 45 km, corresponding to alkalic (60-68 km) and tholeiitic (40-58 km) magma types. 14 of the samples modelled for REE inversion are lavas, whose geographic proximity to their site of magma generation is more reliable than the intrusions. Tholeiitic lavas

are restricted to the basin centre on central Axel Heiberg Island (Oakey and Stephenson, 2008). HALIP intrusive basaltic magmas are systematically distributed and generally follow the same distribution as the lavas, indicating the same controls on magma generation, with minor lateral injection into other domains. The geographic distribution of the two magma types follows the tectonic domains outlined by Trettin (1991), where tholeiites occur mainly in the heavily rifted Sverdrup Island Domain (SID), and the alkalic basalts occur in the Northern and Central Ellesmere Domains (NED and CED, respectively). These domains are delineated by Late Cretaceous to Paleogene tectonics, such as the Princess Margret Arch in the SID and the Eurekan fold-and-thrust belt in the CED, and run parallel to basement Carboniferous to Permian rift structures caused by the opening of the Arctic Ocean (Trettin, 1991). Magma distribution follows tectonic structure, not a linear track as one would expect with a plume.

References

Bouvier, A., Vervoort, J.D., and Patchett, P.J., 2008, The Lu-Hf and Sm-Nd isotopic composition of CHUR: Constraints from unequilibrated chondrites and implications for the bulk composition of terrestrial planets, *Earth and Planetary Science Letters*, v. 273, no. 1-2, p. 48–57.

Bryan, S.E., and Ernst, R.E., 2008, Revised definition of Large Igneous Provinces (LIPs), *Earth-Science Reviews*, v. 86, p. 175–202.

Buchan, K.L., and Ernst, R., 2006, Giant dyke swarms and the reconstruction of the Canadian Arctic islands, Greenland, Svalbard and Franz Josef Land, in: Hanski, E., Mertanen, S., Rämö, T., and Vuollo, J. (Eds.), *Dyke Swarms: Time Markers of Crustal Evolution*, Taylor and Francis Group, London, UK, p. 27–48.

Campbell, I.H., 2007, Testing the plume theory, *Chemical Geology*, v. 241, p. 153–176.

Coffin, M.F., and Eldholm, O., 1992, Volcanism and continental break-up: A global compilation of large igneous provinces, in: Storey, B., Alabaster, T., Pankhurst, R. (Eds.), *Magmatism and the Causes of Continental Break-up*, Geological Society of London Special Publication No. 68, p. 17–30.

Corfu, F., Polteau, S., Planke, S., Faleide, J.I., Svensen, H., Zayoncheck, A., and Stolbov, N., 2013, U-Pb geochronology of Cretaceous magmatism on Svalbard and Franz Josef Land, Barents Sea Large Igneous Province, *Geological Magazine*, v. 150, no. 6, p. 1127–1135.

DePaolo, D.J., and Wasserburg, G.J., 1976, Nd isotopic variations and petrogenic models, *Geophysical Research Letters*, v. 3, no. 5, p. 249–252.

Ellam, R.M., 1992, Lithospheric thickness as a control on basalt geochemistry, *Geology*, v. 20, p. 153–156.

Embry, A., and Beauchamp, B., 2008, Sverdrup Basin, in: Miall, A.D. (Ed.) *Sedimentary Basins of the World*, *Volume 5*, Elsevier Ltd., p. 451–471.

Ernst, R., and Bleeker, W., 2010, Large igneous provinces (LIPs), giant dyke swarms, and mantle plumes: Significance for breakup events within Canada and adjacent regions from 2.5 Ga to the present, *Canadian Journal of Earth Sciences*, v. 47, p. 695–739.

Estrada, S., 2015, Geochemical and Sr-Nd isotope variations within Cretaceous continental flood-basalt suites of the Canadian High Arctic, with a focus on the Hassel Formation basalts of northeast Ellesmere Island, *International Journal of Earth Sciences*, v. 104, no. 8, p. 1981–2005.

Estrada, S., and Henjes-Kunst, F., 2013, ^{40}Ar-^{39}Ar and U-Pb dating of Cretaceous continental rift-related magmatism on the northeast Canadian Arctic margin, *Zeitschrift der Deutschen Gesellschaft für Geowissenschaften*, v. 164, p. 107–130.

Evenchick, C.A., Davis, W.J., Bedard, J.H., Hayward, N., and Friedman, R.M., 2015, Evidence for protracted High Arctic large igneous province magmatism in the central Sverdrup Basin from stratigraphy, geochronology, and paleodepths of saucer-shaped sills, *GSA Bulletin*, p. 1–25.

Farmer, G.L., 2014, Continental basaltic rocks, in: Holland, H.D., Turekian, K.K. (Eds.), *Treatise on Geochemistry, Volume 4*, 2nd Edition, Elsevier Ltd., p. 75–110.

Foley, S., 1992, Vein-plus-wall-rock melting mechanisms in the lithosphere and the origin of potassic alkaline magmas, *Lithos*, v. 28, p. 435–453.

Forsyth, D.A., Asudeh, I., White, D., Jackson, R., Stephenson, R.A., Embry, A.F., and Argyle, M., 1998, Sedimentary basins and basement highs beneath the polar shelf north of Axel Heiberg and Meighen islands, *Bulletin of Canadian Petroleum Geology*, v. 46, no. 1, p. 12–29.

Gibson, S.A., and Geist, D., 2010, Geochemical and geophysical estimates of lithospheric thickness variation beneath Galápagos, *Earth and Planetary Science Letters*, v. 300, p. 275–286.

Gibson, S.A., Geist, D.J., and Richards, M.A., 2015, Mantle plume capture, anchoring, and outflow during Galápagos plume-ridge interaction, *Geochemistry, Geophysics, Geosystems*, v. 16, p. 1634–1655.

Google Maps, 2016, Ellesmere and the Sverdrup Islands, terrain map, retrieved from https://www.google.ca/maps/@80.4432023,-94.8656865,5z/data=!4m2!6m1!1szaoU7Jghh3Io.keFJTViEExQU

Hamilton, M.A., Pearson, D.G., Thompson, R.N., Kelley, S.P., and Emeleus, C.H., 1998, Rapid eruption of Skye lavas inferred from precise U-Pb and Ar-Ar dating of the Rum and Cuillin plutonic complexes, *Nature*, v. 394, p. 260–263.

Hole, M.J., Millett, J.M., Rogers, N.W., and Jolley, D.W., 2015, Rifting and mafic magmatism in the Hebridean basins, *Journal of the Geological Society*, v. 172, no. 2, p. 218–236.

Jaupart, C., and Mareschal, J.-C., 2007, Heat flow and thermal structure of the lithosphere, in: Schubert, G. (Ed.), *Treatise on Geophysics, Volume 6*, Elsevier Ltd. p. 217–251.

Jochum, K.P., Nohl, U., Herwig, K., Lammel, E., Stoll, B., and Hofmann, A.W., 2005, GeoReM: A new geochemical database for reference materials and isotopic standards, *Geostandards and Geoanalytical Research*, v. 29, no. 3, p. 333–338.

Jowitt, S.M., Williamson, M.-C., and Ernst, R.E., 2014, Geochemistry of the 130 to 80 Ma Canadian High Arctic large igneous province (HALIP) event and implications for Ni-Cu-PGE prospectivity, *Economic Geology*, v. 109, no. 2, p. 281–307.

Kerr, A.C., 1994, Lithospheric thinning during the evolution of continental large igneous provinces: A case study from the North Atlantic Tertiary province, *Geology*, v. 22, p. 1027–1030.

Kerr, A.C., 1995, The geochemistry of the Mull-Morvern Tertiary lava succession, NW Scotland: An assessment of mantle sources during plume-related volcanism, *Chemical Geology*, v. 122, no. 1-4, p. 43–58.

Kerr, A.C., Kempton, P.D., and Thompson, R.N., 1995, Crustal assimilation during turbulent magma ascent (ATA); new isotopic evidence from the Mull Tertiary lava succession, N. W. Scotland, *Contributions to Mineralogy and Petrology*, v. 119, no. 2-3, p. 142–154.

Kerr, A.C., Kent, R.W., Thomson, B.A., Seedhouse, J.K., and Donaldson, C.H., 1999, Geochemical evolution of the Tertiary Mull volcano, western Scotland, *Journal of Petrology*, v. 40, no. 6, p. 873–908.

Klemme, S., and O'Neill, H.S., 2000, The near-solidus transition from garnet lherzolite to spinel lherzolite, *Contributions to Mineralogy and Petrology*, v. 138, p. 237–248.

Kontak, D.J., Jensen, S.M., Dostal, J., Archibald, D.A., and Kyser, T.K., 2001, Cretaceous mafic dyke swarm, Peary Land, northernmost Greenland: Geochronology and petrology, *The Canadian Mineralogist*, v. 39, no. 4, p. 997–1020.

LeCheminant, A.N., and Heaman, L.M., 1989, Mackenzie igneous events, Canada: Middle Proterozoic hotspot magmatism associated with ocean opening, *Earth and Planetary Science Letters*, v. 96, no. 1-2, p. 38–48.

Lugmair, G.W., and Marti, K., 1978, Lunar initial $^{143}Nd/^{144}Nd$: Differential evolution of the lunar crust and mantle, *Earth and Planetary Science Letters*, v. 39, p. 349–357.

McKenzie, D., and Bickle, M.J., 1988, The volume and composition of melt generated by extension of the lithosphere, *Journal of Petrology*, v. 29, no. 3, p. 625–679.

McKenzie, D., and O'Nions, R.K., 1998, Melt production beneath oceanic islands, *Physics of the Earth and Planetary Interiors*, v. 107, p. 143–182.

McKenzie, D., and O'Nions, R.K., 1991, Partial melt distributions from inversion of rare earth element concentrations, *Journal of Petrology*, v. 32, no. 5, p. 1021–1091.

Mertzman, S.A., 2000, K-Ar results from the southern Oregon-northern California Cascade Range, *Oregon Geology*, v. 62, no. 4, p. 99–122.

Mitchell, R.H., Platt, R.G., and Garth, R., 1984, The Freemans Cove volcanic suite: field relations, petrochemistry, and tectonic setting of nephelinite–basanite volcanism associated with rifting in the Canadian Arctic Archipelago, *Canadian Journal of Earth Sciences*, v. 21, no. 4, p. 428–436.

Oakey, G.N., and Stephenson, R., 2008, Crustal structure of the Innuitian region of Arctic Canada and Greenland from gravity modelling: Implications for the Palaeogene Eurekan orogen, *Geophysical Journal International*, v. 173, no. 3, p. 1039–1063.

Okulitch, A. V., 1991, *Geology of the Canadian Arctic Archipelago, Northwest Territories and North Greenland*, Geological Survey of Canada, "A" Series Map, doi: 10.4095/213121.

Patchett, P.J., Embry, A.F., Ross, G.M., Beauchamp, B., Harrison, J.C., Mayr, U., Isachsen, C.E., Rosenberg, E.J., and Spence, G.O., 2004, Sedimentary cover of the Canadian Shield through Mesozoic time reflected by Nd isotopic and geochemical results for the Sverdrup Basin, Arctic Canada: *The Journal of Geology*, v. 112, no. 1, p. 39–57

Pearce, J.A., 1996, A user's guide to basalt discrimination diagrams, in: Wyman, D.A. (Ed.), *Trace Elements and Geochemistry of Volcanic Rocks: Applications for Massive Sulphide Exploration*, Short Course Notes 12, Geological Association of Canada, p. 79–113.

Peate, D.W., and Hawkesworth, C.J., 1996, Lithospheric to asthenospheric transition in Low-Ti flood basalts from southern Paraná, Brazil, *Chemical* Geology, v. 127, p. 1–24.

Reidel, S.P., Camp, V.E., Tolan, T.L., and Martin, B.S., 2013, The Columbia River flood basalt province: Stratigraphy, areal extent, volume, and physical volcanology, in: Reidel, S.P, Camp, V.E., Ross, M.E., Wolff, J.A., Martin, B.S., Tolan, T.L., and Wells, R.E. (Eds.), *The Columbia River Flood Basalt Province*, Geological Society of America Special Paper 497, p. 1–43.

Ricketts, B., Osadetz, K.G., and Embry, A.F., 1985, Volcanic style in the Strand Fiord Formation (Upper Cretaceous), Axel Heiberg Island, Canadian Arctic Archipelago, *Polar Research*, v. 3, p. 107–122.

Rotenberg, E., Davis, D.W., Amelin, Y., Ghosh, S., and Bergquist, B.A., 2012, Determination of the decay-constant of ^{87}Rb by laboratory accumulation of ^{87}Sr, *Geochimica et Cosmochimica Acta*, v. 85, p. 41–57.

Schaeffer, A.J., and Lebedev, S., 2014, Imaging the North American continent using waveform inversion of global and USArray data, *Earth and Planetary Science Letters*, v. 402, p. 26–41.

Schoene, B., Samperton, K.M., Eddy, M.P., Keller, G., Adatte, T., Bowring, S.A., Khadri, S.F.R., and Gertsch, B., 2015, U-Pb geochronology of the Deccan Traps and relation to the end-Cretaceous mass extinction, *Science*, v. 347, no. 6218, p. 182–184.

Tegner, C., Storey, M., Holm, P.M., Thorarinsson, S.B., Zhao, X., Lo, C.H., and Knudsen, M.F., 2011, Magmatism and Eurekan deformation in the High Arctic Large Igneous Province: ^{40}Ar-^{39}Ar age of Kap Washington Group volcanics, north Greenland, *Earth and Planetary Science Letters*, v. 303, no. 3-4, p. 203–214.

Thiede, D.S., and Vasconcelos, P.M., 2010, Paraná flood basalts: Rapid extrusion hypothesis confirmed by new ^{40}Ar/^{39}Ar results, *Geology*, v. 38, no. 8, p. 747–750.

Thompson, R.N., 1982, Magmatism of the British Tertiary Volcanic Province: *Scottish Journal of Geology*, v. 18, p. 49–107

Thorarinsson, S.B., Holm, P.M., Tappe, S., Heaman, L.M., and Tegner, C., 2011, Late Cretaceous-Palaeocene continental rifting in the High Arctic: U-Pb geochronology of the Kap Washington Group volcanic sequence, North Greenland, *Journal of the Geological Society*, v. 168, p. 1093–1106

Trettin, H.P. (Ed.), 1991, *Geology of the Innuitian Orogen and Arctic Platform of Canada and Greenland*, Geological Survey of Canada, 569 p.

Vermeesch, P., 2012, On the visualization of detrital age distributions, *Chemical Geology*, v. 312-313, p. 190–194.

Villeneuve, M., and Williamson, M.-C., 2006, ^{40}Ar-^{39}Ar dating of mafic magmatism from the Sverdrup Basin Magmatic Province, in: Scott, R.A. and Thurston, D.K. (Eds.), *ICAM IV Proceedings*, Dartmouth, Nova Scotia, p. 206–215.

Van Wagoner, N.A., Williamson, M.-C., Robinson, P.T., and Gibson, I.L., 1986, First samples of acoustic basement recovered from the Alpha Ridge, Arctic Ocean: New constraints for the origin of the ridge, *Journal of Geodynamics*, v. 6, p. 177–196.

Waterton, P.W., Pearson, D.G., Kjarsgaard, B., Hulbert, L., Locock, A., Parman, S., in prep, Origin and thermal evolution of the ultra-fresh 1.9 Ga Winnipegosis Komatiites, Manitoba, Canada

White, R.S., and McKenzie, D., 1995, Mantle plumes and flood basalts, *Journal of Geophysical Research*, v. 100, no. B9, p. 17,543–17,585.

Chapter 3

U-Pb and Ar/Ar Geochronology

3.1 Introduction

The majority of voluminous intra-plate eruptions of basaltic magma on the Earth's surface, known as Large Igneous Provinces or LIPs, are linked to plume-like mantle upwellings or "plumes" (e.g., Morgan, 1971; White and McKenzie, 1995). One indicator of plume-induced LIP magmatism is that more than 75% of the resulting basaltic magmas are produced over short-timescales (1 – 5 Myr; Bryan and Ernst, 2008) and this has been verified by high-precision geochronology studies of several LIPS (e.g., Schoene et al., 2015; Thiede and Vasconcelos, 2010). Another indicate of plume magmatism is the tell-tale 'hot spot track' they leave behind; a time-progressive series of volcanoes that travel across the hot spot by tectonic movement.

The widespread and abundant magmatic rocks that were emplaced throughout the High Arctic of Canada, Svalbard, Franz Josef Land, and Northern Greenland during the Cretaceous have been classified as a LIP – the High Arctic Large Igneous Province (HALIP, e.g., Buchan and Ernst, 2006; Ernst and Bleeker, 2010; Tegner et al., 2011; Jowitt et al., 2014; Corfu et al., 2013). Due to its inaccessibility, this igneous province is one of the least studied on Earth, with very few high-precision radiometric ages for the basaltic magmas that could be used to constrain the duration and cause of High Arctic magmatism. Previous studies have posited a mantle plume model for the formation of the HALIP based on the presence of the Alpha Ridge, interpreted as an oceanic plateau (e.g., Weber, 1990; Van Wagoner et al., 1986), which is thought to mark the location of a plume head during the Early Cretaceous initiation of the HALIP (Buchan and Ernst, 2006). Here we provide the first high-precision U-Pb ages of mafic intrusive sheets from Axel Heiberg and Ellesmere Islands. The new and published geochronological data allows us to examine the temporal and spatial relationships between the two distinct magma types present in order to evaluate the validity of the plume hypothesis for the formation of the Canadian manifestation of the HALIP. This study will contribute to our understanding of the tectono-magmatic evolution of

this area during the Cretaceous.

3.2 Geochemistry, Tectonic Framework, and Timing of Circum-Arctic Magmatism

3.2.1 Distribution of magma types

The widespread geographic extent of Cretaceous magmatism across the High Arctic regions of the Canadian Arctic Archipelago, Svalbard, Franz Josef Land, and Northern Greenland has led to its classification as a LIP (Bryan and Ernst, 2008; Buchan and Ernst, 2006; Corfu et al., 2013; Ernst and Bleeker, 2010; Estrada and Henjes-Kunst, 2013, 2004; Evenchick et al., 2015; Jowitt et al., 2014; Tegner et al., 2011). Basaltic magmatism in the Canadian High Arctic is voluminous and is focused in the Sverdrup Basin, a Carboniferous to Paleogene rift basin that spans the Queen Elizabeth Islands (Fig. 3.1). The basin is filled with up to 13 km of carbonates, clastics, and evaporates with a long axis (~1000 km) parallel to the rifted continental margin bordering the Arctic Ocean, yet the sediment is confined in the basin by the Sverdrup Rim (Fig. 3.1; Embry and Beauchamp, 2008). These volcanic successions correlate to sedimentary units of the Hauterivian to Aptian Isachsen formation, the Late Albian Hassel Formation (Strand Fjord basalts), and the Cenomanian to Campanian Kanguk and Expedition Formations for the Hansen Point Volcanic Complex (Fig. 3.2; Embry and Osadetz, 1988).

Early geochemical studies discovered the presence of two magma compositions within the Sverdrup Basin: tholeiitic and mildly alkalic basalt (Rickets, 1985; Trettin and Parrish, 1987; Williamson, 1988). The Early Cretaceous tholeiitic magmas have been linked to seafloor spreading during the second stage of opening of the Amerasian Basin (ca. 131-127 Ma; Grantz et al., 2011). The tholeiites were then superseded by a Late Cretaceous alkali basaltic magma suite that many authors argue is the continental manifestation of the Alpha Ridge, a submarine volcanic edifice off the northwestern coast of Ellesmere Island (Døssing et al., 2013; Maher, 2001; Ricketts et al., 1985; Sweeney, 1985). Both magma types outcrop as lava flows, as well as hypabyssal intrusions. Extrusive sequences are tholeiitic and most voluminous near the basin centre, on northern Axel Heiberg and northwest Ellesmere Islands, with a maximum thickness

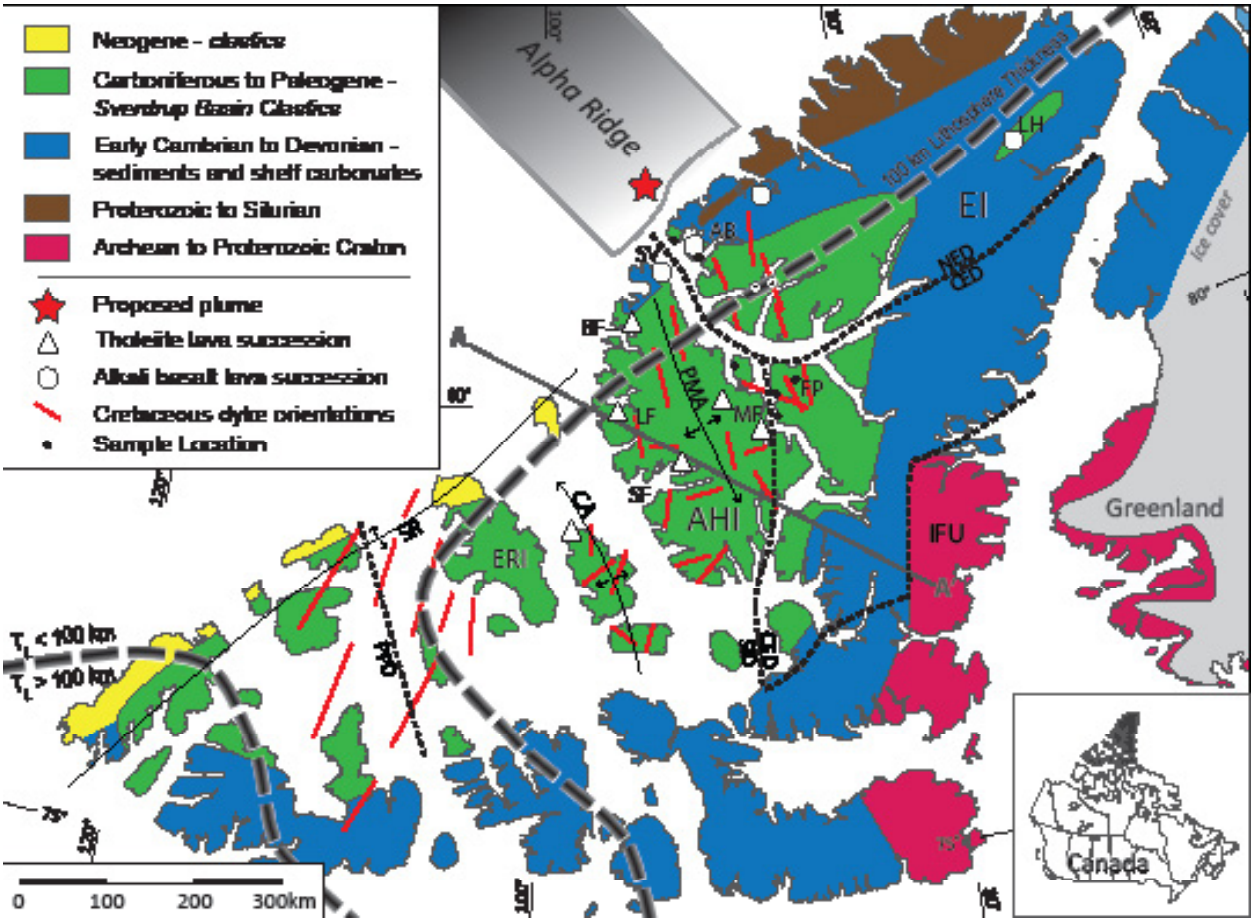

Figure 3.1 Map of the Queen Elizabeth Islands, Arctic Canada, showing: i) Regional geology (Okulitch, 1991); ii) U-Pb and Ar/Ar sampling locations (black dots); iii) dyke orientations and proposed plume location (Buchan and Ernst, 2006); iv) surface trace of the +4% S-wave seismic anomaly (dashed line; Schaeffer and Lebedev, 2014), which approximates the 100 km T_L (modern thickness of the lithosphere). iv) four tectonic domains of the Sverdrup Basin (SID – Sverdrup Islands Domain; PPD – Prince Patrick Domain; NED – Northern Ellesmere Domain, CED – Central Ellesmere Domain) and relevant structural highs (PMA – Princess Margret Arch; CA – Cornwallis Arch; SR – Sverdrup Rim) from Trettin (1991); v) A to A' schematic cross section discussed in Section 3.6.7. Geographic locations: Alpha Ridge – offshore volcanic edifice; EI – Ellesmere Island; AHI – Axel Heiberg Island; ERI – Ellef Ringnes Island; AB – Audhild Bay; BF – Bunde Fjord; FP – Fosheim Penninsula; LF – Li Fjord; LH – Lake Hazen; MF – Mokka Fjord; SF – Strand Fjord; SV – Svarteveeg Cliffs; IFU – Inglefield Uplift.

of 900 m in Strand Fjord (Ricketts et al., 1985). The extrusive thickness of the alkaline Hassel Formation is 68 m near Lake Hazen (Fig 3.2), in northeastern Ellesmere Island (Fig 3.1; Osadetz and Moore, 1988). Intrusive sheets of both magma types outcrop throughout most of the basin and have an aggregate thickness that exceeds 1500 m in the basin centre, approaching 12% of the entire basin-fill thickness (Fig. 3.1; Embry and Beauchamp, 2008). An aggregate volcanic

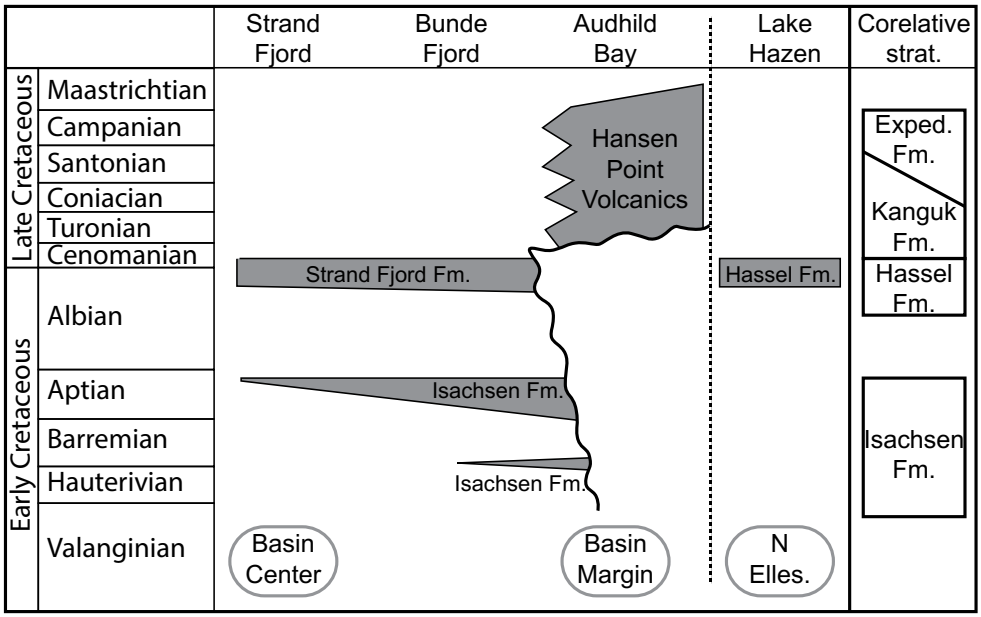

Figure 3.2 Schematic stratigraphy column of the basalt formations of the Sverdrup Basin modified from Embry and Osadetz (1988). Hassel Formation basalts are correlative to Strand Fjord Formation basalts, but outcrop mostly on northern Ellesmere Island. See Figure 3.1 for geographic locations of lava sequences.

thickness of 12 000 km^3 and an aggregate intrusive thickness of 100 000 km^3 has been estimated by Williamson (1988). Despite these pioneering early studies, the geochemical and temporal relationship between the intrusive and extrusive sequences is poorly constrained. Elucidating the relationship between these sequences is one of the aims of this study.

3.2.2 Available age constraints

Sverdrup Basin biostratigraphy constrains four main phases of volcanic activity, shown in Figure 3.2: two pulses in the Isachsen Fm. (135-130 and 127-120 Ma); Strand Fjord Fm. and stratigraphically equivalent Hassel Fm. basalts (105-90Ma); and Hansen Point Volcanics (95-70 Ma; Embry and Osadetz, 1988; Estrada, 2014). These four phases correlate to basin-wide unconformities (Embry and Beauchamp, 2008).

Previous geochronological studies of the Sverdrup Basin volcanics have mostly used the $^{40}Ar/^{39}Ar$ method, with a few K-Ar, Rb-Sr, and U-Pb ages. This study will discuss only modern (post-2000) ages, including a few U-Pb and many $^{40}Ar/^{39}Ar$ radiometric ages (summarized in Appendix C) that are accompanied by degassing data, as many K-Ar ages are likely overprinted

in this basin (e.g., Polteau et al., 2015). $^{40}Ar/^{39}Ar$ results for the extrusive basalts of the Strand and Hassel Formations and the Hansen Point Volcanics reveal two overlapping age ranges: 100-80 Ma and 84-65 Ma, respectively (Fig. 3.2; Estrada and Henjes-Kunst, 2013; Villeneuve and Williamson, 2006). Published $^{40}Ar/^{39}Ar$ ages confirm the biostratigraphic ages, but do not narrow the timeframe of the longstanding volcanic eruptions and the published ages of the Sverdrup Basin intrusive sheets span 130-70 Ma, within error.

Eight U-Pb ages have been published for the gabbroic and granitic intrusions of the Wooton Intrusive Complex, which is a NE-SW striking series of gabbroic to more evolved plutons, in northern Ellesmere Island, related to the Canadian HALIP (Estrada and Henjes-Kunst, 2013). All eight ages overlap within 92 ± 1 Ma (Trettin and Parrish, 1987; Estrada and Henjes-Kunst, 2013). At present, only two U-Pb ages have been reported for the mafic sills of the Canadian HALIP; zircon from a gabbro and baddeleyite from a dolerite sill, both from Ellef Rignes Island, which lies at the centre of the Sverdrup Basin, yielded ages of 126.7 ± 1.5 Ma and 120.7 ± 0.9 Ma, respectively (Figure 3.1; Evenchick et al., 2015).

Beyond Canada, related magmatism on the Arctic continental margin outcrops on Svalbard and Franz Josef Land, where five tholeiitic dykes were dated by the U-Pb zircon method, indicating an emplacement age of 125 – 122 Ma (Corfu et al., 2013). Younger magmatism outcrops on northern Greenland as alkali basalt dykes intruding the Peary Land metasediments, ca. 85 Ma (Kontak et al., 2001) and the intermediate to evolved volcanics of the Kap Washington Group, ca. 70 – 60 Ma (Thorarinsson et al., 2011). The tectonic reconstruction pre-Arctic Ocean Basin formation places all these islands adjacent to the Canadian Arctic Islands. This Cretaceous palaeo-geography links the contemporaneous magmatism across the circum-Arctic as part of the HALIP (Buchan and Ernst, 2006)

Recent circum-Arctic Ar/Ar and high-precision U-Pb dating of mafic magmatism has resulted in the HALIP magma pulses being narrowed down to the following two age ranges: one tholeiitic basalt phases, between 128-121 Ma, followed by an alkalic phase from 100-77 Ma (Villeneuve

and Williamson, 2006; Estrada and Henjes-Kunst, 2013; Evenchick et al., 2015). In this study, high-precision U-Pb dates and robust Ar/Ar dates for the intrusive sheets and lavas of the Canadian HALIP will be used to address: 1) the actual length and geochemical composition of the pulses; 2) the validity of the previously published Ar/Ar ages using a robust and unrelated dating method (U-Pb); 3) the temporal relationship between the two magma types and whether there is any systematic change in magma type with respect to geography; 4) finally, in conjunction with modelled 'lid' thickness results of Chapter 2, I address the question of whether the Canadian HALIP is plume-derived by consideration of the lithospheric and sub-lithospheric processes that occurred during the Cretaceous.

3.3 Samples

The study area covers a 400 km NW-SE transect between eastern Axel Heiberg and western Ellesmere Islands, centered on Nansen and Eureka Sounds between the islands (black dots in Fig. 3.1). This study area was selected to sample both the high magma volume in the basin centre, nearest to the proposed 'plume head' off the northwest coast of Ellesmere Island (Ernst and Buchan, 2001; Døssing et al., 2013), as well as the cratonward basin margin where only intrusive sheets are present.

Intrusive sheets, ranging from 0.5 to 25 m thick, were sampled close to their margins, to obtain a quenched – low fractionation – sample for geochemistry (Chapter 2), as well as in their central parts where fractionation and insulation promotes growth of extractable Zr-bearing minerals (baddeleyite or zircon) for U-Pb analysis. Following mineral separation, six samples yielded sufficient quantities of these minerals for U-Pb ID-TIMS geochronology.

A Hansen Point Volcanic lava succession was sampled at Audhild Bay (Fig. 3.1), with five distinct flows that are delineated by amygdule abundance and distribution, as well as thin paleosol development between flows. Flows ranged from 4-8 m thick. Samples for $^{40}Ar/^{39}Ar$ geochronology were selected based on low loss-on-ignition (LOI) and petrographical evidence of

minimal levels of alteration (Section 2.5). Two mafic intrusive sheets were also selected for Ar/Ar dating to extend the geographic range of the Ar/Ar samples. One sheet was dated by both Ar/Ar and U-Pb to allow for comparison of the two methods.

Sample petrography and alteration are discussed in Chapter 2 of this thesis.

3.4 Analytical Techniques

3.4.1 Geochemistry

Nine geochronology samples were analyzed for major-elements by XRF at the X-Ray Laboratory, Franklin and Marshall College, Pennsylvania, following methods outlined by Mertzman (2000). Major-element precision calculated from 10 separate fusion disks of the OKUM standard during a parallel analysis to this study (reported in Table 1; Waterton et al., *in preparation*). Precision varies by oxide with the highest being CaO (0.6% relative standard deviation) and the lowest being K_2O and P_2O_5 (3.7% and 3.5% relative standard deviation, respectively). The average relative standard deviation is 1.4% for all the major-elements. As OKUM is a komatiite, oxide concentration differences effect the precision. For example, there is 10 – 50 times less K_2O and 10 – 40 times less P_2O_5 in OKUM than the basalts of the Canadian HALIP. The higher concentrations in the basalts of this study would likely improve the analytical precision of the above two major-elements. Regardless of the chemical differences between OKUM and the Canadian HALIP basalts, the results analyzed by Waterton et al. (*in preparation*) overlap the preferred values for OKUM (Jochum et al., 2005) within 95% confidence limits and are therefore accurate.

Trace-element geochemistry was analyzed by ICP-MS at the University of Alberta in the Arctic Resources Geochemistry Facility. Geochemistry was undertaken on samples collected from the quenched margin of the intrusive body while U-Pb geochronology was undertaken on the chemically fractionated, coarse crystalline centre. Analytical uncertainty for the ICP-MS trace-elements were calculated based on nine separate BCR-2 dissolutions that were analyzed 15 times

(1σ quoted in Table 3.1). The analyzed BCR-2 results overlap with preferred values (Jochum et al., 2005) at the 95% confidence limit, using a Student's t-distribution factor (14 degrees of freedom), and are therefore deemed accurate.

3.4.2 U-Pb Geochronology

Zircon and baddeleyite were separated from six coarse crystalline gabbro samples using the methods described in Appendix D. Zircons were thermally annealed at 1000°C for 60 hours to anneal fission tracks before subjecting them to a 24% hydrofluoric acid chemical abrasion for 16 hours at 170°C to dissolve inclusions and altered zones following protocols outlined by Mattinson (2005). Both baddeleyite and the chemically abraded zircons were cleaned with acetone and 4N HNO_3 before a 72 hour dissolution at 190°C in a 5:1 solution of 48N HF and 7N HNO_3.

Each dissolved mineral fraction was dried down with 3 µL of 0.15N H_3PO_4 followed by mixing with 4 µL of silicic acid activator and loaded on an outgassed rhenium filament. The uranium and lead isotope ratios were measured on the Thermo Triton Plus Thermal Ionization Mass Spectrometer (TIMS) at the University of Alberta in the Arctic Resources Geochemistry Facility, either using multi-collection on Faraday cups equipped with 10^{12} ohm feedback resistors (Sarkar et al., 2015) or peak-hopping on an SEM (results for standards and mass fractionation corrections identical to those described in Sarkar et al., 2015). The decay constants of ^{235}U (9.8485×10^{-10} year^{-1}), ^{238}U (1.55125×10^{-10} year^{-1}) and the $^{238}U/^{235}U$ isotopic ratio (137.88) used in age calculations are from Jaffey et al. (1971). Weighted mean ages and concordia diagrams were created using ISOPLOT (Ludwig, 2008). All age uncertainties are reported as 2σ and were calculated by propagating total analytical error, but do not include the uncertainties introduced by the spike or decay constant.

A Phalaborwa baddeleyite standard (IN-1, 2059.60 ± 0.35 Ma; Heaman, 2009) was analyzed with each sample run and the results ($^{207}Pb/^{206}Pb$ weighted mean age: 2063.5 ± 6.4 Ma, n = 4) are in agreement with the accepted value, however the uncertainty of the standard is quite large. This

is potentially due to measurement of each fraction on two different TIMS insturments, which can induce variability. Also, the variation in ages may be due errors during early stages of training, as I chose large baddeleyite fragments during the first attempts, as they were easiest to handle. The large mass of these grains may not have experienced complete dissolution, which may have fractionated the isotopic ratios. Isotopic data were corrected for mass fractionation ($^{238}U/^{235}U$ = 0.024% amu^{-1}; $^{207}Pb/^{206}Pb$ = 0.095% amu^{-1}) using mass bias ratios determined from the long-term reproducibility (0.13% over 3 years) of NBS981 standard analyzed on the Triton-Plus (Sarkar et al., 2015).

The total common lead values of individual sample fractions are between 0.5 - 3 pg, with 20% of the fractions in the anomalously high 3 – 13 pg range. These high common Pb results may have originated from mineral inclusions within the zircon that were not removed during chemical abrasion. Common lead corrections are calculated following Stacey and Kramers' (1975) two step model. The total Pb loading blank during the source of this study was 0.18 pg, consistent with the long-term laboratory average. Total loading blanks, monitored over one year, have a mean value of 0.21 pg of ^{204}Pb (1σ = 0.16; n=11).

3.4.3 $^{40}Ar/^{39}Ar$ Geochronology

Three whole-rock samples and a biotite separate were analysed at Oregon State University using methods outlined in Appendix D. Reference material FCT-NM was also irradiated to monitor the conversion efficiency of ^{39}K to ^{39}Ar, the flux gradient of the reactor and all ages are calculated in relation to 28.201 ± 0.023 Ma following Kuiper et al. (2008) and Schmitz (2012). The decay constants of ^{39}Ar (2.940 ± 0.016 x 10^{-7} $hour^{-1}$), ^{40}K (0.5530 ± 0.048 x 10^{-10} $year^{-1}$), atmospheric $^{40}Ar/^{36}Ar$ of 295.50, and age equations from Min et al. (2000).

3.5 Results

3.5.1 Major-element geochemistry – whole-rock

Major-element geochemistry for the nine geochronological samples are tabulated (Table 3.1)

Table 3.1 – Major- and trace-element geochemistry

Sample		DMD124	DMD143A	DMD143D	DMD145	DMD147	DMD154	DMD160	DMD169	DMD173
TE classification		alkalic	alkali basalt	alkali basalt	tholeiitic	tholeiitic	tholeiitic	tholeiitic	tholeiitic	akalic
Sample type		sheet*	lava flow	lava flow	dyke	sheet	sheet	sheet	sheet*	sill
Latitude (°N)		79.81344	81.398632	81.399291	81.060496	81.091248	81.564941	80.344299	80.145786	80.020558
Longitude (°W)		86.41845	90.109512	90.117356	86.839593	85.759936	91.357157	88.481716	85.132571	86.383641
	1σ (rel.) ‡									
SiO_2	*0.79%*	54.6	50.7	48.2	49.5	49.3	50.2	50.7	50.8	47.2
TiO_2	*1.3%*	2.05	2.80	2.76	3.00	2.73	3.70	2.83	3.17	3.34
Al_2O_3	*0.68%*	15.4	16.9	17.1	12.5	13.6	13.8	13.3	14.1	14.6
Fe_2O_{3T}	*1.1%*	11.9	10.7	11.9	16.5	16.1	15.1	16.1	14.8	14.9
MnO	*0.71%*	0.24	0.53	0.28	0.24	0.31	0.27	0.37	0.27	0.22
MgO	*0.88%*	2.21	3.53	4.63	4.94	6.14	4.80	5.74	2.12	5.80
CaO	*0.58%*	6.1	7.8	9.0	9.4	8.7	7.4	6.2	10.7	8.1
Na_2O	*1.2%*	4.26	4.35	3.44	2.50	2.38	3.41	3.62	2.59	4.00
K_2O	*3.7%*	2.39	2.11	1.71	0.98	0.44	0.75	0.94	1.02	1.38
P_2O_5	*3.5%*	0.75	0.83	0.82	0.34	0.31	0.48	0.37	0.39	0.63
Total	*0.09%*	100.0	100.1	99.8	99.8	100.0	100.0	100.2	99.9	100.1
LOI	*8.0%*	2.07	2.02	1.94	0.04	1.69	1.85	1.26	6.78	2.15
Mg#		14	22	25	21	25	21	23	11	25
	1σ									
Ba	*16*	994	578	677	272	137	163	277	210	450
Ce	*1.6*	85.9	54.0	112.6	56.5	36.5	71.9	28.8	61.2	49.7
Co†	*1.1*	28	31	37	54	60	51	54	45	52
Cr†	*0.67*	28	14	30	52	51	50	64	28	96
Cs	*0.033*	1.29	0.25	0.33	1.44	1.52	0.49	0.60	1.17	5.98
Cu	*0.97*	7.0	19.6	23.6	190.6	118.2	44.3	37.1	199.9	18.7
Dy	*0.24*	8.6	3.5	6.0	9.2	7.1	7.9	4.9	7.9	5.4
Er	*0.13*	4.44	1.81	2.90	5.34	3.97	4.19	2.80	4.70	2.71
Eu	*0.030*	4.49	1.43	2.89	2.24	2.11	2.58	1.41	1.97	2.77
Ga	*0.81*	27.8	18.8	19.7	22.6	21.6	25.2	19.3	22.0	20.5
Gd	*0.10*	10.20	4.11	8.71	8.57	6.77	8.70	4.24	7.38	6.38
Hf	*0.18*	6.82	5.59	5.26	5.89	4.38	6.63	4.66	6.46	2.93
Ho	*0.040*	1.62	0.67	1.09	1.88	1.40	1.53	0.99	1.59	1.01
La	*1.4*	36.8	19.9	52.7	25.7	14.8	32.4	7.8	22.2	21.5
Lu	*0.022*	0.57	0.22	0.36	0.66	0.50	0.52	0.38	0.61	0.33
Mo	*12*	1.97	2.36	1.37	1.43	1.15	1.15	1.60	1.85	0.87
Nb	*0.23*	36.6	56.6	80.3	19.7	14.9	32.6	16.1	29.3	23.0
Nd	*0.54*	46.8	21.1	52.8	31.7	23.2	40.0	14.1	29.6	28.7
Ni†	*1.2*	1	8	16	37	50	21	28	28	41
Pb	*0.36*	10.18	4.73	4.40	5.86	24.55	4.89	16.40	8.20	1.99
Pr	*0.12*	11.02	4.93	13.30	6.98	4.86	9.17	2.94	6.63	6.43
Rb	*1.7*	42.8	27.1	46.2	40.7	22.8	39.7	22.7	23.1	33.3
Sc†	*1.1*	15	16	19	36	35	26	35	40	23
Sm	*0.16*	9.89	4.48	9.53	7.96	6.22	9.08	4.05	7.16	6.65
Sr	*13*	514	392	777	191	195	273	130	256	389
Ta	*0.028*	2.39	3.37	4.56	1.16	0.87	1.93	0.94	1.54	1.33
Tb	*0.04*	1.50	0.62	1.20	1.44	1.14	1.39	0.76	1.25	0.98
Th	*0.27*	5.10	2.32	5.82	3.65	1.73	5.08	1.25	3.59	2.54
U	*0.08*	1.26	1.25	1.52	0.89	0.45	1.42	0.80	1.28	0.63
V†	*13*	124	189	250	353	307	312	298	422	267
Y	*1.2*	45.0	14.8	30.9	54.7	39.3	43.4	23.5	42.2	28.3
Yb	*0.14*	3.86	1.52	2.48	4.64	3.50	3.62	2.60	4.35	2.21
Zn†	*3.6*	175	105	89	147	259	115	103	105	74
Zr	*4.8*	294	250	224	241	168	265	181	264	106
La/Sm		3.7	4.4	5.5	3.2	2.4	3.6	1.9	3.1	3.2
Gd/Yb		2.6	2.7	3.5	1.8	1.9	2.4	1.6	1.7	2.9

Major elements measured from an anhydrous powder post LOI determination, therefore the total is both anhydrous and not equal to 100

Mg# calculated on a cation basis by Mg# = 100 x Mg / (Mg +Fe^{2+}), with FeO = 0.9 x Fe_2O_{3T}

* no quenched margin sampled. More evolved geochemistry; † XRF Powder Briquette analyses, all others solution ICP-MS

‡ Major element precision calculated using 10 replicates of OKUM. Analysis done by Waterton et al. (in prep.)

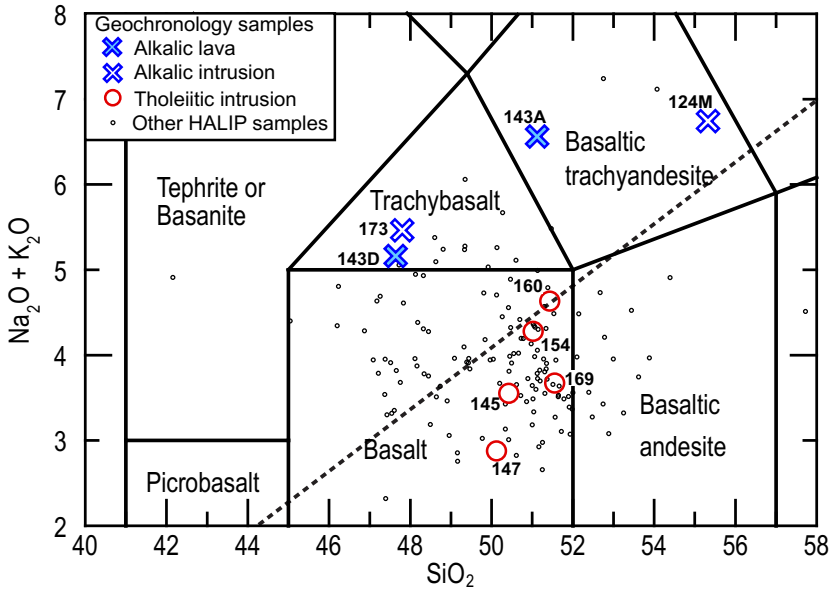

Figure 3.3 Total alkali-silica (TAS) diagram of geochronological samples from this study. LOI < 3 wt%. Alkali-tholeiite discrimination line from Macdonald (1968), though not used for classification as immobile trace-elements are used (see Chapter 2). Previously published results from Estrada and Henjes-Kunst, 2004; Estrada, 2014; Jowitt et al., 2014; Kontak et al., 2001

and plotted on a total alkali-silica plot (Fig. 3.3). Five of the nine samples plot within the basalt field (DMD145, -147, -154, -160, and -169). We were able to sample the quenched margin of the above samples, which likely reflects the magma composition upon emplacement. We therefore used these quenched samples for geochemistry and the more evolved, intrusive centre for U-Pb dating. Two samples plot in the trachybasalt field (DMD143D and DMD173) and two within the basaltic trachyandesite (DMD124 and DMD143A). DMD173 and 124 are coarse, evolved samples without a quenched margin for geochemical analysis of emplacement chemistry. DMD143A and D are lavas from Audhild Bay (Fig. 3.1) that have undergone fractionation to lower MgO concentrations, but are classified as alkalic basalts based on their immobile trace-element chemistry (Chapter 2). The TAS nomenclature of these rocks are misleading due to the effects of fractionation and magma evolution. Therefore, this study will classify the samples based on their trace-element geochemistry (Section 6.2).

Geochemistry of the samples destined for geochronology are plotted on CaO vs. MgO and Sc vs. MgO diagrams (Fig. 3.4), along with the alkalic basalts and tholeiite fields from Chapter 2. The geochronological samples are plotted with their quenched margin (when analyzed) to determine trends in fractionation (tie-lines; Fig. 3.4). These fractionation trends help constrain the alkalic and tholeiitic fields and demonstrate the inflection point for the fractionation of clinopyroxene

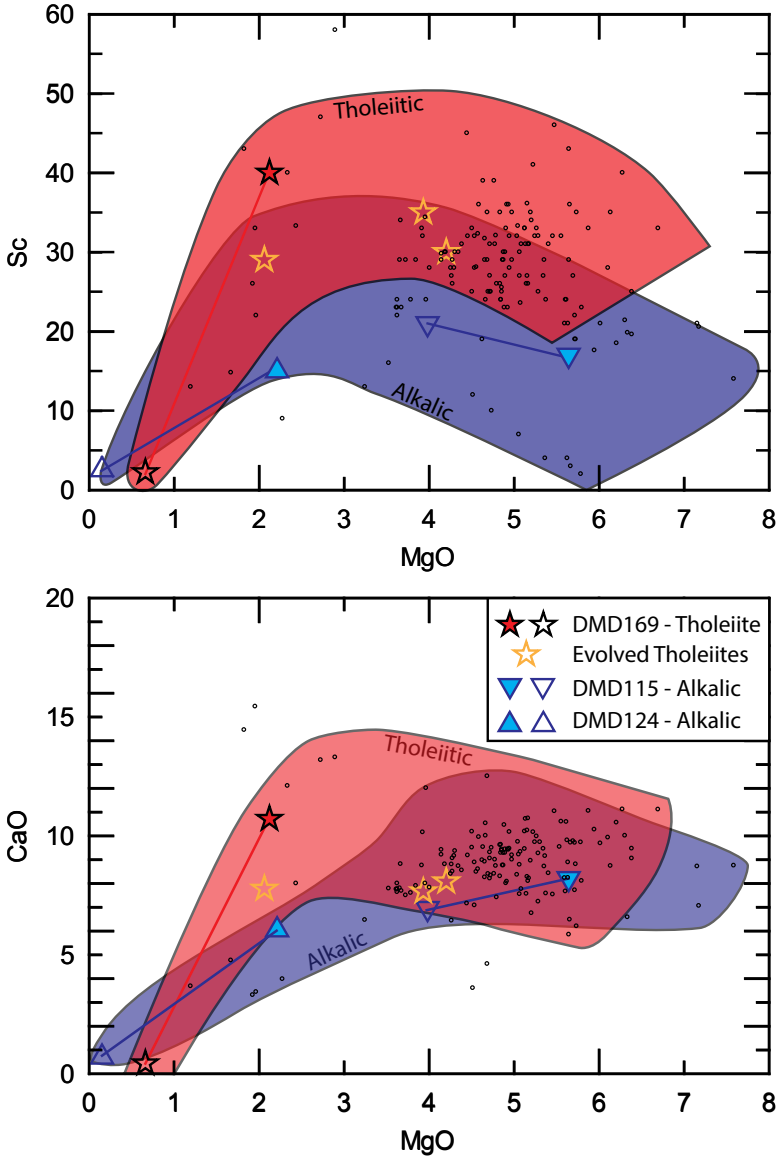

Figure 3.4 Variation of MgO with CaO and Sc. Inflection points defined by geochemical analysis of Chapter 2 as well as duplicate samples of the same intrusion: one from the quenched margin and one from the more evolved intrusion centre. These samples from the same intrusion define a magma evolution path, displayed as tie-lines. Black circles data from this study (Chapter 2), Estrada and Henjes-Kunst, 2004; Estrada, 2014; Jowitt et al., 2014; Kontak et al., 2001

in alkalic and tholeiitic basalts at 4 wt% MgO and between 2 – 3 wt% MgO, respectively (Fig. 3.4). Seven of the ten geochronology samples plot at higher MgO than the clinopyroxene inflection points, while the other three (DMD169 was dated by both methods and counts as two geochronology samples) plot below this inflection point.

3.5.2 Trace-element geochemistry

Trace-element results are tabulated (Table 3.1) and plotted on the Nb/Y versus $Zr/P_2O_5*10^4$ immobile trace-element ratio diagram (after Floyd and Winchester, 1976; Fig. 3.5a), which divides the nine samples into four alkalic basalts and five tholeiitic basalts. Classification of these

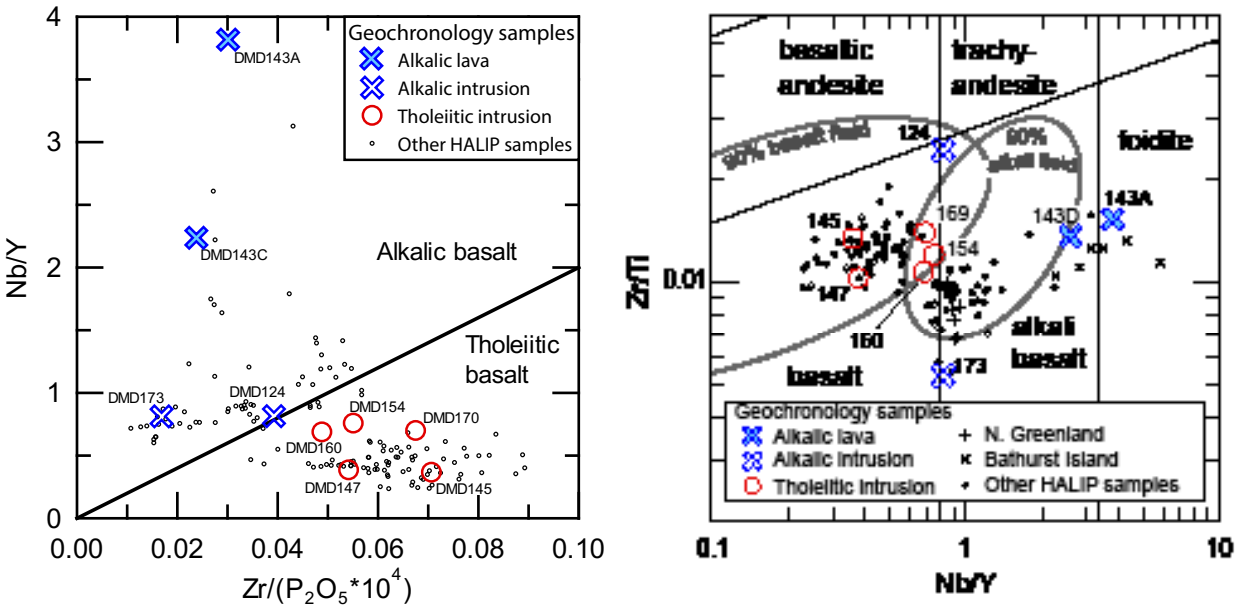

Figure 3.5 Geochronological samples classified between alkalic and tholeiitic basalt using immobile trace-element ratios (left). The classified samples are then plotted on a Zr/Ti vs. Nb/Y discrimination diagram after Pearce (1996, on the right). Previously published HALIP samples from: Estrada and Henjes-Kunst, 2013, 2004; Estrada, 2014; Evenchick et al., 2015; Jowitt et al., 2014; Kontak et al., 2001. The 90% confidence ellipses determined by Pearce (1996) to construct the discrimination lines are used to better constrain the HALIP basalts.

samples is based on the division in Figure 3.5a. All of the alkalic basalts lie outside of the 90% confidence ovals on Figure 3.5b (from Pearce, 1996; used in Chapter 2). DMD124 and -173 have variable Zr/Ti ratios. DMD124 has relatively high Zr (294 ppm) and low TiO_2 (2.1 wt%), likely due to fractionation magma evolution, since it is coarse crystalline with an MgO concentration of 2.2 wt%. However, DMD173 is a quenched margin sample with high MgO (5.8 wt%), indicating minimal fractionation, yet it has anomalously low Zr (106 ppm, outside 2σ of the mean Zr concentration in the HALIP), with normal TiO_2 values. The two lavas (DMD143A and D) are on the high Nb/Y side of the 90% alkalic basalt confidence field, but as discussed in Chapter 2, they have similar REE patterns to the nepheline normative basalts and are therefore classified as alkalic basalts that underwent fractionation at depth.

Variation of Sc with respect to MgO (Fig. 3.4) in both the alkalic and tholeiitic magma series are similar to the CaO inflection points indicative of clinopyroxene fractionation, as Sc is compatible in this phase. The Sc inflection points differ from those indicated by the CaO versus MgO plot, as

the tholeiitic inflection is between 3 – 4 wt% MgO and the alkalic inflection point is between 2 – 3 wt% MgO (Fig. 3.4)

3.5.3 U-Pb Geochronology

Twenty-six single-grain zircon and two baddeleyite fractions, containing between seven and twelve crystals each, were analyzed from six diabase intrusive sheets (Fig. 3.6; Table 3.2). All the zircon crystals are euhedral and ranged in length from 60 – 120 µm, with the notable exception of those from DMD145, which contained larger crystals (120-200 µm). Zircons from DMD145 are transparent with a brown hue, all others were colourless with alteration mineral growth along fractures that was removed during annealing and chemical abrasion following Mattinson (2005). Zircon Th/U is generally high and ranged from 0.91 – 3.43, typical for primary magmatic zircon crystallizing from basaltic magmas, with variable uranium concentrations (134 – 2572 ppm). One zircon (DMD160-2) has low Th/U (0.67) and U (67 ppm) values compared to all other fractions and has an apparent $^{206}Pb/^{238}U$ age of 184.6 ± 1.8 Ma. This age is 60 Myr older than the oldest analysed grains and is considered a xenocryst. It is not considered in any weighted mean calculations. Baddeleyite fractions consist of translucent, dark tan to beer-bottle brown, crystal fragments that are generally blade-like. They contain no visible inclusions. Baddeleyite Th/U values are indicative of a mafic parental magma (0.045 and 0.070; Heaman and LeCheminant,

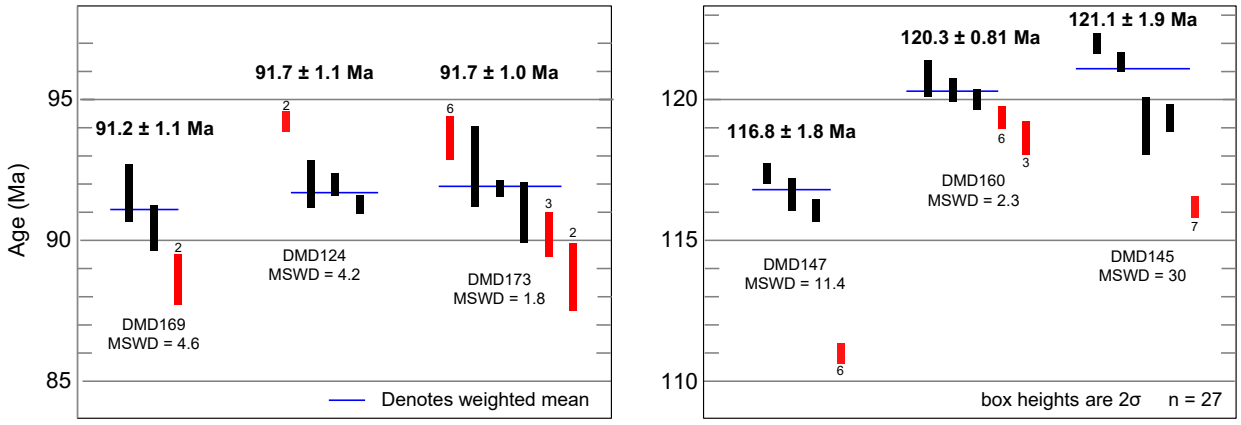

Figure 3.6 $^{206}Pb/^{236}U$ weighted mean ages for the 6 samples from this study calculated using Isoplot (Ludwig, 2008). Black fractions used for weighted mean; red fractions were omitted form the weighted mean calculation (See text for explanation). ± 2σ uncertainty given the height of the box. Xenocrystic zircon DMD160-2 (184.6 ± 1.8 Ma) is not plotted.

Table 3.2 – U-Pb fraction results (ID-TIMS)

Sample	Mineral	Weight (µg)	Concentration					Atomic Ratios (± 2σ)					Model Ages (Ma ± 2σ)	
			U (ppm)	Pb (ppm)	Th (ppm)	Th/U	TCPb (pg)	$^{206}Pb/^{204}Pb$	$^{206}Pb/^{238}U$	$^{207}Pb/^{235}U$	ρ	$^{207}Pb/^{206}Pb$	$^{206}Pb/^{238}U$	$^{207}Pb/^{235}U$
Alkali basalts														
DMD124-1	Single zircon	0.5	2061	37	2257	1.10	1.5	631	0.01427 ± 5	0.0930 ± 21	0.333	0.04729 ± 103	91.4 ± 0.3	90.3 ± 2.0
DMD124-2	Single zircon	2.0	210	6	719	3.43	1.2	340	0.01474 ± 6	0.1012 ± 49	0.449	0.04980 ± 235	94.3 ± 0.4	97.9 ± 4.6
DMD124-3	Single zircon	1.0	584	22	532	0.91	12.9	59	0.01439 ± 13	0.0938 ± 83	0.097	0.04730 ± 419	92.1 ± 0.8	91.0 ± 7.7
DMD124-4	Single zircon	1.5	351	8	324	0.92	3.5	155	0.01438 ± 6	0.0950 ± 50	0.468	0.04793 ± 244	92.1 ± 0.4	92.1 ± 4.7
DMD173-2	7 badd. frag.	1.4	132	4	9	0.070	4.1	58	0.01387 ± 19	0.0938 ± 142	0.370	0.04908 ± 721	88.8 ± 1.2	91.0 ± 13.1
DMD173-3	12 badd. frag.	1.4	322	5	14	0.045	2.7	166	0.01418 ± 13	0.0929 ± 52	0.298	0.04755 ± 257	90.3 ± 0.8	89.8 ± 3.6
DMD173-4	Single zircon	0.5	370	9	1237	3.34	0.5	364	0.01448 ± 23	0.0933 ± 201	0.668	0.04672 ± 959	92.7 ± 1.4	90.7 ± 17.2
DMD173-5	Single zircon	1.0	134	4	289	2.15	1.9	80	0.01423 ± 17	0.0923 ± 188	0.638	0.04704 ± 923	91.1 ± 1.1	89.6 ± 17.4
DMD173-6	Single zircon	1.2	269	10	636	2.37	5.5	72	0.01465 ± 12	0.1011 ± 93	0.358	0.05006 ± 448	93.7 ± 0.8	97.7 ± 8.6
DMD173-7	Single zircon	1.0	637	16	1961	3.08	0.6	1000	0.01436 ± 5	0.0950 ± 32	0.387	0.04797 ± 157	91.9 ± 0.3	92.1 ± 3.0
Tholeiitic basalts														
DMD169-2	Single zircon	0.5	230	3	341	1.48	0.6	195	0.01387 ± 14	0.0921 ± 183	0.580	0.04819 ± 933	88.7 ± 0.9	89.6 ± 12.6
DMD169-3	Single zircon	1.0	144	3	188	1.30	1.2	123	0.01434 ± 16	0.0823 ± 154	0.491	0.04165 ± 760	91.8 ± 1.0	80.3 ± 14.4
DMD169-4	Single zircon	1.0	161	4	245	1.52	1.7	101	0.01414 ± 13	0.0849 ± 134	0.507	0.04356 ± 668	90.5 ± 0.8	82.7 ± 12.5
DMD147-1	Single zircon	1.0	710	20	1354	1.91	1.9	437	0.01838 ± 6	0.1155 ± 30	0.349	0.04558 ± 113	117.4 ± 0.4	111.0 ± 2.7
DMD147-3	Single zircon	1.0	571	16	1165	2.04	1.8	374	0.01827 ± 9	0.1116 ± 81	0.726	0.04432 ± 306	116.7 ± 0.6	107.4 ± 7.4
DMD147-5	Single zircon	0.8	717	17	807	1.13	2.0	348	0.01818 ± 6	0.1212 ± 36	0.353	0.04838 ± 141	116.1 ± 0.4	116.1 ± 3.3
DMD147-6	Single zircon	0.6	1221	34	2825	2.31	1.5	555	0.01738 ± 6	0.1144 ± 29	0.355	0.04775 ± 117	111.0 ± 0.4	110.0 ± 2.7
DMD160-1	Single zircon	2.4	230	9	495	2.15	6.0	128	0.01891 ± 10	0.1285 ± 87	0.606	0.04927 ± 319	120.8 ± 0.6	122.7 ± 7.8
DMD160-2	Single xeno-zircon	1.9	67	6	45	0.67	9.0	44	0.02904 ± 56	0.2188 ± 476	0.529	0.05468 ± 1136	184.6 ± 3.5	200.9 ± 39.2
DMD160-3	Single zircon	0.8	281	9	540	1.92	2.3	134	0.01857 ± 10	0.1246 ± 93	0.455	0.04869 ± 352	118.7 ± 0.6	119.4 ± 6.6
DMD160-5	Single zircon	1.0	639	24	2021	3.16	2.9	283	0.01885 ± 7	0.1267 ± 40	0.427	0.04876 ± 148	120.4 ± 0.4	121.1 ± 3.6
DMD160-6	Single zircon	1.1	862	28	2432	2.82	1.8	622	0.01870 ± 6	0.1247 ± 22	0.322	0.04838 ± 83	119.4 ± 0.4	119.3 ± 2.0
DMD160-7	Single zircon	1.7	777	20	1382	1.78	0.9	1700	0.01880 ± 6	0.1257 ± 16	0.343	0.04851 ± 59	120.0 ± 0.4	120.2 ± 1.5
DMD145-1	Single zircon	3.6	627	22	2079	3.32	1.0	2791	0.01867 ± 8	0.1205 ± 58	0.677	0.04681 ± 211	119.4 ± 0.5	115.7 ± 5.2
DMD145-2	Single zircon	1.5	2572	84	7191	2.80	2.0	2305	0.01911 ± 6	0.1315 ± 36	0.602	0.04994 ± 128	122.0 ± 0.4	125.5 ± 3.2
DMD145-4	Single zircon	4.0	1379	36	2423	1.76	2.5	2601	0.01861 ± 16	0.1225 ± 15	0.656	0.04775 ± 44	119.1 ± 1.0	117.5 ± 1.3
DMD145-5	Single zircon	1.5	1412	43	3457	2.45	0.7	3440	0.01901 ± 5	0.1269 ± 12	0.418	0.04844 ± 43	121.4 ± 0.3	121.3 ± 1.1
DMD145-7	Single zircon	1.0	2402	61	4208	1.75	1.2	2392	0.01820 ± 6	0.1215 ± 9	0.482	0.04846 ± 33	116.2 ± 0.4	116.5 ± 0.9

Atomic ratios corrected for blank (1pg Pb; 0.5pg U), fractionation and initial common Pb (Stacey and Kramers, 1975).Weight determined with a UTM-2 ultra-microbalance; uncertainty in weight is typically 0.5 micrograms or
TCPb refers to the total amount of common lead present in the analyses in picograms. Th concentration estimated from the amount of ^{208}Pb present in the analysis and the $^{206}Pb/^{238}U$ age. Badd. frag. - baddeleyite fragmer

1993) with uranium concentrations that vary between 332 and 132 ppm.

Zircons from Cretaceous magmas have low ^{207}Pb concentrations, making accurate $^{207}Pb/^{235}U$ ages difficult to obtain and limiting the utility of the concordia diagram. The $^{206}Pb/^{238}U$ apparent ages have lower analytical uncertainties and are therefore better suited for resolving the detailed magmatic histories of young large igneous provinces. Weighted mean $^{206}Pb/^{238}U$ ages (Fig. 3.6) of the fractions outlined in Table 3.2 are divided into two age groups: three samples formed in the Early Cretaceous (Aptian) and three samples formed in the Late Cretaceous (Turonian). DMD169 is the youngest sample dated, with a weighted mean age of 91.2 ± 1.1 Ma (n = 2), however weighted mean ages should be from 3 or more fractions, so this age is less reliable than the Ar/Ar age of the same unit (see Section 2.5.4). Two samples, DMD124 and DMD173, are near identical in age at 91.7 ± 1.1 Ma (n = 3) and 91.9 ± 0.81 Ma (n = 3), respectively. The oldest two sheets in this study are DMD145 and DMD160, with weighted mean ages of 121.1 ± 1.9 Ma and 120.27 ± 0.81 Ma, respectively. DMD147 stands alone, at 116.8 ± 1.8 Ma, being outside of analytical uncertainty of the two main groups and may represent a sample from a temporally discrete magma pulse.

We filtered the individual age determinations on the basis of consistency of the elemental systematics (e.g., Th/U), evidence of Pb-loss and the nominal agreement between their $^{206}Pb/^{238}U$ and $^{207}Pb/^{235}U$ ages before calculating a weighted mean. A few single grain zircon and baddeleyite fractions that we analysed have been omitted from any further consideration of their age significance due to apparent inheritance and Pb loss (shown in red on Fig. 3.6). The omission of these fractions has a negligible effect on the absolute age of any given sample and only affects the uncertainty of the resulting age. The DMD124-2 zircon dissolution was omitted from the weighted mean age due to its high Th/U of 3.43 (where the other fractions are 0.91-1.1), the fraction shows poor agreement between its ^{206}Pb / ^{238}U and ^{207}Pb / ^{235}U ages, and it is 2.2 Ma older than the other fractions. All indicative of inheritance. DMD145-7 was the only zircon omitted due to significant Pb loss, even though there is a slight age gap between the other four fractions,

which indicates minor Pb loss (Fig 3.6). However, these four fractions have a lower intercept age of 121.0 ± 0.9 Ma, with a mean square weighted deviates (MSWD) value of 2.4, which has more statistical significance than the reported weighted mean (MSWD = 30). We therefore use fractions DMD145-1 to 4 for the age calculation because they have experienced negligible Pb loss. Two fractions analyzed from DMD160 are omitted due to Pb loss (3 and 6) along with the xenocryst DMD160-2 (not plotted). Zircon DMD147-6 was omitted due to significant amount of Pb loss, which results in a younger fraction by 5 Ma. One zircon and two baddeleyite fractions were omitted from the weighed mean age calculation for sample DMD173: single zircon DMD173-6 displays inheritance relative to the other fractions; both baddeleyite fractions, DMD173-2 and -3, are younger than zircon fractions.

3.5.4 $^{40}Ar/^{39}Ar$ Geochronology

Plateau ages for three whole-rock and one single phase (biotite) $^{40}Ar/^{39}Ar$ analyses are presented in Figure 3.7 (Table 3.3). We use a reliability index for the resulting ages, from 1 (most reliable) to 3 (least reliable, indicative only), based on the following criteria: percent of gas released over the plateau being greater than 50%, probability of fit greater than 0.05, good agreement between plateau and inverse isochron ages, as well as the similarity of calculated initial $^{40}Ar/^{36}Ar$ with the atmospheric value of 295.5 (Baksi, 2006). Ages are reported along with 95% analytical errors only.

The single phase biotite sample, DMD169 (Aptian plateau age: 91.7 ± 0.1 Ma), is the most reliable rank (1.5/3) as the plateau consists of 61% of the total gas released, with an initial $^{40}Ar/^{36}Ar$ of 293.3 ± 7.7 being defined by the inverse isochron, and within-error agreement between the plateau and inverse isochron age. The reason we do not assign a rank of 1 is due to the relatively low probability of fit of the plateau age (0.046) and the inverse isochron (0.039), which are marginally below 0.05. Biotite-bearing “pegmatite” sample DMD169 was collected from a late stage, leucocratic lens within a 30+ m thick mafic sill and contains both zircon and biotite, allowing for an age determination by both methods. The results agree within error, with

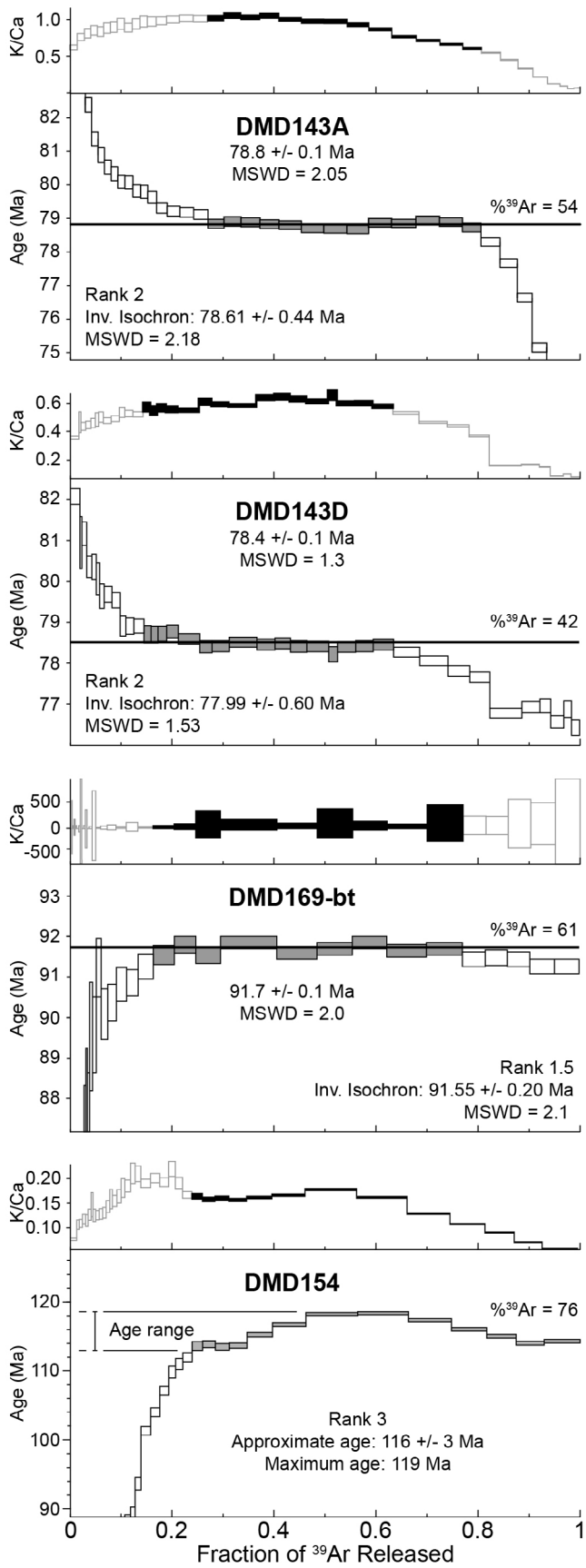

Figure 3.7 $^{40}Ar/^{39}Ar$ step heating spectrum ages for the 4 samples from this study. Plateau steps used for age calculations shaded in grey. K/Ca ratios steps are shown for each sample and plateau steps are shaded black. Reliability rank out of three quoted for each sample. Plateau ages and Inverse isochron ages quoted with 2σ analytical error. Note the high precision of each individual gas measurement.

the Ar/Ar age (91.7 ± 0.1 Ma) slightly older than the zircon crystallization age (91.2 ± 1.1 Ma) and ages agree within analytical error. Since the Ar/Ar age is more precise, we regard it as the emplacement age of DMD169.

The reliability rank 2 samples are the alkali basalt flows DMD143A (plateau age: 78.8 ± 0.1 Ma) and DMD143D (plateau age: 78.4 ± 0.1 Ma), from the same sequence of flows. The slight, yet significant, difference between the lava ages is consistent with their stratigraphic order in that DMD143A is below DMD143D in the succession. Both their plateau and inverse isochron ages are Campanian and agree within error. For sample DMD143A we assign a lower reliability rank of 2 because of the low probability of fits of both the plateau and inverse isochron. DMD143D has much better probability of fits for these two

Table 3.3 – Step heating Ar/Ar results

Sample	Magma Type		Rank	Material	Temp. Steps Plateau / Total	Ca/K	Ca/K average	Total gas age Ma ± 2σ	Plateau Age Calculation				Inverse Isochron Calculation			
									Age Ma ± 2σ	% ^{39}Ar released	MSWD	Prob. of Fit	Age Ma ± 2σ	MSWD	Atm ^{40}Ar/^{36}Ar ± 2σ	Prob. of Fit
DMD143A	alkalic	Lava	2/3	whole rock	13 / 38	0.068 - 4.80	0.781	78.66 ± 1.76	**78.8 ± 0.1**	54	2.05	0.017	78.6 ± 0.44	2.18	370 ± 176	0.013
DMD143D	alkalic	Lava	2/3	whole rock	12 / 38	0.083 - 0.653	0.589	78.29 ± 1.75	**78.4 ± 0.1**	42	1.30	0.22	78.0 ± 0.60	1.53	630 ± 390	0.31
DMD169	tholeiitic	Sill	1.5/3	biotite	9 / 41	0.8 - 103.1	17.2	90.83 ± 2.03	**91.7 ± 0.1**	61	2.0	0.046	91.6 ± 0.20	2.1	293.3 ± 7.7	0.039
DMD154	tholeiitic	Dyke	3/3	whole rock	13 / 38	0.057 - 0.220	0.086	109.30 ± 2.44	~~**116.2 ± 1.0** *~~	76	> 100	0	119.9 ± 2.0	67.87	164.93 ± 54.4	0

All errors reported with analitical uncertainty only

* Result unreliable: a resonable inferred age (116 ± 3 Ma) is extracted from the step heating spectrum plot (see text and Fig. 3.7)

parameters (0.22 and 0.31), yet it has large errors on the calculated initial $^{40}Ar/^{36}Ar$ and the gas released over the plateau is only 42%, lowering its reliability to 2 of 3.

We assign the reliability of the $^{40}Ar/^{39}Ar$ age of sample DMD154 as rank 3 because it has a very disturbed gas release pattern, with no distinct plateau over any significant fraction of gas released. The broad "hump" in gas release indicates a maximum age of 119 Ma and 20% of the ^{39}Ar released sits at around 113 Ma. The inverse isochron age (119.9 ± 2.0 Ma) is unreliable, with a large analytical error and a high MSWD (68). The inverse isochron age only broadly agrees, within error, of the maximum age determined from the age spectrum. We therefore discuss this sample as an approximate age of 116 ± 3 Ma. Whereas the uncertainty is probably an underestimate, we note that this "indicative" age overlaps, within error, the much more precise U-Pb zircon age determination for another dyke sample, DMD147 of 116.8 ± 1.8 Ma, which we take to be the crystallisation age. These dykes, 100 km apart, may represent an additional pulse of magma, close in age, but (in the case of DMD147) distinct from, the ca. 122 Ma HALIP magma pulse.

3.6 Discussion

3.6.1 Initiation and duration of mafic magmatism

The 184.6 ± 1.8 Ma age from xenocrystic zircon DMD160-2 is 60 Ma older than all published Mesozoic ages and is the first radiometric age evidence of Jurassic magmatism in the Sverdrup Basin. It was crystallized from a mafic magma as evidenced by its relatively high Th/U value. It could represent the first phase of rifting of the Amerasian Basin, which occurred between 195 – 160 Ma (Embry and Beauchamp, 2008; Grantz et al., 2011).

The oldest volcanic activity in the Sverdrup Basin is constrained by biostratigraphy. The Isachsen Fm. basalts outcrop near Bunde Fjord (20 m thick; Fig. 3.2. for stratigraphy) and the Geodedic Hills (10 m thick; Fig. 3.1 for locations) and were emplaced between 135 - 128 Ma (Embry and Osadetz, 1988). There are no radiometric ages that confirm the oldest lavas of

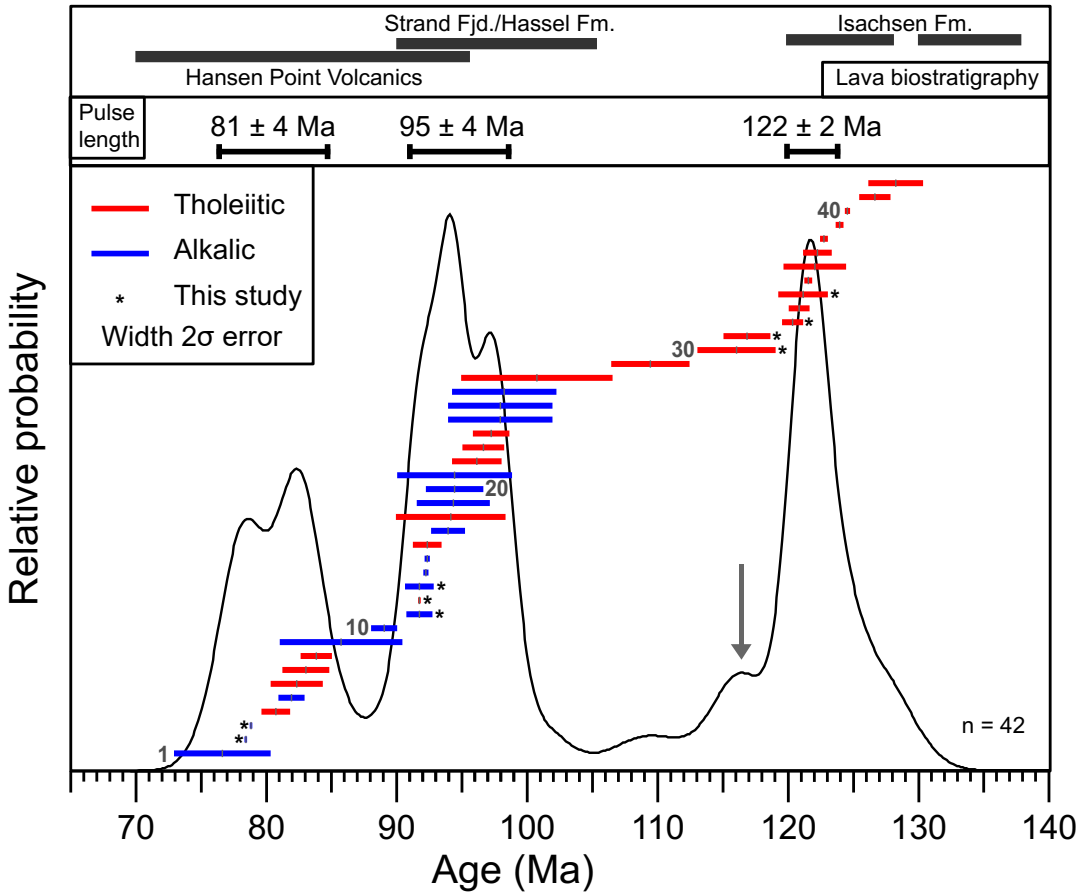

Figure 3.8 Age summary and kernel density estimation curve of this study (marked by *) and published Cretaceous mafic magmatism from: Corfu et al., 2013; Estrada, 2015; Estrada and Henjes-Kunst, 2013; Jokat et al., 2013; Kontak et al., 2001; Thorarinsson et al., 2011; Villeneuve and Williamson, 2006. See Appendix C for a compilation age summary and sample ID#. All ages quoted are from publications using Tholeiitic (red) and alkalic composition (blue) from this study. Grey arrow points to the two ~117 Ma ages reported in this study. 2σ errors reported as width of box. Kernel Density Estimation (after Vermeesch, 2012) bandwidth set to 1.5 to equally weight the uncertainty of each reported age. Biostratigraphy of extrusive formations from, Tegner et al. (2011) and references therein, demonstrate the overlap of the extrusive units with magmatism peaks. However, the dates (n=41) better demonstrate the pulsing nature of the mafic magmatism. Pulse length calculated by full width at half maximum.

the Isachsen Fm basalts or any basalt older than 130 Ma. The oldest radiometric ages in the northern Sverdrup Basin are from the Lightfoot River tholeiitic dyke swarm at 128.2 ± 2.1 Ma ($^{40}Ar/^{39}Ar$ wholerock; Villeneuve and Williamson, 2006) and at 126.7 ± 1.5 Ma in the southern Sverdrup (U-Pb zircon/baddeleyite; Evenchick et al., 2015) within the rift basins associated with tholeiitic eruptions Sverdrup Islands Domain (SID, Chapter 2). This first pulse of exposed mafic magmatism has been attributed to the second opening phase of the Amerasian Basin (Embry and Beauchamp, 2008; Grantz et al., 2011). Significantly, there is evidence for coeval MORB eruption at the Arctic spreading centre between 131 – 127.5 Ma (Grantz et al., 2011),

synchronous with the first pulse of tholeiitic mafic magmatism in the Sverdrup Basin.

Voluminous basaltic magmatism in the Sverdrup Basin continued intermittently over a period of at least 50 Myr from its initiation at ~130 Ma, punctuated by two quiescent periods, creating three temporally distinct pulses: 124 – 120 Ma, 99 – 91 Ma, and 85 – 77 Ma (Fig. 3.8; calculated by full width at half maximum of peak; ages compiled in Table 3.4), which corresponds to basin-wide unconformities related to thermal uplift (Embry and Beauchamp, 2008). As two ages obtained in this study are coincident at ~ 117 Ma, we tentatively suggest this as evidence for a fourth pulse of basaltic magmatism in the Sverdrup Basin, but more ages are needed to confirm this hypothesis. No other precise radiometric ages lie within these gaps in the Canadian Arctic, although a mafic dyke in northern Greenland has been reported at 109.4 ± 3 Ma (Estrada and Henjes-Kunst, 2013). Mafic magmatism in the Canadian Arctic Islands ceased at 76.6 ± 3.7 Ma ($^{40}Ar/^{39}Ar$ age: Estrada and Henjes-Kunst, 2013), which overlaps within error to our youngest reported age from the Hansen Point Volcanic complex (HPVC) of Audhild Bay (Fig. 3.2). More evolved trachybasalts to rhyolites continued in the northern Greenland Kap Washington Group between 71 and 61 Ma, for a total duration of almost 70 Myr of magmatism on the North American Arctic continental margin.

In geochronological assessments of high volume large igneous provinces (LIP), earlier studies (pre-2000) tend to overestimate the duration of magmatism (e.g., Parana; Deccan; Siberian LIPs – outlined in Renne and Basu, 1991; Hamilton et al., 1998; Thiede and Vasconcelos, 2010). Yet, with modern refined analytical techniques, plume-derived LIPs are found to have erupted the majority of their basaltic magma in 1 – 3 Myr (Schoene et al., 2015), with significantly reduced volcanic activity that can persist for up to 10 Ma after the major eruptive event. This is not the case for the Cretaceous magmas of the HALIP. Robust U-Pb dating from this study combined with the two U-Pb ages reported by Evenchick et al. (2015) show that: i) the overall duration of mafic magmatism across the Canadian HALIP is much more prolonged than other LIPS – at least 50 Myr; and ii) The overall span of mafic magmatism is segmented into at least three

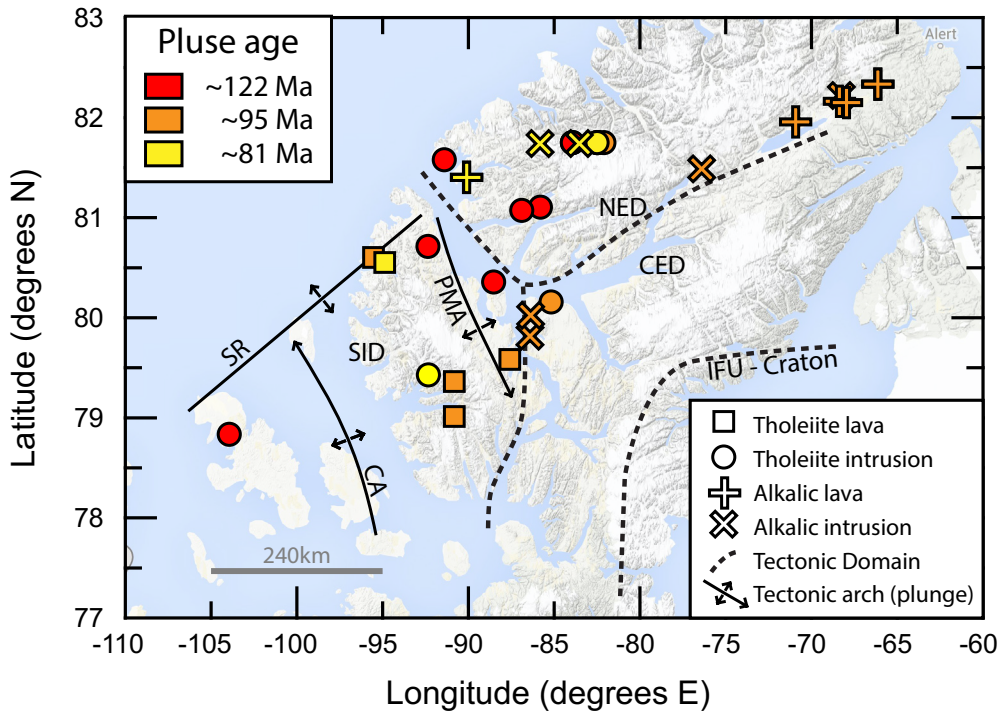

Figure 3.9 Geographic distribution of all published samples of the Canadian HALIP with tectonic domains and highs also in Fig. 2.14 (Chapter 2) modified from Trettin (1991). There is no systematic trend in emplacement age with respect to geography or the tectonic domains of the Sverdrup Basin. Terrain map from Google Maps (2016)

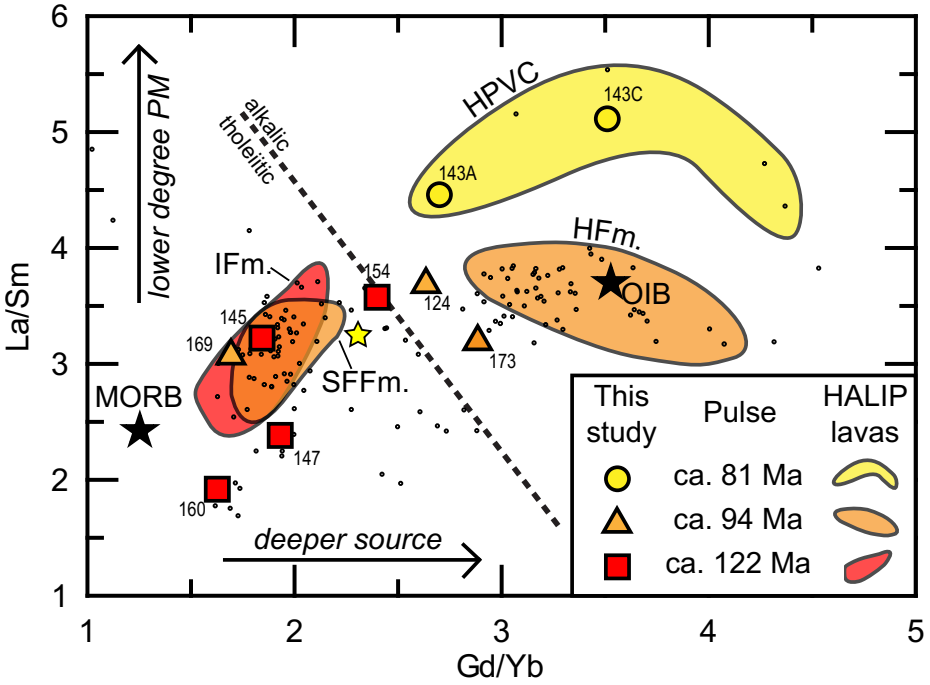

Figure 3.10 La/Sm vs Gd/Yb plot demonstrating contemporaneous alkalic and tholeiitic eruptions of the ~95 and 81 Ma pulses, as well as the exclusive tholeiitic emplacement of the ~122 Ma pulse. Yellow star is a tholeiitic basalt of the 3rd pulse (BND83-016: age 83.8 ± 1.2; Villeneuve and Williamson, 2006). Ages from this study; Estrada and Henjes-Kunst, 2013; Kontak et al., 2001; Estrada, 2015; Villeneuve and Williamson, 2006. See stratigraphic column (Figure 3.2)

distinct pulses, each 10 – 12 Myr in duration (Fig. 3.8) This range is much longer than the LIP classification of the 1 – 5 Myr outlined by Bryan and Ernst (2008). Gaps between the pulses are 21 and 6 Myr, during which time minimal magma is emplaced. Geochemical and temporal differences are evident that limit the classification of these pluses as one single LIP and demand an alternative, more complex model for the generation of this sequence of voluminous mafic magma production.

3.6.2 Temporal, compositional, and geographic distribution of Sverdrup mafic magmatism

Intrusive sheets occur throughout the entire Sverdrup Basin and vary in age from 128 to 76 Ma. Two critical points are that: i) there is no correlation between the geographic distribution of sheets and their emplacement ages (Fig. 3.9); and ii) there is no clear relationship between magma-type (alkalic versus tholeiitic) generation with time (Fig. 3.10). Intrusive sheets have little geographic relevance, as magma intruding into continental lithosphere has been shown to travel up to 260 km from its source (Reidel et al., 2013). On the other hand, lavas have geographic relevance since they can be correlated using stratigraphy and are likely to travel significantly shorter distances from their source. The occurrence of lavas of both alkali and tholeiitic character on Axel Heiberg Island and northern Ellesmere Island (Locations on Fig. 3.1 requires variable lithospheric thicknesses to be present in the Canadian HALIP, as melting of metasomatized lithosphere is unlikely from geochemical considerations (outlined in Section 2.7.2)

All ca. 122 Ma basalts and intrusive sheets investigated in this study are tholeiitic, as are those from central Sverdrup Basin (Evenchick et al., 2015), Franz Josef Land, and Svalbard (Bailey and Rasmussen, 1997; Corfu et al., 2013). There are no reported basalts belonging to the alkali differentiation series on the circum-Arctic islands, except for in the Sverdrup Basin and on northern Greenland. This implies that the rift-related tholeiites of the 122 Ma pulse are the only geochemical link between the islands and that there is no further association post-rift. Our documentation of a reliable U-Pb zircon age of 116.8 ± 1.8 Ma for a tholeiitic sheet from west-

central Ellesmere Island (Emma Fjord, Fig. 3.1) is the youngest of this tholeiitic series to be dated, whose age overlaps with the inferred Ar/Ar age from a tholeitic dyke north of Audhild Bay (Fig 3.1). These two results represent either part of the tail of the ~122 Ma pulse, or a pulse of its own. Further age constraint is needed to comment further.

The ca. 95 and 81 Ma pulses of HALIP mafic magmatism outcrop only in the Canadian Artic Islands and on northern Greenland. They are more geochemically and geographically complex than the ca. 122 Ma pulse of magma erupted across the circum-Arctic. The basaltic magmas produced within these later pulses are both tholeiitic and alkali, with a wide range of normalized REE ratios (Fig. 3.10; Gd/Yb between 1.5 to 4.3). The alkalic basalts of the Hassel Formation in northern Ellesmere Island (Lake Hazen, Fig. 3.1) have been dated to between 94 – 98 Ma (Estrada, 2015), yet, the intrusive sheets DMD124 and DMD173 (91.7 ± 1.1 and 91.7 ± 1.0) of this study are the oldest reported radiometric ages of alkali basaltic magmatism in the central Sverdrup Basin by more than 10 Myr. This confirms the temporal overlap between the alkalic magmas (92 – 76 Ma) and tholeiites (100 – 81 Ma) of the 2nd and 3rd magma pulses across the Canadian HALIP.

The latest known tholeiitic basalt sequence erupted as a flow on west Axel Heiberg Island, forming part of the Strand Fjord Fm., at 81 Ma (Villeneuve and Williamson, 2006). All younger magmatism has strong alkali, OIB-like signatures.

3.6.3 Mapping lithospheric thickness variations through time using magma geochemistry

Lithospheric thickness is a primary control on isentropic upwelling and melting of the mantle (e.g., Mckenzie & Bickle, 1988). The temporal variation in the thickness of the lithospheric lid is a potential test of whether the melting regime that produced the HALIP magmas is consistent with a simple plume model, or requires a more complex tectonic genetic model. In plume-derived LIPs, the plume impinges on the base of thick, often stable, continental lithosphere. When adiabatic upwelling mantle encounters this lithospheric barrier, decompression melting leads to relatively low volume melting and the first basalts erupted are of alkalic affinity.

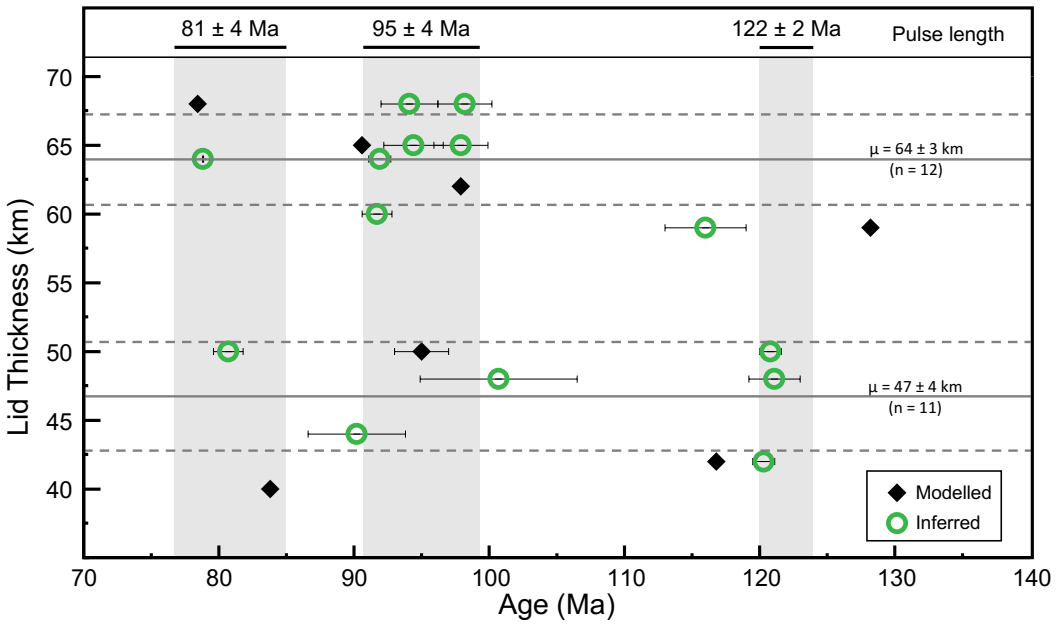

Figure 3.11 Distribution of lithospheric 'lid' thickness versus age, with thickness averages and pulse lengths calculated by this study shaded in grey. There is notable absence of lithospheric thickness values between about 50 and 58 km.

With time, a plume erodes the thermal boundary layer, thinning the lithosphere and leading to high volume tholeiitic magma production (Kerr, 1994; Hamilton et al., 1998), resulting in an progression from alkalic eruptions to tholeiitic eruptions. The results from the Canadian HALIP indicate the opposite is occurring, with the first magma pulse producing exclusively tholeiitic basalts, generated beneath thin lithosphere (42 - 58 km; Fig. 3.11).

Analysis of estimates of lid thickness (obtained from REE inversion, Chapter 2) over the 50 Myr duration of Canadian HALIP mafic magmatism reveals that there is no correlation between the age of emplacement of the lavas or intrusions and lithospheric thickness (Fig. 3.11). For instance, in both the 81 Ma and 95 Ma pulses, lid thickness ranges widely, from 40 to 68 km, with no systematic trend. The generation of the 122 Ma pulse took place in lithosphere that was thinner overall (40 to 58 km). The two alkali basalt flows of Audhild Bay (Fig. 3.1; DMD143A and –D: 78.8 ± 0.1 and 78.4 ± 0.1 Ma), were erupted on-shore, less than 200 km south of the Alpha Ridge (Fig. 3.1). This oceanic crustal structure has a crustal thickness of > 30 km (Verzhbitskii et al., 2013) and would be accompanied by a thick lithospheric root. Generation of the most recent magma beneath the Alpha Ridge should produce alkalic basalts, which has been

confirmed by sampling (Van Wagoner et al., 1986). The REE inversion modelling (Chapter 2) results in an inferred lithospheric thickness of these 68 km for these lavas, which we interpret as the maximum lithospheric thickness for the Alpha Ridge at 80 Ma. These striking differences in the thickness of the lithosphere around the Canadian HALIP, at different points in time, appear to dominate the nature of the magma chemistry but document a complex picture. The absence of any temporal trend in lid thickness, both within individual magma pulses, and over the entire duration of the HALIP magmatism, is inconsistent with that documented for magmatism produced in other LIPs and requires a more complex model than simple plume impingement and associated lithospheric rifting to explain the temporal complexity.

3.6.4 An alternative tectonomagmatic model for the Sverdrup Basin basaltic magmatism

A working tectonomagmatic model for the Canadian HALIP must be capable of generating coeval alkali and tholeiitic basaltic magmatism in pulses across the Sverdrup Basin. One mechanism to explain the observed complexity in geochemical and chronological relationships could be localized lithospheric thickness variations caused by the juxtaposition of thick, cratonic lithosphere beside the thin, rifted lithosphere of the Sverdrup Basin. This is an optimal situation for magma production via the alternating effects of the two types of edge-driven convection (EDC): EDC *sensu stricto* (s.s.) and EDC with shear

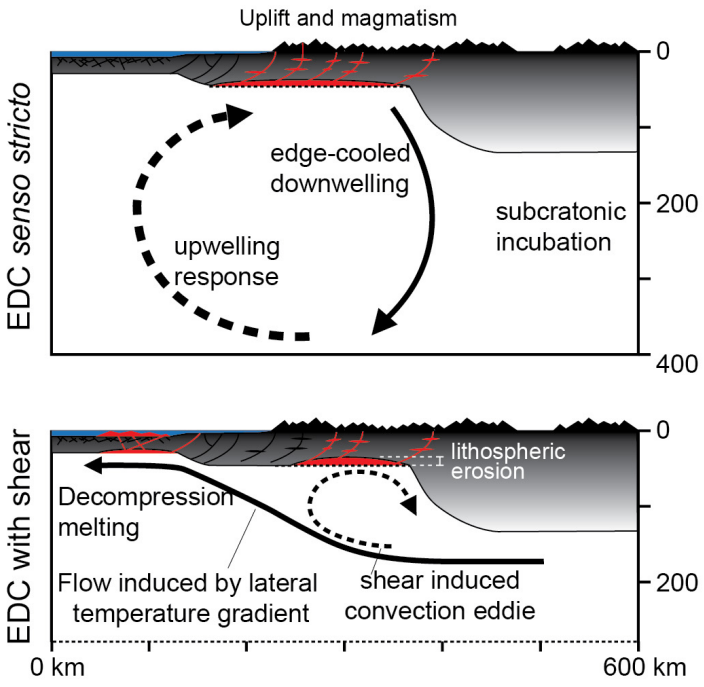

Figure 3.12 Cartoon representation of the two modes of Edge-driven convection (EDC) modified from Kaislaniemi and van Hunen (2014): a) EDC senso stricto: at the craton edge, mantle cools and downwells, creating short wavelength convection cells. b) EDC with shear: a horizontal temperature gradient induces a long wavelength convection cell that produces secondary eddies, eroding the thermal boundary layer (TBL). See text.

(w.s.), as described by Kaislaniemi and van Hunen (2014) and is illustrated schematically in Figure 3.12.

The Sverdrup Basin was deposited on the margin of to the very large cratonic amalgamation of North America. Lithospheric thickness on Somerset Island, 350 km south of the Sverdrup Basin, had ~170 km thick lithosphere at 90 Ma, based on mantle xenoliths (Mather et al., 2011). The eruption of MORB in the newly formed Amerasian Basin to the north would be very thin lithosphere. This steep lithospheric gradient from cratonic to thin oceanic lithosphere is more than a 120 km difference in lithospheric thickness over 800 km map distance. Such a lithospheric architecture makes the Canadian HALIP a candidate for the alternating effects of EDC *s.s.* and EDC w.s.. At the craton edge, old, cold lithosphere, cools the adjacent mantle, inducing downwelling EDC s.s.. At the same time, the subcratonic mantle is thermally insulated by overlying thick lithosphere such that it may have warmer than normal mantle potential temperature (Jaupart and Mareschal, 2007; Heron and Lowman, 2014). The excess mantle potential temperature will generate a horizontal thermal gradient (0.1 to 1% T_p difference), which, in turn, induces lateral mantle movement, shearing the EDC s.s. downwelling mantle. The movement of subcratonic mantle up the basal-lithospheric gradient toward thinner lithosphere creates a long wavelength convection cell, with secondary convection cells (eddies) on the lee side of the craton edge (Fig. 3.12, EDC w.s.; Kaislaniemi and van Hunen (2014). Coupled with decompression melting and erosion of the thermal boundary layer, these eddies create a peak-and-pit topography at the base of the lithosphere abutting the craton. This small-scale gradient in lithospheric thickness can have a profound influence on the chemistry of the magmas generated and on their geographic distribution, as lithospheric erosion can progress to ~40 km (Kaislaniemi and van Hunen, 2014), which is significant enough to account for the different magma types generated in the Sverdrup Basin.

3.6.5 EDC control on magma composition and volume

Variability in the composition of the erupted magmas can be explained by alternating modes of

EDC operating during the Cretaceous, with upwelling mantle travelling northwest, towards the basin centre. Rising mantle beneath Greenland would have traveled toward the Arctic Ocean basin, inducing mantle eddies and melting beneath northwestern Sverdrup basin, where the continental lithosphere is the thinnest. This magma then injects vertically into the Sverdrup Basin, likely utilizing extensional fault planes created during rifting (See Chapter 2, Section 2.7.4). At reasonable mantle potential temperatures (1300 – 1400°C), EDC w.s. (Fig. 3.12) can produce between 5 – 20 m of magma (vertical thickness) per million years. Over the 50 Myr duration of the Canadian HALIP, this amounts to an aggregate thickness of about 1000 m of magma. This is comparable to the 900 m of extrusive successions in the Strand Fjord Formation measured by Ricketts et al. (1985). However, this does not account for the additional ~1500 m of aggregate sill thickness estimated to have accumulated in the basin centre (Trettin, 1991). The additional magma generation is likely due to an increase in scale from the parameters used by Kaislaniemi and van Hunen (2014). Their model input for craton width was 2000 km and they posit that larger cratons would likely strengthen the effect of EDC w.s. by increasing the horizontal temperature difference. As the North American (plus Greenland) craton dimensions are on the order of approximately 4000 by 3500 km, it is likely that this larger area increases the volume of magma the EDC system is able to produce.

3.6.6 EDC control on eruption timing and pulses

The timing of the Canadian HALIP magmatism can be explained by the alternating modes of edge-driven convection. Sub-lithospheric eddies create heterogeneous thinning of up to ~ 40 km (Kaislaniemi and van Hunen, 2014). The spatial variability of this thinning is sufficient to generate contemporaneous tholeiitic and alkalic magma. Moreover, detailed modeling indicates that when alternate EDC modes operate, magma erupts in pulses of 12 – 20 Myr duration, separated by 14 – 26 Ma periods of quiescence (Kaislaniemi and van Hunen, 2014). This pulsing mimics the periodicity observed in the Canadian manifestation of the HALIP (Fig 3.8).

The alternating modes of EDC might have begun in the Canadian HALIP as rifting in the

Sverdrup Basin waned after the ca. 122 Ma magma pulse that thinned the lithosphere sufficiently to produce tholeiites. At this point, heat lost to conduction and the cooling effect of the craton would have lowered the temperature of the sub-Sverdrup mantle, inducing the craton edge downwelling mode of EDC *s.s.* and marking the start of the first quiescent period between 120 - 99 Ma. Sometime prior to the ca. 95 Ma pulse, EDC w.s. (Fig. 3.12) could have become dominant, as lithospheric thinning predates the peak of magmatism (Kaislaniemi and van Hunen, 2014). There is a minor gap of about 6 Myr with minimal magma eruption between the ~95 and the ~ 81 Ma pulses (Fig. 3.8), indicating that the switch between EDC styles between the pulses was shorter than the model predicts (15 – 25 Myr gaps; Kaislaniemi and van Hunen, 2014). In the numerical models, there is a negative correlation between mantle convection speed and gap length, whereby the faster the EDC w.s. mantle is travelling, the shorter the gaps between pulses. As mantle velocity depends on the lateral temperature gradient (Kaislaniemi and van Hunen, 2014), the increased scale of the North American craton likely increases the lateral temperature gradient which would decrease the gaps between pulses.

3.6.7 EDC control on geography of magma emplacement

As discussed in Chapter 2, there are rift-controlled locations of thin lithosphere present in the Sverdrup Basin. These pre-established zones of thin lithosphere may have been exploited by EDC, providing “nucleation sites” for the development of eddies that further erode the lithosphere. In the geodynamic models, these eddies are 200 km wide (Kaislaniemi and van Hunen, 2014), which is the same width as the Sverdrup Basin depocenter beneath Axel Heiberg and Ellef Ringnes Islands (Oakey and Stephenson, 2008). It is possible that repeated thermal boundary layer erosion by EDC w.s. eddies, followed by thermal subsidence between pulses, would have controlled the dimensions of the depocenter. It is 200 km wide with a long axis parallel to the craton’s edge (Fig. 3.1).

Hot mantle shed off the base of continental North America and Greenland would create sub-lithospheric eddies that decrease the lithospheric thickness by up to 40 km (Kaislaniemi and van

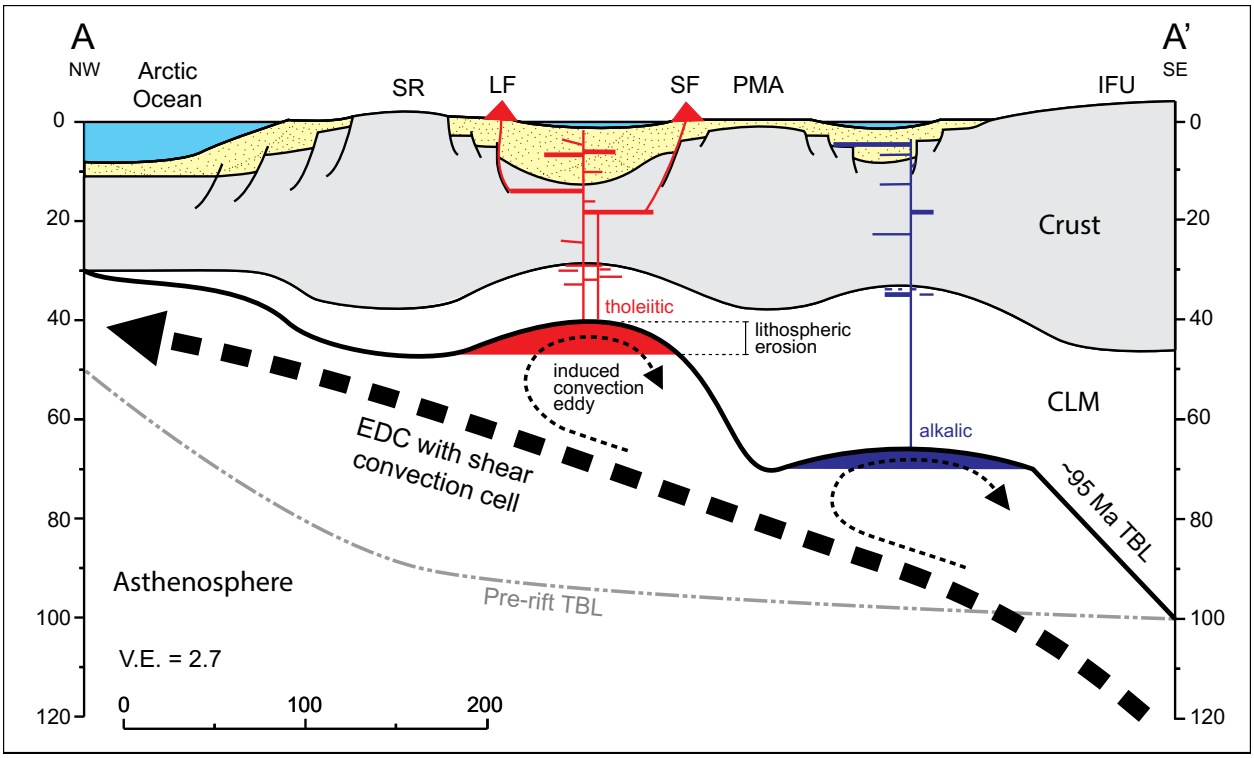

Figure 3.13 Schematic lithospheric cross section of the ca. 95 Ma Sverdrup Basin with inferred effect of EDC on the continental lithospheric mantle (CLM). EDC heterogeneously erodes the thermal boundary layer (TBL) and utilizes the tectonically weakened crust for magma injection. Sverdrup Basin from SR to coastal IFU. Rifted basement structures limit the migration of tholeiites and alkalic magmas between sub-basins, seen in Figure 2.14, Chapter 2. Large lateral thermal gradient and upwelling mantle—with shear—is generated by either sub-cratonic incubation or a distal plume (See text). Pre-rift TBL of 90 km (depocenter) to 100 km (margin) and crustal thicknesses (35 – 44 km) from Stephenson et al. (1987). Rotated half-graben fault blocks inferred by seismic in other parts of the Sverdrup basin by Beauchamp et al. (2001). Sverdrup basement structure adapted from Embry and Beauchamp (2008). Long axis of magma eddies into and out-of page, parallel to craton's edge. LF – Li Fjord; PMA – Princess Margret Arch; SF – Strand Fjord; SR – Sverdrup Rim; see Fig. 3.1 for location of cross-section.

Hunen, 2014). Such a difference in lithospheric erosion accounts for the range of lithospheric thickness determined by REE inversion modeling (40-70 km; Chapter 2). The sedimentary depo-center of the Sverdrup basin is immediately west of the Princess Margret Arch in the Sverdrup Island Domain (SID in Fig. 3.9; Trettin, 1991). All the voluminous tholeiitic lavas of the Strand Fjord Fm. and Isachsen Fm (Fig. 3.2) erupted in this domain and some were generated beneath extremely thin lithosphere. The age constraints on these thin-lid tholeiites confirm that magma was generated beneath 40 - 45 km lithosphere during all three pulses of the Canadian HALIP (Fig. 3.11). We interpret this as evidence for a tholeiitic magma generation 'pool' that was created during the first pulse and was re-activated during the ~95 and ~81 Ma pulses (Fig. 3.13).

The schematic cross section (Fig. 3.13) is a west to east transect across the Sverdrup basin, depicted in map view on Figure 3.1. Between the thick craton and the thin lithosphere of Strand and Li Fjords, where thinning is at a maximum, a second magma generation 'pool' may have formed beneath the area east of the Princess Margaret Arch (Fig. 3.13). The thicker lithosphere in this area would generate the alkalic basalts sampled in near the basin margin on Fosheim Peninsula (Fig. 3.1).

Bounded by normal faults in the basement, the Princess Margaret Arch would have been a barrier that limited the crossover of intrusions of different magma types. A few lateral injections of tholeiite from the thin SID (lid ~40 - 55km) were emplaced in the crust of the CED (Fig. 3.9), but are likely sills that travelled sub-horizontally between basins, above the basement horst beneath the PMA (Fig. 3.13). However, no alkaline rocks have been sampled that infiltrated the SID from the point of generation east of the PMA.

3.6.8 Is there a room for a plume in the Canadian HALIP?

A central part of understanding the origin of the HALIP magmas is the complex temporal evolution of magma chemistry, which is primarily controlled by the thickness of overlying lithosphere during magma production (Mckenzie and Bickle, 1988). The lithospheric thicknesses presented here have been calculated with an assumed mantle potential temperature of 1400 °C, which is low for a mantle plume (typically 1450-1500 °C; White and McKenzie, 1995). If a plume was present and supplied upwelling mantle to the system, it would enhance the effects that EDC w.s. had on the Canadian HALIP by supplying a larger volume of upwelling mantle, simply due to the enhancement of mantle potential temperature.

The Alpha Ridge is accepted by many as a plume-generated seamount genetically related to the HALIP (Fig. 3.14), yet its mode of generation is disputed. Most publications posit that this submarine volcanic edifice is the manifestation of a plume that originated in the Arctic Ocean at ~120 Ma (Buchan and Ernst, 2006; Døssing et al., 2013). However, this enigmatic feature may also be explained in the EDC model of HALIP magmatism. Below the Alpha ridge lies the

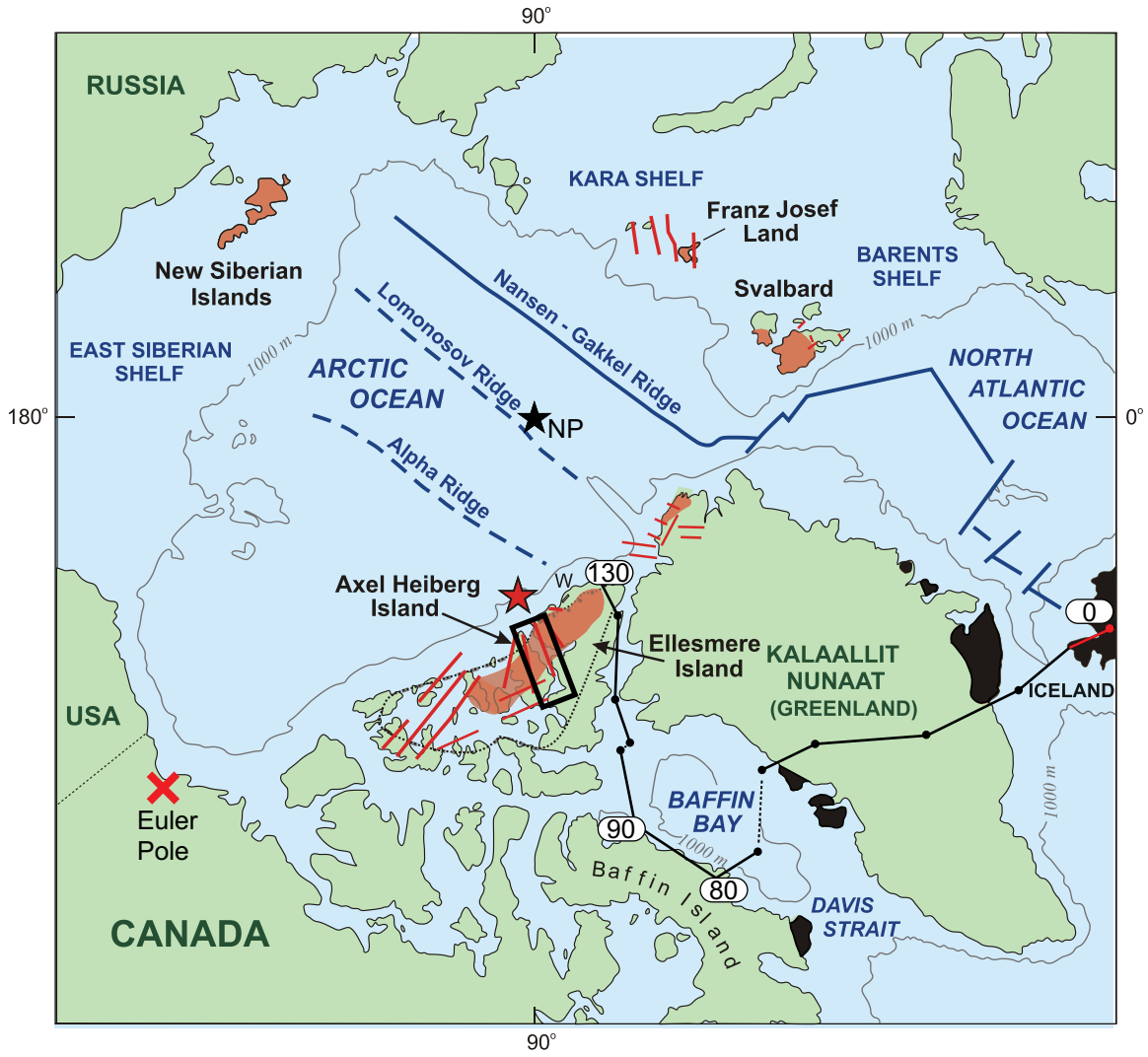

Figure 3.14 Arctic polar projection map displaying the extent of the HALIP (orange shading) modified from Jowitt et al. (2014). Proposed plume track by Lawver and Muller indicate a plume beneath the Sverdrup Basin ca. 130 Ma. This track would have a distal plume during the ~94 and 81 Ma pulses. Study area outlined in black rectangle. Sverdrup Basin (dashed outline). The 62 to 55 Ma North Atlantic LIP in black. Proposed plume head (red star) and dyke orientations (red lines) from Ernst and Buchan (2006).

mechanically weakened Amerasian Basin transform fault that was created during Jurassic rifting about an euler pole in the Mackenzie delta, Yukon, Canada (red X in Fig. 3.14; approximately 67°37'34" N, 129° 8'36" W; Grantz et al., 2011). Magma derived from alternating modes of EDC would pool at the base of the lithosphere, beneath the north coast of Ellesmere and Axel Heiberg Islands, exactly where the epicentre of "plume" magmatism has been proposed (red star, Fig. 3.1; e.g., Buchan and Ernst, 2006). Magma could then transect, and erupt on top of, the mechanically weakened oceanic lithosphere of the Eurasian Basin transform fault. Since this would be the path of least resistance, it would be expected that most of the magmatism

would erupt at a focal point off-shore, under thin oceanic lithosphere and attenuated continental lithosphere. Thus, over time, the Alpha Ridge would build iteratively, rather than in one plume-derived pulse. This hypothesis is reinforced by an Ar/Ar age of 89 ± 1 Ma (plagioclase separate; plateau age includes 82% of gas release) for an alkali basalt dredged from the Alpha Ridge (Jokat et al., 2013). The plume head proposed by Embry and Osadetz (1988) and geophysically imaged by Døssing et al. (2013) could simply be an artefact of EDC-driven upwelling focused on the fault-weakened zone.

The Iceland plume has been proposed to have originated near the Alpha Ridge of the northern coast of Ellesmere Island at around 130 Ma (Forsyth et al., 1986; Lawver and Müller, 1994). It seems plausible that the ~122 Ma HALIP magma pulse, along with the rifting of the Arctic Ocean and continental breakup in the Late Jurassic and Early Cretaceous, are the manifestation of the activity of this plume (Fig. 3.14). We therefore suggest that the ca. 122 Ma circum-Arctic tholeiites (e.g., this study; Corfu et al., 2013; Evenchick et al., 2015; Villeneuve and Williamson, 2006) are the only magmas that should be considered as part of a pure plume-driven HALIP, as they are the only magmas associated with continental breakup between 128 and 120 Ma.

The timing and duration of the 2nd (~92 Ma) and 3rd (~81 Ma) basaltic magma pulses, along with their complex pattern of geochemical "evolution" seems better explained by the alternating modes of EDC. At 90 Ma, the plume's location is calculated to lie off the northern coast of Baffin Island (Fig. 3.14; Lawver and Müller, 1994), 900 km distant from the centre of the Sverdrup Basin. Upwelling mantle driving EDC w.s. could have been supplied from a plume in this location, creating a substantial lateral temperature gradient. Such a distal plume would not exert primary control on the 2nd and 3rd (ca. 95 and 81 Ma) HALIP magma pulses, nor build the thick volcanic Alpha Ridge. Any effects that this "proto-Iceland plume" had on the Canadian HALIP would be secondary effects. Hence, we suggest that the genesis of the complex temporal, spatial, and chemical relations of the Canadian HALIP require a mechanism such as edge-driven convection in addition to the possible initiation by a plume-like upwelling.

3.7 Conclusions

A geographically, geochemically, and temporally diverse sample suite of basaltic intrusions and lavas were collected from Axel Heiberg and Ellesmere Islands, Nunavut. This study is the first reporting of U-Pb ages for intrusive sheets from Axel Heiberg and Ellesmere Islands. The total age distribution of the samples is from 121.1 ± 1.9 Ma to 78.5 ± 1.76 Ma, which is within the range of previously published results (~128 to 76 Ma; Villeneuve and Williamson, 2006; Estrada and Henjes-Kunst, 2013; Estrada, 2015). The U-Pb ages of the intrusive sheets corroborate the Ar/Ar ages provided in the above studies, yet two new ages (U-Pb: 116.8 ± 1.8; and Ar/Ar: 116 ± 3) define an age range previously undiscovered. A xenocrystic zircon that was crystallized from a mafic melt was analysed (model age: 184.6 ± 1.8 Ma) and is the first reported evidence of Jurassic magmatism in the Sverdrup Basin. The new age results, combined with all modern (post-2000) published ages detail a >50 Myr magma emplacement occurring in at least three pulses that peaked around 122 Ma, 95 Ma, and 81 Ma, with gaps of 21 and 6 Ma between pulses with negligible magmatism.

Analysis of the spatial distribution of all published ages revealed no systematic trend in emplacement age with respect to geography for either the intrusives or the lavas. This is contrary to what would be expected for a plume-derived LIP, where the plume track is evident as eruption ages young with increasing proximity to the hot-spot (e.g., Campbell, 2007). Furthermore, the alkalic and tholeiitic basalts erupted contemporaneously during the ~95 Ma and ~81 Ma pulses, segregated by the Carboniferous to Permian basement rift structures. This too is inconsistent with a plume model, where the geochemistry of the erupted basalts would evolve from alkalic to tholeiitic with time.

We posit that a plume may have exerted primary control on the first pulse of the HALIP (~122 Ma), which is exclusively tholeiitic and extends across the circum-Arctic. However, the second and third basaltic pulses, which are characterized by coeval alkalic and tholeiitic basalts, cannot be explained by a standard plume model. A new tectonomagmatic model is required to explain

the 95 Ma and 81 Ma pulses. Edge-driven convection (EDC) is a possible tectonic model for magma genesis and pulsed timing of the Canadian manifestation of the HALIP. The effects of EDC scale in proportion to the size of cratonic mass and the gradient in lithospheric thickness. The Canadian HALIP is adjacent to a cratonic mass that is greater than 4000 km, amplifying magma generation due to enhanced sub-lithospheric incubation, which may account for the >2500 m lava successions and intrusions in the depocenter on west Axel Heiberg Island. The pulsed timing, extended duration, and inter-pulse periodicity of the basaltic magmatism is consistent with alternating effects of EDC.

The mantle plume track proposed by Forsyth et al. (1986) requires the plume to have been beneath the Sverdrup Basin at around 130 Ma. However, at the time of the ~95 Ma pulse, this plume is modeled as beneath pre-rift Baffin Island and Greenland (Lawver and Müller, 1994). Any input this plume had on magma generation and emplacement in the Sverdrup Basin would be 'far-field' and secondary in nature (i.e. shedding mantle that drives EDC). A distal plume would induce a relatively large lateral temperature gradient, inducing a very strong EDC w.s. convection cell, amplifying the magma production of EDC (Kaislaniemi and van Hunen, 2014). EDC convection eddies would exploit the previously rifted basal lithosphere during the second and third pulses, enforcing the geographic distribution of magma types imposed by the Carboniferous to Permian rift structures beneath the Sverdrup Basin, and causing the magma type distribution observed at the surface.

We therefore suggest that the ca. 122 Ma circum-Arctic tholeiites (e.g., this study; Corfu et al., 2013; Evenchick et al., 2015; Villeneuve and Williamson, 2006) are the only magmas that should be considered as part of a pure plume-driven HALIP, as a plume may have been present in the Canadian Arctic during the time of HALIP initiation (ca. 130 Ma). Furthermore, we suggest that the genesis of the complex temporal, spatial, and chemical relations of the final two pluses of the Canadian HALIP require a mechanism of magma generation such as edge-driven convection.

References

Bailey, J.C., and Rasmussen, M.H., 1997, Petrochemistry of Jurassic and Cretaceous tholeiites from Kong Karls Land, Svalbard, and their relation to Mesozoic magmatism in the Arctic, *Polar Research*, v. 16, no. 1, p. 37–62.

Baksi, A.K., 2006, Guidelines for assessing the reliability of $^{40}Ar/^{39}Ar$ plateau ages: Application to ages relevant to hotspot tracks, www.mantleplumes.org, accessed on Oct. 16, 2015.

Beauchamp, B., Harrison, J.C., Utting, J., Brent, T.A., and Pinard, S., 2001, *Carboniferous and Permian subsurface stratigraphy, Prince Patrick Island, Northwest Territories, Canadian Arctic*: Geological Survey of Canada, Bulletin 565.

Bryan, S.E., and Ernst, R.E., 2008, Revised definition of Large Igneous Provinces (LIPs), *Earth-Science Reviews*, v. 86, p. 175–202.

Buchan, K.L., and Ernst, R., 2006, Giant dyke swarms and the reconstruction of the Canadian Arctic islands, Greenland, Svalbard and Franz Josef Land, in: Hanski, E., Mertanen, S., Rämö, T., and Vuollo, J. (Eds.), *Dyke Swarms: Time Markers of Crustal Evolution*, Taylor and Francis Group, London, UK, p. 27–48.

Campbell, I.H., 2007, Testing the plume theory, *Chemical Geology*, v. 241, p. 153–176.

Corfu, F., Polteau, S., Planke, S., Faleide, J.I., Svensen, H., Zayoncheck, A., and Stolbov, N., 2013, U-Pb geochronology of Cretaceous magmatism on Svalbard and Franz Josef Land, Barents Sea Large Igneous Province, *Geological Magazine*, v. 150, no. 6, p. 1127–1135.

Døssing, A., Jackson, H.R., Matzka, J., Einarsson, I., Rasmussen, T.M., Olesen, A. V., and Brozena, J.M., 2013, On the origin of the Amerasia Basin and the High Arctic Large Igneous Province - Results of new aeromagnetic data, *Earth and Planetary Science Letters*, v. 363, p. 219–230.

Embry, A., and Beauchamp, B., 2008, Sverdrup Basin, in: Miall, A. (Ed.), *Sedimentary Basins of the World, Volume 5*, Elsevier B.V., p. 451–471.

Embry, A.F., and Osadetz, K.G., 1988, Stratigraphy and tectonic significance of Cretaceous volcanism in the Queen Elizabeth Islands, Canadian Arctic Archipelago, *Canadian Journal of Earth Sciences*, v. 25, p. 1209–1219.

Ernst, R., and Bleeker, W., 2010, Large igneous provinces (LIPs), giant dyke swarms, and mantle plumes: Significance for breakup events within Canada and adjacent regions from 2.5 Ga to the present, *Canadian Journal of Earth Sciences*, v. 47, p. 695–739.

Ernst, R.E., and Buchan, K.L., 2001, Large mafic magmatic events through time and links to mantle-plume heads, in: Ernst, R.E, and Buchan, K.L. (Eds.), *Mantle Plumes: Their Identification Through Time*, Geological Society of America Special Paper 352, p. 483–575.

Estrada, S., 2015, Geochemical and Sr-Nd isotope variations within Cretaceous continental flood-basalt suites of the Canadian High Arctic, with a focus on the Hassel Formation basalts of northeast Ellesmere Island, *International Journal of Earth Sciences*, v. 104, no. 8, p. 1981–2005.

Estrada, S., and Henjes-Kunst, F., 2013, ^{40}Ar-^{39}Ar and U-Pb dating of Cretaceous continental rift-related magmatism on the northeast Canadian Arctic margin, *Zeitschrift der Deutschen*

Gesellschaft für Geowissenschaften, v. 164, p. 107–130.

Estrada, S., and Henjes-Kunst, F., 2004, Volcanism in the Canadian High Arctic related to the opening of the Arctic Ocean, *Zeitschrift der Deutschen Geologischen Gesellschaft*, v. 154, no. 4, p. 579–603.

Evenchick, C.A., Davis, W.J., Bedard, J.H., Hayward, N., and Friedman, R.M., 2015, Evidence for protracted High Arctic large igneous province magmatism in the central Sverdrup Basin from stratigraphy, geochronology, and paleodepths of saucer-shaped sills, *GSA Bulletin*, v. 127, no. 9/10, p. 1366–1390.

Forsyth, D.A., Morel-A-L'Huissier, P., Asudeh, I., and Green, A.G., 1986, Alpha Ridge and Iceland - Products of the same plume? *Journal of Geodynamics*, v. 6, p. 197–214.

Google Maps, 2016, Ellesmere and the Sverdrup Islands, terrain map, retrieved from https://www.google.ca/maps/@80.4432023,-94.8656865,5z/data=!4m2!6m1!1szaoU7Jghh3Io.keFJTViEExQU

Grantz, A., Hart, P.E., and Childers, V.A., 2011, Geology and tectonic development of the Amerasia and Canada Basins, Arctic Ocean, in: Spencer, A.M., Embry, A.F., Gautier, D.L., Stoupakova, A.V., and Sorensen, K. (Eds.), *Arctic Petroleum Geology*, Memoir 35, The Geological Society of London, London, p. 771–799.

Hamilton, M.A., Pearson, D.G., Thompson, R.N., Kelley, S.P., and Emeleus, C.H., 1998, Rapid eruption of Skye lavas inferred from precise U-Pb and Ar-Ar dating of the Rum and Cuillin plutonic complexes, *Nature*, v. 394, p. 260–263.

Heaman, L.M., 2009, The application of U-Pb geochronology to mafic, ultramafic and alkaline rocks: An evaluation of three mineral standards, *Chemical Geology*, v. 261, no. 1-2, p. 42–51.

Heaman, L.M., and LeCheminant, A.N., 1993, Paragenesis and U-Pb systematics of baddeleyite (ZrO_2), *Chemical Geology*, v. 110, p. 95–126.

Heron, P.J., and Lowman, J.P., 2014, The impact of Rayleigh number on assessing the significance of supercontinent insulation, *Journal of Geophysical Research: Solid Earth*, v. 119, p. 711–733.

Jaffey, A.H., Flynn, K.F., Glendenin, L.E., Bentley, W.C., and Essling, A.M., 1971, Precision measurement of half-lives and specific activities of U^{235} and U^{238}, *Physical Review C*, v. 4, no. 5, p. 1889–1906.

Jaupart, C., and Mareschal, J.-C., 2007, Heat flow and thermal structure of the lithosphere, in: Schubert, G. (Ed.), *Treatise on Geophysics, Volume 6*, Elsevier Ltd., p. 217–251.

Jochum, K.P., Nohl, U., Herwig, K., Lammel, E., Stoll, B., and Hofmann, A.W., 2005, GeoReM: A new geochemical database for reference materials and isotopic standards, *Geostandards and Geoanalytical Research*, v. 29, no. 3, p. 333–338.

Jokat, W., Ickrath, M., and O'Connor, J., 2013, Seismic transect across the Lomonosov and Mendeleev Ridges: Constraints on the geological evolution of the Amerasia Basin, Arctic Ocean, *Geophysical Research Letters*, v. 40, no. 19, p. 5047–5051.

Jowitt, S.M., Williamson, M.-C., and Ernst, R.E., 2014, Geochemistry of the 130 to 80 Ma Canadian High Arctic large igneous province (HALIP) event and implications for Ni-Cu-

PGE prospectivity, *Economic Geology*, v. 109, no. 2, p. 281–307.

Kaislaniemi, L., and van Hunen, J., 2014, Dynamics of lithospheric thinning and mantle melting by edge-driven convection: Application to Moroccan Atlas mountains, *Geochemistry, Geophysics, Geosystems*, v. 15, p. 3175–3189.

Kerr, A.C., 1994, Lithospheric thinning during the evolution of continental large igneous provinces: A case study from the North Atlantic Tertiary province, *Geology*, v. 22, p. 1027–1030.

Kontak, D.J., Jensen, S.M., Dostal, J., Archibald, D.A., and Kyser, T.K., 2001, Cretaceous mafic dyke swarm, Peary Land, northernmost Greenland: Geochronology and petrology, *The Canadian Mineralogist*, v. 39, no. 4, p. 997–1020.

Kuiper, K.F., Deino, A., Hilgen, F.J., Krijgsman, W., Renne, P.R., and Wijbrans, J.R., 2008, Synchronizing rock clocks of Earth history, *Science*, v. 320, no. 5875, p. 500–504.

Lawver, L.A., and Müller, R.D., 1994, Iceland hotspot track, *Geology*, v. 22, no. 4, p. 311–314.

Ludwig, K.R., 2012, Isoplot 3.75. A geochronological toolkit for Microsoft Excel, *Berkley Geochronology Center Special Publications*, v. 5, p. 75.

Maher, H.D., 2001, Manifestations of the Cretaceous High Arctic Large Igneous Province in Svalbard, *The Journal of Geology*, v. 109, p. 91–104.

Mather, K.A., Pearson, D.G., McKenzie, D., Kjarsgaard, B.A., and Priestley, K., 2011, Constraints on the depth and thermal history of cratonic lithosphere from peridotite xenoliths, xenocrysts and seismology, *Lithos*, v. 125, no. 1-2, p. 729–742.

Mattinson, J.M., 2005, Zircon U-Pb chemical abrasion ("CA-TIMS") method: Combined annealing and multi-step partial dissolution analysis for improved precision and accuracy of zircon ages, *Chemical Geology*, v. 220, no. 1-2, p. 47–66.

Mckenzie, D., and Bickle, M.J., 1988, The volume and composition of melt generated by extension of the lithosphere, *Journal of Petrology*, v. 29, no. 3, p. 625–679.

McKenzie, D., and O'Nions, R.K., 1991, Partial melt distributions from inversion of rare earth element concentrations, *Journal of Petrology*, v. 32, no. 5, p. 1021–1091.

Mertzman, S.A., 2000, K-Ar results from the southern Oregon-northern California Cascade Range, *Oregon Geology*, v. 62, no. 4, p. 99–122.

Min, K., Mundil, R., Renne, P.R., and Ludwig, K.R., 2000, A test for systematic errors in 40Ar/39Ar geochronology through comparison with U/Pb analysis of a 1.1-Ga rhyolite, *Geochimica et Cosmochimica Acta*, v. 64, no. 1, p. 73–98.

Morgan, W.J., 1971, Convection plumes in the lower mantle, *Nature*, v. 230, no. 5288, p. 42–43.

Oakey, G.N., and Stephenson, R., 2008, Crustal structure of the Innuitian region of Arctic Canada and Greenland from gravity modelling: Implications for the Palaeogene Eurekan Orogen, *Geophysical Journal International*, v. 173, no. 3, p. 1039–1063.

Okulitch, A. V., 1991, *Geology of the Canadian Arctic Archipelago, Northwest Territories and North Greenland*, Geological Survey of Canada, "A" Series Map, doi: 10.4095/213121.

Osadetz, K.G., and Moore, P.R., 1988, Basic volcanics in the Hassel Formation (mid-Cretaceous) and associated intrusives, Ellesmere Island, District of Franklin, Northwest Territories, Geological Survey of Canada Paper 87-21, 19 p.

Polteau, S., Hendriks, B.W.H., Planke, S., Ganerød, M., Corfu, F., Faleide, J.I., Midtkandal, I., Svensen, H., and Myklebust, R., 2016, The Early Cretaceous Barents Sea Sill Complex: Distribution, $^{40}Ar/^{39}Ar$ geochronology, and implications for carbon gas formation, *Palaeogeography, Palaeoclimatology, Palaeoecology*, v. 441, p. 83–95.

Reidel, S.P., Camp, V.E., Tolan, T.L., and Martin, B.S., 2013, The Columbia River flood basalt province: Stratigraphy, areal extent, volume, and physical volcanology, in: Reidel, S.P, Camp, V.E., Ross, M.E., Wolff, J.A., Martin, B.S., Tolan, T.L., and Wells, R.E. (Eds.), *The Columbia River Flood Basalt Province*, Geological Society of America Special Paper 497, p. 1–43.

Renne, P.R., and Basu, A.R., 1991, Rapid eruption of the Siberian Traps flood basalts at the Permo-Triassic boundary, *Science*, v. 253, no. 11, p. 176–179.

Ricketts, B., Osadetz, K.G., and Embry, A.F., 1985, Volcanic style in the Strand Fiord Formation (Upper Cretaceous), Axel Heiberg Island, Canadian Arctic Archipelago, *Polar Research*, v. 3, p. 107–122.

Sarkar, C., Pearson, D.G., Heaman, L.M., and Woodland, S.J., 2015, Precise Pb isotope ratio determination of picogram-size samples: A comparison between multiple Faraday collectors equipped with 10^{12} Ω amplifiers and multiple ion counters, *Chemical Geology*, v. 395, p. 27–40.

Schaeffer, A.J., and Lebedev, S., 2014, Imaging the North American continent using waveform inversion of global and USArray data: *Earth and Planetary Science Letters*, v. 402, p. 26–41.

Schmitz, M.D., 2012, Radiogenic isotope geochronology, in: Gradstein, F.M., Ogg, J.G., Schmitz, M.D., and Ogg, G. (Eds.), *The Geologic Time Scale 2012*, Elsevier, Amsterdam, p. 115–126.

Schoene, B., Samperton, K.M., Eddy, M.P., Keller, G., Adatte, T., Bowring, S.A., Khadri, S.F.R., and Gertsch, B., 2015, U-Pb geochronology of the Deccan Traps and relation to the end-Cretaceous mass extinction, *Science*, v. 347, no. 6218, p. 182–184.

Stacey, J.S., and Kramers, J.D., 1975, Approximation of terrestrial lead isotope evolution by a two-stage model, *Earth and Planetary Science Letters*, v. 26, no. 2, p. 207–221.

Stephenson, R.A., Embry, A.F., Nakiboglu, S.M., and Hastaoglu, M.A., 1987, Rift-initiated Permian to Early Cretaceous subsidence of the Sverdrup Basin, in Beaumont, C. and Tankard, A.J. eds., *Sedimentary Basins and Basin-Forming Mechanisms*, Canadian Society of Petroleum Geologists, p. 213–231.

Sweeney, J.F., 1985, Geology/geophysics of the Arctic Basin and adjacent seas: Comments about the age of the Canada Basin, in: Husebye, G.L., Johnson, G.L., and Kristoffersen, Y. (Eds.), *Tectonophysics*, v. 114, p. 1–10.

Tegner, C., Storey, M., Holm, P.M., Thorarinsson, S.B., Zhao, X., Lo, C.H., and Knudsen, M.F., 2011b, Magmatism and Eurekan deformation in the High Arctic Large Igneous Province: ^{40}Ar-^{39}Ar age of Kap Washington Group volcanics, North Greenland, *Earth and Planetary Science Letters*, v. 303, no. 3-4, p. 203–214.

Thiede, D.S., and Vasconcelos, P.M., 2010, Paraná flood basalts: Rapid extrusion hypothesis confirmed by new $^{40}Ar/^{39}Ar$ results, *Geology*, v. 38, no. 8, p. 747–750.

Thorarinsson, S.B., Holm, P.M., Tappe, S., Heaman, L.M., and Tegner, C., 2011, Late Cretaceous-Palaeocene continental rifting in the High Arctic: U-Pb geochronology of the Kap Washington Group volcanic sequence, North Greenland, *Journal of the Geological Society*, v. 168, p. 1093–1106.

Trettin, H.P. (Ed.), 1991, *Geology of the Innuitian Orogen and Arctic Platform of Canada and Greenland*, Geological Survey of Canada, 569 p.

Trettin, H.P., and Parrish, R., 1987, Late Cretaceous bimodal magmatism, northern Ellesmere Island: Isotopic age and origin, *Canadian Journal of Earth Sciences*, v. 24, no. 2, p. 257–265.

Vermeesch, P., 2012, On the visualization of detrital age distributions, *Chemical Geology*, v. 312-313, p. 190–194.

Verzhbitskii, E. V, Lobkovskii, L.I., Byakov, A.F., and Kononov, M. V, 2013, The origin and age of the Alpha-Mendeleev and Lomonosov ridges in the Amerasia Basin, *Oceanology*, v. 53, no. 1, p. 89–98.

Villeneuve, M., and Williamson, M.-C., 2006, ^{40}Ar-^{39}Ar dating of mafic magmatism from the Sverdrup Basin Magmatic Province, in: Scott, R.A. and Thurston, D.K. (Eds.), *ICAM IV Proceedings*, Dartmouth, Nova Scotia, p. 206–215.

Van Wagoner, N.A., Williamson, M.-C., Robinson, P.T., and Gibson, I.L., 1986, First samples of acoustic basement recovered from the Alpha Ridge, Arctic Ocean: New constraints for the origin of the ridge, *Journal of Geodynamics*, v. 6, p. 177–196.

Waterton, P.W., Pearson, D.G., Kjarsgaard, B., Hulbert, L., Locock, A., Parman, S., in prep, Origin and thermal evolution of the ultra-fresh 1.9 Ga Winnipegosis Komatiites, Manitoba, Canada

Weber, J.R., 1990, The structures of the Alpha Ridge, Arctic Ocean and Iceland-Faeroe Ridge, North Atlantic: Comparisons and implications for the evolution of the Canada Basin, *Marine Geology*, v. 93, no. 0, p. 43–68.

White, R.S., and McKenzie, D., 1995, Mantle plumes and flood basalts, *Journal of Geophysical Research*, v. 100, no. B9, p. 17,543–17,585.

Williamson, M.-C., 1988, The Cretaceous igneous province of the Sverdrup Basin, Canadian Arctic: Field relations and petrochemical studies, PhD thesis, Dalhousie University, Halifax, NS, 417 p.

Chapter 4

Conclusions

The objective of the present study was to gain insights into the duration of magmatism, temporal variation in geochemistry and the associated temporal and spatial variation in the thickness of the lithosphere in the Canadian High Arctic during the formation of the Cretaceous High Arctic large igneous province (HALIP). Little work has been done on this area due of its remote location, leaving many gaps in knowledge, specifically in the geochronology and trace-element geochemistry of the basalts and intrusions of this expansive Arctic region. The HALIP has been interpreted as a plume-derived LIP due to the apparent radiating dyke swarm originating from a focal point off the coast of northern Ellesmere Island (Buchan and Ernst, 2006), close to the Alpha Ridge submarine volcanic edifice. Recent geochronological studies have begun to question whether a plume-derived origin is the best explanation for the long-lived nature and multiple pulses of HALIP magmatism (Tegner et al., 2011; Estrada, 2015). In this study, samples of a geographically, geochemically, and temporally diverse suite of basaltic intrusions and lavas were collected on Axel Heiberg and Ellesmere Islands, Nunavut. This geographic transect was chosen to obtain samples from the margin of the Sverdrup Basin, near continental North America, and the basin center on Axel Heiberg Island, proximal to the proposed plume head off the northwest coast of Ellesmere Island (e.g. Buchan and Ernst, 2006). Whole-rock geochemistry, U-Pb and Ar/Ar geochronology, Sr-Nd isotope systematics, and REE inversion modelling (following McKenzie and O'Nions, 1991) were conducted. Based on these and published results, a new genetic model for the Canadian HALIP is proposed.

4.1 Geochemistry

The analytical portion of the project involved a detailed study of the trace-element geochemistry of samples collected from the margins of basaltic dykes and sills, whose quenched margin best preserves the eruptive geochemistry. The HALIP is characterized by a bimodal suite of tholeiitic and alkalic basalts. Magma classification in the suite is best accomplished using immobile trace-

element ratios and REE patterns due to the inherent weakness of major-element classification systems that evolve with fractionation. Three nepheline-normative samples from this suite have the same REE patterns as a sample subset classified as alkalic basalts on a Nb/Y vs $Zr/P_2O_5*10^4$ plot (Floyd and Winchester, 1975). The parental magmas of these alkali basalts were likely nepheline-normative, as their REE patterns are indicative of alkalic basalt, yet fractionation has driven these samples to hypersthene-normative. In general, tholeiitic basalts are more likely to have undergone more low temperature hydrothermal alteration and assimilation of crustal components due to their lower overall trace-element abundances. Similar geochemical characteristics and levels of crustal contamination are observed in the Mull and Skye lavas of the British Paleogene (e.g. Thompson, 1982; Kerr et al., 1995).

After accounting for the effects of crustal contamination, Sr-Nd isotope systematics indicate the same mantle source was involved in generating both the alkalic and tholeiitic basalts, without the characteristics of long-term source enrichment via earlier subduction-related metosomatism of mantle peridotite. In the absence of evidence for long-term mantle enrichment, we interpret the variations in REE geochemistry as being due to differences in the physical parameters—primarily the lithospheric "lid" thickness — of the melting environment.

4.2 REE inversion modelling

Samples deemed 'least contaminated' after a rigorous geochemical screening for crustal contamination were modeled for lithospheric lid thickness following McKenzie and O'Nions (1991). The derived lithospheric thicknesses (depth to top of melting column) were classified into two modes ~65 and 45 km, corresponding to alkalic (60-70 km) and tholeiitic (40-60 km) magma types. Seven of the samples modelled for REE inversion are lavas, whose geographic proximity to their site of magma generation is more reliable than the intrusions. Tholeiitic lavas are restricted to the basin centre on central Axel Heiberg Island (Oakey and Stephenson, 2008), whereas alkalic lavas only occur on the basin margins. HALIP intrusive basaltic magmas are systematically distributed and generally follow the same distribution as the lavas, indicating

the same controls on magma generation, with minor lateral injection into other domains. The geographic distribution of the two magma types follows the tectonic domains outlined by Trettin (1991), where tholeiites occur mainly in the heavily rifted Sverdrup Island Domain (SID), and the alkalic basalts occur in the Northern and Central Ellesmere Domains (NED and CED, respectively). These domains are delineated by Late Cretaceous to Paleogene tectonics, such as the Princess Margret Arch in the SID and the Eurekan fold-and-thrust belt in the CED, and run parallel to basement Carboniferous to Permian rift structures caused by the opening of the Arctic Ocean (Trettin, 1991). Magma distribution follows tectonic structure, not a linear track as one would expect with a plume.

4.3 U-Pb and Ar/Ar Geochronology

High-precision U-Pb and Ar/Ar geochronology was conducted on six intrusive basalt samples and two lavas. This study is the first reporting of U-Pb ages for intrusive sheets from Axel Heiberg and Ellesmere Islands. The total age distribution of the samples is from 121.1 ± 1.9 Ma to 78.5 ± 1.76 Ma, which is within the range of previously published results (~128 to 76 Ma; Villeneuve and Williamson, 2006; Estrada and Henjes-Kunst, 2013; Estrada, 2015). The U-Pb ages of the intrusive sheets corroborate the Ar/Ar ages provided in the above studies, yet two new ages (U-Pb: 116.8 ± 1.8; and Ar/Ar: 116 ± 3) define an age range previously undiscovered. A xenocrystic zircon that was crystallized from a mafic melt was analysed (model age: 184.6 ± 1.8 Ma) and is the first reported evidence of Jurassic magmatism in the Sverdrup Basin. The new age results, combined with all modern (post-2000) published ages detail a >50 Myr magma emplacement occurring in at least three pulses that peaked around 122 Ma, 94 Ma, and 81 Ma, with gaps of 14 and 5 Myr between pulses.

4.4 An alternate tectonomagmatic model for the Canadian HALIP

Analysis of the spatial distribution of all published ages revealed no systematic trend in emplacement age with respect to geography for either the intrusives or the lavas. This is contrary

to what would be expected for a plume-derived LIP, where the plume track is evident as eruption ages young with increasing proximity to the hot-spot (e.g. Campbell, 2007). Furthermore, the alkalic and tholeiitic basalts erupted contemporaneously during the ~94 Ma and ~81 Ma pulses, segregated by the Carboniferous to Permian basement rift structures. This too is inconsistent with a plume model, where the geochemistry of the erupted basalts would evolve from alkalic to tholeiitic with time.

We posit that a plume may have exerted primary control on the first pulse of the HALIP (~122 Ma), which is exclusively tholeiitic and extends across the circum-Arctic. However, the second (~94 Ma) and third (81 Ma) basaltic magma pulses, characterized by coeval alkalic and tholeiitic basalts, cannot be explained by a plume model. Edge-driven convection (EDC) is a possible tectonic model for magma genesis proximal to the edge of thick lithospheric mantle (e.g., Kaislaniemi and van Hunen, 2014). Such models are consistent with the long-lived, pulsed timing of the Canadian HALIP. The alternating effects of EDC and EDC modified by shear flow (EDC w.s.; Kaislaniemi and van Hunen, 2014) predict a thickness of erupted lava similar to that seen in the Canadian HALIP.

The mantle plume track proposed by Forsyth et al. (1986) requires the plume, which may have initiated the HALIP, to have been beneath the Sverdrup Basin at around 130 Ma. However, at the time of the ~94 Ma HALIP magma pulse, this plume is calculated to be beneath pre-rift Baffin Island and Greenland (Lawver and Müller, 1994). Any input this plume had on magma generation and emplacement in the Sverdrup Basin would be ‘far-field’ and secondary in nature (i.e. shedding mantle that drives EDC). A distal plume would induce a relatively large lateral temperature gradient, inducing a very strong EDC w.s. convection cell, amplifying the magma production of EDC (Kaislaniemi and van Hunen, 2014). EDC convection eddies would exploit the previously rifted basal lithosphere during the second and third pulses, enforcing the geographic distribution of magma types imposed by the Carboniferous to Permian rift structures beneath the Sverdrup Basin, and causing the magma type distribution observed at the surface.

References

Arndt, N., Chauvel, C., Czamanske, G., and Fedorenko, V., 1998, Two mantle sources, two plumbing systems: tholeiitic and alkaline magmatism of the Maymecha River basin, Siberian flood volcanic province, *Contributions to Mineralogy and Petrology*, v. 133, no. 3, p. 297–313.

Bailey, J.C., and Rasmussen, M.H., 1997, Petrochemistry of Jurassic and Cretaceous tholeiites from Kong Karls Land, Svalbard, and their relation to Mesozoic magmatism in the Arctic, *Polar Research*, v. 16, no. 1, p. 37–62.

Baksi, A.K., 2006, Guidelines for assessing the reliability of $^{40}Ar/^{39}Ar$ plateau ages: Application to ages relevant to hotspot tracks, www.mantleplumes.org, accessed on Oct. 16, 2015.

Balkwill, H.R., 1983, *Geology of Amund Ringnes, Cornwall and Haig-Thomas Islands, District of Franklin*, Geological Survey of Canada Memoir 390, 76 p.

Balkwill, H.R., and Fox, F.G., 1982, Incipient rift zone, western Sverdrup Basin, Arctic Canada, in: Embry, A.F. and Balkwill, H.R. (Eds.), *Arctic Geology and Geophysics*, Canadian Society of Petroleum Geologists Memoir 8, p. 171–187.

Balkwill, H.R., and Haimila, N.E., 1978, K/Ar ages and significance of mafic rocks, Sabine Peninsula, Melville Island, District of Franklin, in: Blackadar, R., Griffin, P., Dumych, H., and Neale, E. (Eds.), *Current Research, Part C*, Geological Survey of Canada Paper No. 78-1C, p. 35-38.

Beauchamp, B., Harrison, J.C., Utting, J., Brent, T.A., and Pinard, S., 2001, *Carboniferous and Permian subsurface stratigraphy, Prince Patrick Island, Northwest Territories, Canadian Arctic*: Geological Survey of Canada, Bulletin 565.

Bouvier, A., Vervoort, J.D., and Patchett, P.J., 2008, The Lu-Hf and Sm-Nd isotopic composition of CHUR: Constraints from unequilibrated chondrites and implications for the bulk composition of terrestrial planets, *Earth and Planetary Science Letters*, v. 273, no. 1-2, p. 48–57.

Bryan, S.E., and Ernst, R.E., 2008, Revised definition of Large Igneous Provinces (LIPs), *Earth-Science Reviews*, v. 86, p. 175–202.

Buchan, K.L., and Ernst, R., 2006, Giant dyke swarms and the reconstruction of the Canadian Arctic islands, Greenland, Svalbard and Franz Josef Land, in: Hanski, E., Mertanen, S., Rämö, T., and Vuollo, J. (Eds.), *Dyke Swarms: Time Markers of Crustal Evolution*, Taylor and Francis Group, London, UK, p. 27–48.

Campbell, I.H., 2007, Testing the plume theory, *Chemical Geology*, v. 241, p. 153–176.

Coffin, M.F., and Eldholm, O., 1992, Volcanism and continental break-up: A global compilation of large igneous provinces, in: Storey, B.C., Alabaster, T., and Pankhurst, R.J. (Eds.), *Magmatism and the Causes of Continental Break-up*, The Geological Society of London Special Publication No. 68, p. 17–30.

Coltice, N., Phillips, B.R., Bertrand, H., Ricard, Y., and Rey, P., 2007, Global warming of the mantle at the origin of flood basalts over supercontinents, *Geology*, v. 35, no. 5, p. 391–394.

Corfu, F., Polteau, S., Planke, S., Faleide, J.I., Svensen, H., Zayoncheck, A., and Stolbov, N., 2013, U-Pb geochronology of Cretaceous magmatism on Svalbard and Franz Josef Land, Barents Sea Large Igneous Province, *Geological Magazine*, v. 150, no. 6, p. 1127–1135.

DePaolo, D.J., and Wasserburg, G.J., 1976, Nd isotopic variations and petrogenic models, *Geophysical Research Letters*, v. 3, no. 5, p. 249–252.

Døssing, A., Jackson, H.R., Matzka, J., Einarsson, I., Rasmussen, T.M., Olesen, A. V., and Brozena, J.M., 2013, On the origin of the Amerasia Basin and the High Arctic Large Igneous Province - Results of new aeromagnetic data, *Earth and Planetary Science Letters*, v. 363, p. 219–230.

Ellam, R.M., 1992, Lithospheric thickness as a control on basalt geochemistry, *Geology*, v. 20, p. 153–156.

Embry, A.F., 1991, Mesozoic history of the Arctic Islands, in: Trettin, H.P. (Ed.), *Geology of the Innuitian Orogen and Arctic Platform of Canada and Greenland*, Geological Survey of Canada, p. 369-433.

Embry, A.F., and Beauchamp, B., 2008, Sverdrup Basin, in: Miall, A. (Ed.), *Sedimentary Basins of the World*, *Volume 5*, Elsevier Ltd., p. 451–471.

Embry, A.F., and Dixon, J., 1990, The breakup unconformity of the Amerasia Basin, Arctic Ocean: Evidence from Arctic Canada, *GSA Bulletin*, v. 102, p. 1526–1534.

Embry, A.F., and Osadetz, K.G., 1988, Stratigraphy and tectonic significance of Cretaceous volcanism in the Queen Elizabeth Islands, Canadian Arctic Archipelago, *Canadian Journal of Earth Sciences*, v. 25, p. 1209–1219.

Ernst, R.E., and Bleeker, W., 2010, Large igneous provinces (LIPs), giant dyke swarms, and mantle plumes: Significance for breakup events within Canada and adjacent regions from 2.5 Ga to the present, *Canadian Journal of Earth Sciences*, v. 47, p. 695–739.

Ernst, R.E., and Buchan, K.L., 2001, Large mafic magmatic events through time and links to mantle-plume heads, in: Ernst, R.E, and Buchan, K.L. (Eds.), Mantle Plumes: Their Identification Through Time, *Geological Society of America Special Paper 352*, p. 483–575.

Estrada, S., 2015, Geochemical and Sr-Nd isotope variations within Cretaceous continental flood-basalt suites of the Canadian High Arctic, with a focus on the Hassel Formation basalts of northeast Ellesmere Island, *International Journal of Earth Sciences*, v. 104, no. 8, p. 1981–2005.

Estrada, S., and Henjes-Kunst, F., 2004, Volcanism in the Canadian High Arctic related to the opening of the Arctic Ocean, *Zeitschrift der Deutschen Geologischen Gesellschaft*, v. 154, no. 4, p. 579–603.

Estrada, S., and Henjes-Kunst, F., 2013, ^{40}Ar-^{39}Ar and U-Pb dating of Cretaceous continental rift-related magmatism on the northeast Canadian Arctic margin, *Zeitschrift der Deutschen Gesellschaft für Geowissenschaften*, v. 164, p. 107–130.

Evenchick, C.A., Davis, W.J., Bedard, J.H., Hayward, N., and Friedman, R.M., 2015, Evidence for protracted High Arctic large igneous province magmatism in the central Sverdrup Basin from stratigraphy, geochronology, and paleodepths of saucer-shaped sills, *GSA Bulletin*, v. 127, no. 9/10, p. 1366–1390.

Farmer, G.L., 2014, Continental basaltic rocks, in: Holland, H.D., Turekian, K.K. (Eds.), *Treatise on Geochemistry, Volume 4*, 2nd Edition, Elsevier Ltd., p. 75–110.

Foley, S., 1992, Vein-plus-wall-rock melting mechanisms in the lithosphere and the origin of potassic alkaline magmas, *Lithos*, v. 28, p. 435–453.

Forsyth, D.A., Asudeh, I., White, D., Jackson, R., Stephenson, R.A., Embry, A.F., and Argyle, M., 1998, Sedimentary basins and basement highs beneath the polar shelf north of Axel Heiberg and Meighen islands, *Bulletin of Canadian Petroleum Geology*, v. 46, no. 1, p. 12–29.

Forsyth, D.A., Morel-A-L'Huissier, P., Asudeh, I., and Green, A.G., 1986, Alpha Ridge and Iceland - Products of the same plume? *Journal of Geodynamics*, v. 6, p. 197–214.

Gibson, S.A., and Geist, D., 2010, Geochemical and geophysical estimates of lithospheric thickness variation beneath Galápagos, *Earth and Planetary Science Letters*, v. 300, p. 275–286.

Gibson, S.A., Geist, D.J., and Richards, M.A., 2015, Mantle plume capture, anchoring, and outflow during Galápagos plume-ridge interaction, *Geochemistry, Geophysics, Geosystems*, v. 16, p. 1634–1655.

Google Maps, 2016, Ellesmere and the Sverdrup Islands, terrain map, retrieved from https://www.google.ca/maps/@80.4432023,-94.8656865,5z/data=!4m2!6m1!1szaoU7Jghh3Io.keFJTViEExQU

Grantz, A., Hart, P.E., and Childers, V.A., 2011, Geology and tectonic development of the Amerasia and Canada Basins, Arctic Ocean, in: Spencer, A.M., Embry, A.F., Gautier, D.L., Stoupakova, A.V., and Sorensen, K. (Eds.), *Arctic Petroleum Geology*, The Geological Society of London Memoir 35, p. 771–799.

Hamilton, M.A., Pearson, D.G., Thompson, R.N., Kelley, S.P., and Emeleus, C.H., 1998, Rapid eruption of Skye lavas inferred from precise U-Pb and Ar-Ar dating of the Rum and Cuillin plutonic complexes, *Nature*, v. 394, p. 260–263.

Harrison, T.M., Copeland, P., Kidd, W.S.F., and Yin, A.N., 1992, Raising Tibet, *Science*, v. 255, no. 5052, p. 1663–1670.

Heaman, L.M., 2009, The application of U-Pb geochronology to mafic, ultramafic and alkaline rocks: An evaluation of three mineral standards, *Chemical Geology*, v. 261, no. 1-2, p. 42–51.

Heaman, L.M., and LeCheminant, A.N., 1993, Paragenesis and U-Pb systematics of baddeleyite (ZrO_2), *Chemical Geology*, v. 110, p. 95–126.

Heron, P.J., and Lowman, J.P., 2014, The impact of Rayleigh number on assessing the significance of supercontinent insulation, *Journal of Geophysical Research: Solid Earth*, v. 119, p. 711–733.

Hole, M.J., Millett, J.M., Rogers, N.W., and Jolley, D.W., 2015, Rifting and mafic magmatism in the Hebridean basins, *Journal of the Geological Society*, v. 172, no. 2, p. 218–236.

Jaffey, A.H., Flynn, K.F., Glendenin, L.E., Bentley, W.C., and Essling, A.M., 1971, Precision measurement of half-lives and specific activities of U^{235} and U^{238}, *Physical Review C*, v. 4, no.

5, p. 1889–1906.

Jaupart, C., and Mareschal, J.-C., 2007, Heat flow and thermal structure of the lithosphere, in: Schubert, G. (Ed.), *Treatise on Geophysics, Volume 6*, Elsevier Ltd., p. 217–251.

Jochum, K.P., Nohl, U., Herwig, K., Lammel, E., Stoll, B., and Hofmann, A.W., 2005, GeoReM: A new geochemical database for reference materials and isotopic standards, *Geostandards and Geoanalytical Research*, v. 29, no. 3, p. 333–338.

Jokat, W., 2003, Seismic investigations along the western sector of Alpha Ridge, Central Arctic Ocean, *Geophysical Journal International*, v. 152, no. 1, p. 185–201.

Jokat, W., Ickrath, M., and O'Connor, J., 2013, Seismic transect across the Lomonosov and Mendeleev Ridges: Constraints on the geological evolution of the Amerasia Basin, Arctic Ocean, *Geophysical Research Letters*, v. 40, no. 19, p. 5047–5051.

Jowitt, S.M., Williamson, M.-C., and Ernst, R.E., 2014, Geochemistry of the 130 to 80 Ma Canadian High Arctic large igneous province (HALIP) event and implications for Ni-Cu-PGE prospectivity, *Economic Geology*, v. 109, no. 2, p. 281–307.

Kaislaniemi, L., and van Hunen, J., 2014, Dynamics of lithospheric thinning and mantle melting by edge-driven convection: Application to Moroccan Atlas mountains, *Geochemistry, Geophysics, Geosystems*, v. 15, p. 3175–3189.

Kerr, J.W., 1976, Geology of outstanding Arctic aerial photographs: 3. Margin of Sverdrup Basin, Lyall River, Devon Island, *Bulletin of Canadian Petroleum Geology*, v. 24, no. 2, p. 139–153.

Kerr, A.C., 1994, Lithospheric thinning during the evolution of continental large igneous provinces: A case study from the North Atlantic Tertiary province, *Geology*, v. 22, p. 1027–1030.

Kerr, A.C., 1995, The geochemistry of the Mull-Morvern Tertiary lava succession, NW Scotland: An assessment of mantle sources during plume-related volcanism, *Chemical Geology*, v. 122, no. 1-4, p. 43–58.

Kerr, A.C., Kempton, P.D., and Thompson, R.N., 1995, Crustal assimilation during turbulent magma ascent (ATA); new isotopic evidence from the Mull Tertiary lava succession, N. W. Scotland, *Contributions to Mineralogy and Petrology*, v. 119, no. 2-3, p. 142–154.

Kerr, A.C., Kent, R.W., Thomson, B.A., Seedhouse, J.K., and Donaldson, C.H., 1999, Geochemical evolution of the Tertiary Mull volcano, western Scotland, *Journal of Petrology*, v. 40, no. 6, p. 873–908.

King, S.D., and Anderson, D.L., 1998, Edge-driven convection, *Earth and Planetary Science Letters*, v. 160, p. 289–296.

Klemme, S., and O'Neill, H.S., 2000, The near-solidus transition from garnet lherzolite to spinel lherzolite, *Contributions to Mineralogy and Petrology*, v. 138, p. 237–248.

Kontak, D.J., Jensen, S.M., Dostal, J., Archibald, D.A., and Kyser, T.K., 2001, Cretaceous mafic dyke swarm, Peary Land, northernmost Greenland: Geochronology and petrology, *The Canadian Mineralogist*, v. 39, no. 4, p. 997–1020.

Kuiper, K.F., Deino, A., Hilgen, F.J., Krijgsman, W., Renne, P.R., and Wijbrans, J.R., 2008, Synchronizing rock clocks of Earth history, *Science*, v. 320, no. 5875, p. 500–504.

Larsen, L.M., Heaman, L.M., Creaser, R.A., Duncan, R.A., Frei, R., and Hutchison, M., 2009, Tectonomagmatic events during stretching and basin formation in the Labrador Sea and the Davis Strait: Evidence from age and composition of Mesozoic to Palaeogene dyke swarms in West Greenland, *Journal of the Geological Society*, v. 166, p. 999–1012.

Lawver, L.A., and Müller, R.D., 1994, Iceland hotspot track, *Geology*, v. 22, no. 4, p. 311–314.

LeCheminant, A.N., and Heaman, L.M., 1989, Mackenzie igneous events, Canada: Middle Proterozoic hotspot magmatism associated with ocean opening, *Earth and Planetary Science Letters*, v. 96, no. 1-2, p. 38–48.

Ludwig, K.R., 2012, Isoplot 3.75. A geochronological toolkit for Microsoft Excel, *Berkley Geochronology Center Special Publications*, v. 5, p. 75.

Lugmair, G.W., and Marti, K., 1978, Lunar initial $^{143}Nd/^{144}Nd$: Differential evolution of the lunar crust and mantle, *Earth and Planetary Science Letters*, v. 39, p. 349–357.

Maher, H.D., 2001, Manifestations of the Cretaceous High Arctic Large Igneous Province in Svalbard, *The Journal of Geology*, v. 109, p. 91–104.

Mather, K.A., Pearson, D.G., McKenzie, D., Kjarsgaard, B.A., and Priestley, K., 2011, Constraints on the depth and thermal history of cratonic lithosphere from peridotite xenoliths, xenocrysts and seismology, *Lithos*, v. 125, no. 1-2, p. 729–742.

Mattinson, J.M., 2005, Zircon U-Pb chemical abrasion ("CA-TIMS") method: Combined annealing and multi-step partial dissolution analysis for improved precision and accuracy of zircon ages, *Chemical Geology*, v. 220, no. 1-2, p. 47–66.

McKenzie, D., and Bickle, M.J., 1988, The volume and composition of melt generated by extension of the lithosphere, *Journal of Petrology*, v. 29, no. 3, p. 625–679.

McKenzie, D., and O'Nions, R.K., 1998, Melt production beneath oceanic islands, *Physics of the Earth and Planetary Interiors*, v. 107, p. 143–182.

McKenzie, D., and O'Nions, R.K., 1991, Partial melt distributions from inversion of rare earth element concentrations, *Journal of Petrology*, v. 32, no. 5, p. 1021–1091.

Mertzman, S.A., 2000, K-Ar results from the southern Oregon-northern California Cascade Range, *Oregon Geology*, v. 62, no. 4, p. 99–122.

Min, K., Mundil, R., Renne, P.R., and Ludwig, K.R., 2000, A test for systematic errors in 40Ar/39Ar geochronology through comparison with U/Pb analysis of a 1.1-Ga rhyolite, *Geochimica et Cosmochimica Acta*, v. 64, no. 1, p. 73–98.

Mitchell, R.H., and Platt, R.G., 1984, The Freemans Cove volcanic suite: Field relations, petrochemistry, and tectonic setting of nephelinite–basanite volcanism associated with rifting in the Canadian Arctic Archipelago, *Canadian Journal of Earth Sciences*, v. 21, no. 4, p. 428–436.

Morgan, W.J., 1971, Convection plumes in the lower mantle, *Nature*, v. 230, no. 5288, p. 42–43.

Oakey, G.N., and Stephenson, R., 2008, Crustal structure of the Innuitian region of Arctic Canada and Greenland from gravity modelling: Implications for the Palaeogene Eurekan Orogen, *Geophysical Journal International*, v. 173, no. 3, p. 1039–1063.

Okulitch, A. V., 1991, *Geology of the Canadian Arctic Archipelago, Northwest Territories and North Greenland*, Geological Survey of Canada, "A" Series Map, doi: 10.4095/213121.

Osadetz, K.G., and Moore, P.R., 1988, Basic volcanics in the Hassel Formation (mid-Cretaceous) and associated intrusives, Ellesmere Island, District of Franklin, Northwest Territories, Geological Survey of Canada Paper 87-21, 19 p.

Patchett, P.J., Embry, A.F., Ross, G.M., Beauchamp, B., Harrison, J.C., Mayr, U., Isachsen, C.E., Rosenberg, E.J., and Spence, G.O., 2004, Sedimentary cover of the Canadian Shield through Mesozoic time reflected by Nd isotopic and geochemical results for the Sverdrup Basin, Arctic Canada: *The Journal of Geology*, v. 112, no. 1, p. 39–57

Pearce, J.A., 1996, A user's guide to basalt discrimination diagrams, in: Wyman, D.A. (Ed.), *Trace Elements and Geochemistry of Volcanic Rocks: Applications for Massive Sulphide Exploration*, Short Course Notes 12, Geological Association of Canada, p. 79–113.

Peate, D.W., and Hawkesworth, C.J., 1996, Lithospheric to asthenospheric transition in Low-Ti flood basalts from southern Paraná, Brazil, *Chemical* Geology, v. 127, p. 1–24.

Polteau, S., Hendriks, B.W.H., Planke, S., Ganerød, M., Corfu, F., Faleide, J.I., Midtkandal, I., Svensen, H., and Myklebust, R., 2016, The Early Cretaceous Barents Sea Sill Complex: Distribution, $^{40}Ar/^{39}Ar$ geochronology, and implications for carbon gas formation, *Palaeogeography, Palaeoclimatology, Palaeoecology*, v. 441, p. 83–95.

Reidel, S.P., Camp, V.E., Tolan, T.L., and Martin, B.S., 2013, The Columbia River flood basalt province: Stratigraphy, areal extent, volume, and physical volcanology, in: Reidel, S.P, Camp, V.E., Ross, M.E., Wolff, J.A., Martin, B.S., Tolan, T.L., and Wells, R.E. (Eds.), *The Columbia River Flood Basalt Province*, Geological Society of America Special Paper 497, p. 1–43.

Renne, P.R., and Basu, A.R., 1991, Rapid eruption of the Siberian Traps flood basalts at the Permo-Triassic boundary, *Science*, v. 253, no. 11, p. 176–179.

Ricketts, B., Osadetz, K.G., and Embry, A.F., 1985, Volcanic style in the Strand Fiord Formation (Upper Cretaceous), Axel Heiberg Island, Canadian Arctic Archipelago, *Polar Research*, v. 3, p. 107–122.

Rotenberg, E., Davis, D.W., Amelin, Y., Ghosh, S., and Bergquist, B.A., 2012, Determination of the decay-constant of ^{87}Rb by laboratory accumulation of ^{87}Sr, *Geochimica et Cosmochimica Acta*, v. 85, p. 41–57.

Sarkar, C., Pearson, D.G., Heaman, L.M., and Woodland, S.J., 2015, Precise Pb isotope ratio determination of picogram-size samples: A comparison between multiple Faraday collectors equipped with 10^{12} Ω amplifiers and multiple ion counters, *Chemical Geology*, v. 395, p. 27–40.

Schaeffer, A.J., and Lebedev, S., 2014, Imaging the North American continent using waveform inversion of global and USArray data: *Earth and Planetary Science Letters*, v. 402, p. 26–41.

Schmitz, M.D., 2012, Radiogenic isotope geochronology, in: Gradstein, F.M., Ogg, J.G., Schmitz, M.D., and Ogg, G. (Eds.), *The Geologic Time Scale 2012*, Elsevier, Amsterdam, p.

115–126.

Schoene, B., Samperton, K.M., Eddy, M.P., Keller, G., Adatte, T., Bowring, S.A., Khadri, S.F.R., and Gertsch, B., 2015, U-Pb geochronology of the Deccan Traps and relation to the end-Cretaceous mass extinction, *Science*, v. 347, no. 6218, p. 182–184.

Stacey, J.S., and Kramers, J.D., 1975, Approximation of terrestrial lead isotope evolution by a two-stage model, *Earth and Planetary Science Letters*, v. 26, no. 2, p. 207–221.

Stephenson, R.A., Embry, A.F., Nakiboglu, S.M., and Hastaoglu, M.A., 1987, Rift-initiated Permian to Early Cretaceous subsidence of the Sverdrup Basin, in Beaumont, C. and Tankard, A.J. eds., *Sedimentary Basins and Basin-Forming Mechanisms*, Canadian Society of Petroleum Geologists, p. 213–231.

Stevens, R.D., Delabio, R.N., and Lachance, G.R., 1982, Age determinations and geological studies: K-Ar isotopic ages, Report 15, Geological Survey of Canada Paper 81-2, 56 p.

Sweeney, J.F., 1985, Geology/geophysics of the Arctic Basin and adjacent seas: Comments about the age of the Canada Basin, in: Husebye, G.L., Johnson, G.L., and Kristoffersen, Y. (Eds.), *Tectonophysics*, v. 114, p. 1–10.

Tarduno, J.A., Brinkman, D.B., Renne, P.R., Cottrell, R.D., Scher, H., and Castillo, P., 1998, Evidence for extreme climatic warmth from Late Cretaceous Arctic vertebrates, *Science*, v. 282, no. 5397, p. 2241–2244.

Tegner, C., Storey, M., Holm, P.M., Thorarinsson, S.B., Zhao, X., Lo, C.H., and Knudsen, M.F., 2011, Magmatism and Eurekan deformation in the High Arctic Large Igneous Province: ^{40}Ar-^{39}Ar age of Kap Washington Group volcanics, North Greenland, *Earth and Planetary Science Letters,* v. 303, no. 3-4, p. 203–214.

Thiede, D.S., and Vasconcelos, P.M., 2010, Paraná flood basalts: Rapid extrusion hypothesis confirmed by new 40Ar/39Ar results, *Geology*, v. 38, no. 8, p. 747–750.

Thompson, R.N., 1982, Magmatism of the British Tertiary Volcanic Province: *Scottish Journal of Geology*, v. 18, p. 49–107

Thorarinsson, S.B., Holm, P.M., Tappe, S., Heaman, L.M., and Tegner, C., 2011, Late Cretaceous-Palaeocene continental rifting in the High Arctic: U-Pb geochronology of the Kap Washington Group volcanic sequence, North Greenland, *Journal of the Geological Society*, v. 168, p. 1093–1106

Trettin, H.P. (Ed.), 1991, *Geology of the Innuitian Orogen and Arctic Platform of Canada and Greenland*, Geological Survey of Canada, 569 p.

Trettin, H.P., and Parrish, R., 1987, Late Cretaceous bimodal magmatism, northern Ellesmere Island: Isotopic age and origin, *Canadian Journal of Earth Sciences*, v. 24, no. 2, p. 257–265.

Van Wagoner, N.A., Williamson, M.-C., Robinson, P.T., and Gibson, I.L., 1986, First samples of acoustic basement recovered from the Alpha Ridge, Arctic Ocean: New constraints for the origin of the ridge, *Journal of Geodynamics*, v. 6, p. 177–196.

Vermeesch, P., 2012, On the visualization of detrital age distributions, *Chemical Geology*, v. 312-313, p. 190–194.

Verzhbitskii, E. V, Lobkovskii, L.I., Byakov, A.F., and Kononov, M. V, 2013, The origin and age of the Alpha-Mendeleev and Lomonosov ridges in the Amerasia Basin, *Oceanology*, v. 53, no. 1, p. 89–98.

Villeneuve, M., and Williamson, M.-C., 2006, ^{40}Ar-^{39}Ar dating of mafic magmatism from the Sverdrup Basin Magmatic Province, in: Scott, R.A. and Thurston, D.K. (Eds.), *ICAM IV Proceedings*, Dartmouth, Nova Scotia, p. 206–215.

Waterton, P.W., Pearson, D.G., Kjarsgaard, B., Hulbert, L., Locock, A., Parman, S., in prep, Origin and thermal evolution of the ultra-fresh 1.9 Ga Winnipegosis Komatiites, Manitoba, Canada

Weber, J.R., and Sweeney, J.F., 1990, Ridges and basins in the central Arctic Ocean, in: Grantz, A.L., Johnson, L., and Sweeney, J.F. (Eds.), *The Geology of North America, Volume L, The Arctic Ocean Region*, The Geological Society of America, p. 305-336.

White, R.S, and McKenzie, D., 1989, Magmatism at rift zones: The generation of volcanic continental margins and flood basalts, *Journal of Geophysical Research*, v. 94, no. B6, p. 7685–7729.

White, R.S., and McKenzie, D., 1995, Mantle plumes and flood basalts, *Journal of Geophysical Research*, v. 100, no. B9, p. 17,543–17,585.

White, R.S., Minshull, T.A., Bickle, M.J., and Robinson, C.J., 2001, Melt generation at very slow-spreading oceanic ridges: Constraints from geochemical and geophysical data, *Journal of Petrology*, v. 42, no. 6, p. 1171–1196.

Williamson, M.-C., 1988, The Cretaceous igneous province of the Sverdrup Basin, Canadian Arctic: Field relations and petrochemical studies, PhD thesis, Dalhousie University, Halifax, NS, 417 p.

Appendix A

Table A – Major- and trace-element geochemistry

Sample no.		DMD101B	DMD102	DMD104M	DMD106	DMD107B	DMD108M	DMD110	DMD111M
TE classification		tholeiitic	alkalic	alkalic	alkalic	alkalic	tholeiitic	alkalic	tholeiitic
Sample type		sheet	sheet	dyke	sheet	dyke	sheet	dyke	sheet
Latitude (°N)		79.894356	79.893911	79.897143	79.907988	79.899534	79.902028	79.906119	79.897664
Longitude (°W)		82.582619	82.606739	82.587027	82.59822	82.591637	82.672886	82.68168	82.674483
	1σ (rel.) ‡								
SiO_2	*0.79%*	46.9	46.2	47.1	47.1	46.3	49.4	46.8	49.4
TiO_2	*1.3%*	3.04	3.73	3.33	3.39	3.64	2.61	3.42	2.53
Al_2O_3	*0.68%*	16.6	14.3	14.3	14.3	14.3	13.7	14.6	14.1
Fe_2O_{3T}	*1.1%*	13.1	16.0	15.3	15.4	15.5	15.2	15.2	15.0
MnO	*0.71%*	0.14	0.25	0.22	0.20	0.21	0.22	0.20	0.22
MgO	*0.88%*	2.90	5.73	6.02	5.64	5.72	5.36	5.62	5.61
CaO	*0.58%*	13.3	8.8	9.7	8.9	9.7	8.7	10.6	7.7
Na_2O	*1.2%*	2.76	3.04	2.59	3.17	2.79	3.66	2.34	3.46
K_2O	*3.7%*	1.13	1.16	1.02	1.35	1.07	0.96	0.90	1.70
P_2O_5	*3.5%*	0.35	0.86	0.56	0.56	0.63	0.32	0.57	0.31
Total	*0.09%*	100.1	100.0	100.1	99.9	99.9	100.1	100.2	99.9
LOI	*8.0%*	8.29	1.59	1.30	1.75	1.15	1.14	2.19	1.37
Mg#		16	24	25	24	24	23	24	24
	1σ								
Ba	*16*	174	619	309	944	457	163	365	225
Ce	*1.6*	44.3	59.5	60.4	58.3	51.7	45.7	60.7	42.2
Co†	*1.1*	39	57	55	54	61	52	58	53
Cr†	*0.67*	87	86	95	69	70	79	87	94
Cs	*0.033*	0.73	0.49	1.71	0.67	0.30	0.94	3.92	0.75
Cu	*0.97*	198.9	23.4	35.8	41.2	34.7	89.7	43.6	59.5
Dy	*0.24*	6.8	6.2	5.7	6.3	4.1	7.3	6.4	7.0
Er	*0.13*	3.83	2.92	2.70	3.04	1.92	4.04	3.09	4.02
Eu	*0.030*	2.00	3.41	2.29	2.63	2.31	2.03	2.52	2.02
Ga	*0.81*	21.5	21.1	23.3	23.3	20.0	20.6	22.9	21.2
Gd	*0.10*	6.31	7.77	6.68	7.34	5.38	6.90	7.46	6.75
Hf	*0.18*	5.17	4.43	4.51	3.41	4.12	4.40	4.98	4.10
Ho	*0.040*	1.37	1.13	1.04	1.15	0.75	1.42	1.17	1.40
La	*1.4*	18.7	29.2	23.9	29.2	22.2	19.3	26.5	19.1
Lu	*0.022*	0.53	0.35	0.32	0.33	0.20	0.52	0.35	0.51
Mo	*12*	1.19	1.32	1.24	1.61	1.49	1.00	1.30	1.07
Nb	*0.23*	15.1	26.2	24.8	27.2	20.0	16.4	26.9	15.3
Nd	*0.54*	23.6	34.6	31.2	33.9	26.3	26.9	34.7	25.4
Ni†	*1.2*	41	38	46	39	33	40	47	41
Pb	*0.36*	5.59	1.74	4.16	4.56	3.58	2.18	4.60	3.38
Pr	*0.12*	5.18	7.64	7.00	7.72	5.95	5.97	7.72	5.61
Rb	*1.7*	25.5	22.9	25.5	37.5	16.4	34.0	24.7	47.2
Sc†	*1.1*	58	19	21	21	22	29	24	24
Sm	*0.16*	5.98	7.78	7.14	7.60	5.80	6.65	7.89	6.25
Sr	*13*	208	522	487	583	416	302	568	261
Ta	*0.028*	0.93	1.52	1.48	1.58	1.16	0.99	1.60	0.97
Tb	*0.04*	1.08	1.12	1.03	1.09	0.77	1.18	1.14	1.13
Th	*0.27*	2.90	2.78	3.08	3.13	2.07	2.50	3.31	2.45
U	*0.08*	0.95	0.76	0.97	0.93	0.77	0.72	1.04	0.70
V†	*13*	537	267	286	291	308	343	304	326
Y	*1.2*	35.7	31.1	32.4	30.9	17.8	40.1	32.8	38.1
Yb	*0.14*	3.64	2.41	2.23	2.40	1.48	3.53	2.51	3.51
Zn†	*3.6*	96	112	128	138	107	92	133	115
Zr	*4.8*	194	186	198	111	174	171	197	147

Major elements measured from an anhydrous powder post LOI determination, therefore the total is both anhydrous and not equal to 100

Mg# calculated on a cation basis by Mg# = 100 x Mg / (Mg +Fe^{2+}), with FeO = 0.9 x Fe_2O_{3T}

†XRF Powder Briquette analyses, all others solution ICP-MS

‡1σ (relative) for the major elements calculated from 10 OKUM standards (Waterton, in prep.)

Appendix A - Continued

Sample	DMD112	DMD113M	DMD114M	DMD115B	DMD116M	DMD119M	DMD120M	DMD121	DMD122M
TE class.	tholeiitic	alkalic	tholeiitic	alkalic	tholeiitic	alkalic	alkalic	alkalic	tholeiitic
Smp. type	sheet	sheet	sheet	sheet	sheet	sheet	dyke	sheet	dyke
Lat. (°N)	79.897852	79.855478	79.855792	79.858336	79.867139	79.5804	79.320833	79.320833	79.323188
Long. (°W)	82.671096	82.53175	82.530123	82.534878	82.562977	83.221723	84.166354	84.166354	84.069095
SiO_2	50.0	47.6	48.7	50.6	50.3	47.0	47.8	41.4	47.5
TiO_2	2.48	4.02	2.08	3.27	2.60	3.76	3.37	3.62	3.06
Al_2O_3	13.8	13.1	14.5	13.2	13.9	14.0	14.5	16.5	15.2
Fe_2O_{3T}	14.6	16.3	14.2	15.1	14.9	15.6	14.8	15.1	14.0
MnO	0.23	0.26	0.21	0.27	0.20	0.25	0.19	0.16	0.10
MgO	5.65	4.72	6.70	3.98	5.41	5.72	4.89	1.96	2.73
CaO	8.2	8.2	11.1	7.0	8.4	7.7	10.4	15.4	13.2
Na_2O	3.28	4.19	2.39	3.57	3.19	3.88	2.62	3.52	3.24
K_2O	1.42	0.65	0.32	1.80	0.87	1.08	1.10	1.28	0.56
P_2O_5	0.30	1.08	0.20	0.94	0.32	1.01	0.57	0.64	0.35
Total	100.0	100.1	100.3	99.8	100.1	100.0	100.3	99.6	99.9
LOI	1.27	1.58	0.49	1.78	1.46	2.31	4.34	11.86	8.76
Mg#	25	20	29	18	24	24	22	10	14
Ba	232	306	58	686	118	454	337	289	117
Ce	42.3	73.2	21.4	66.3	38.0	58.7	57.0	59.5	51.1
Co†	55	47	52	55	54	54	52	48	47
Cr†	88	75	122	97	88	107	62	62	92
Cs	0.82	0.89	0.69	0.68	0.25	1.15	0.48	0.35	0.30
Cu	98.8	18.9	198.5	23.5	93.1	10.1	41.1	42.4	197.2
Dy	7.1	8.8	5.9	7.0	5.1	6.3	6.0	6.1	9.5
Er	3.88	3.98	3.34	3.54	2.81	3.14	2.98	2.94	5.46
Eu	1.98	3.77	1.54	3.97	1.55	3.66	2.47	2.56	2.24
Ga	21.0	24.7	20.5	21.7	18.5	21.9	22.2	24.4	22.2
Gd	6.55	10.58	5.16	8.57	5.06	7.84	7.30	7.35	8.68
Hf	4.29	5.23	3.26	3.89	4.15	3.96	4.78	4.71	5.82
Ho	1.39	1.60	1.19	1.31	1.01	1.16	1.11	1.12	1.88
La	17.9	30.2	7.9	31.5	14.1	28.7	28.8	27.3	24.6
Lu	0.51	0.44	0.44	0.41	0.35	0.36	0.34	0.33	0.73
Mo	0.76	1.73	0.58	1.63	1.16	1.63	1.73	1.11	1.16
Nb	15.9	31.4	8.1	31.2	13.9	25.8	26.4	27.0	17.0
Nd	25.4	46.4	15.7	39.6	19.9	34.8	33.2	33.3	31.2
Ni†	46	22	97	37	41	36	37	39	43
Pb	3.88	2.86	12.84	2.21	2.36	1.96	5.60	4.56	2.17
Pr	5.61	9.88	3.10	8.78	4.40	7.73	7.68	7.44	6.93
Rb	45.9	16.1	6.8	36.3	20.2	35.2	27.6	24.3	13.0
Sc†	29	25	33	21	31	19	23	33	47
Sm	6.39	11.05	4.69	8.80	5.08	7.92	7.56	7.54	8.02
Sr	292	662	188	592	162	430	517	472	265
Ta	0.97	1.89	0.52	1.71	0.81	1.51	1.59	1.56	1.07
Tb	1.14	1.61	0.93	1.27	0.84	1.14	1.08	1.12	1.49
Th	2.36	2.80	0.77	2.52	1.88	2.51	3.25	3.09	3.68
U	0.69	0.86	0.24	0.68	0.72	0.70	1.02	0.97	0.91
V†	322	243	355	289	329	283	307	358	479
Y	38.4	43.2	33.0	36.0	24.5	32.2	30.3	32.0	52.0
Yb	3.46	3.01	2.98	2.85	2.47	2.51	2.43	2.39	4.95
Zn†	150	119	120	106	82	87	115	151	144
Zr	164	207	121	163	156	164	192	193	218

Major elements measured from an anhydrous powder post LOI determination, therefore the total is both anhydrous and not equal to 100

Mg# calculated on a cation basis by Mg# = 100 x Mg / (Mg +Fe^{2+}), with FeO = 0.9 x Fe_2O_{3T}

†XRF Powder Briquette analyses, all others solution ICP-MS

Appendix A - Continued

Sample	DMD124M	DMD125M	DMD128	DMD129	DMD130	DMD132	DMD133	DMD134	DMD135
TE class.	alkalic	tholeiitic	tholeiitic	tholeiitic	tholeiitic	tholeiitic	tholeiitic	alkalic	alkalic
Smp. type	sheet	sheet	sheet	sheet	sheet	sheet	sheet	dyke	sheet
Lat. (°N)	79.81344	79.857203	79.494632	79.492288	78.151746	78.188749	78.224897	78.455243	78.772843
Long. (°W)	86.41845	87.026007	87.644313	87.64697	87.316268	87.219387	87.376388	87.318317	86.568493
SiO_2	54.6	47.5	50.3	49.6	52.4	57.0	50.3	50.2	52.7
TiO_2	2.05	3.69	3.23	3.25	3.10	2.34	2.27	2.86	3.26
Al_2O_3	15.4	14.7	12.8	12.6	13.6	14.4	13.1	13.7	13.7
Fe_2O_{3T}	11.9	13.3	16.0	17.1	15.1	11.1	15.9	15.7	14.5
MnO	0.24	0.22	0.23	0.27	0.23	0.24	0.28	0.22	0.21
MgO	2.21	1.83	4.72	4.91	3.93	2.06	5.25	4.54	4.20
CaO	6.1	14.4	9.0	8.0	7.7	7.8	9.7	8.9	8.1
Na_2O	4.26	2.85	2.66	3.04	2.82	3.51	2.37	2.79	2.81
K_2O	2.39	1.04	0.76	0.78	1.07	0.93	0.49	0.78	0.46
P_2O_5	0.75	0.47	0.41	0.36	0.40	0.49	0.21	0.34	0.40
Total	100.0	100.0	100.2	99.9	100.3	99.9	99.9	100.0	100.4
LOI	2.07	10.10	1.44	1.53	6.68	5.62	3.66	4.36	3.57
Mg#	14	11	20	20	18	14	22	20	20
Ba	994	260	159	173	178	204	102	166	108
Ce	85.9	75.2	53.8	58.4	24.4	32.2	26.6	40.9	29.3
Co†	28	34	52	58	43	27	53	51	47
Cr†	28	60	62	38	30	27	34	48	32
Cs	1.29	1.01	2.42	1.68	0.21	0.82	0.46	0.31	0.44
Cu	7.0	208.9	162.9	139.5	20.6	9.1	145.9	91.1	47.8
Dy	8.6	10.1	9.7	8.9	6.4	7.9	6.5	3.6	3.9
Er	4.44	5.62	5.21	5.11	3.62	4.42	3.72	1.89	1.96
Eu	4.49	2.80	2.55	2.32	1.68	1.87	1.66	1.24	1.24
Ga	27.8	23.1	23.0	22.7	21.5	23.3	20.6	19.0	19.4
Gd	10.20	9.65	9.05	8.37	5.59	6.63	5.64	3.96	4.00
Hf	6.82	7.06	6.57	5.70	5.44	7.74	3.63	4.17	5.05
Ho	1.62	1.97	1.85	1.83	1.29	1.59	1.31	0.70	0.74
La	36.8	32.2	25.0	24.9	9.1	11.6	10.0	13.8	8.2
Lu	0.57	0.74	0.66	0.71	0.48	0.58	0.48	0.22	0.22
Mo	1.97	1.66	1.48	0.89	1.19	1.70	0.55	1.51	1.45
Nb	36.6	34.1	19.6	22.4	15.7	20.2	8.5	18.1	16.7
Nd	46.8	41.0	33.9	33.1	17.5	22.6	18.3	18.7	15.3
Ni†	1	25	38	29	7	3	35	25	21
Pb	10.18	6.47	4.16	4.58	5.50	4.82	3.80	3.58	4.09
Pr	11.02	9.53	7.32	7.55	3.60	4.64	3.72	4.19	3.22
Rb	42.8	26.4	32.7	29.7	13.2	6.3	15.3	17.0	6.2
Sc†	15	43	31	33	35	29	32	32	30
Sm	9.89	9.46	8.59	8.09	5.17	6.56	5.22	4.31	4.16
Sr	514	376	235	252	188	137	209	154	177
Ta	2.39	1.83	1.23	1.28	0.95	1.20	0.53	0.99	0.93
Tb	1.50	1.60	1.52	1.45	1.01	1.21	1.02	0.62	0.67
Th	5.10	4.68	3.63	3.46	1.68	2.04	1.75	1.71	1.33
U	1.26	1.17	0.95	0.78	0.86	1.27	0.49	0.91	0.93
V†	124	506	350	410	309	191	401	375	337
Y	45.0	56.9	52.2	51.1	34.3	38.0	37.2	13.0	14.0
Yb	3.86	5.12	4.56	4.68	3.30	4.09	3.24	1.56	1.59
Zn†	175	297	144	112	189	135	116	129	139
Zr	294	285	252	224	204	300	131	163	202

Major elements measured from an anhydrous powder post LOI determination, therefore the total is both anhydrous and not equal to 100

Mg# calculated on a cation basis by Mg# = 100 x Mg / (Mg +Fe^{2+}), with FeO = 0.9 x Fe_2O_{3T}

†XRF Powder Briquette analyses, all others solution ICP-MS

Appendix A - Continued

Sample	DMD137	DMD140M	DMD141	DMD143A	DMD143B	DMD143C	DMD143D	DMD144	DMD145M
TE class.	tholeiitic	tholeiitic	tholeiitic	alkalic	alkalic	alkalic	alkalic	alkalic	alkalic
Smp. type	sheet	sheet	dyke	Lava flow	Lava flow	Lava flow	Lava flow	sheet	dyke
Lat. (°N)	78.956119	80.536987	80.537247	81.398632	81.398632	81.399291	81.399291	81.0168	81.060496
Long. (°W)	86.195025	85.961462	85.958702	90.109512	90.109512	90.117356	90.117356	89.497381	86.839593
SiO_2	51.3	52.0	50.4	50.7	52.4	47.0	48.2	49.4	49.5
TiO_2	2.26	3.19	2.73	2.80	2.60	3.40	2.76	3.45	3.00
Al_2O_3	13.3	14.1	13.9	16.9	16.1	15.2	17.1	13.4	12.5
Fe_2O_{3T}	15.9	16.5	15.7	10.7	10.9	13.8	11.9	14.6	16.5
MnO	0.22	0.21	0.23	0.53	0.51	0.60	0.28	0.21	0.24
MgO	5.20	4.69	5.17	3.53	3.25	4.85	4.63	5.35	4.94
CaO	8.9	4.6	8.1	7.8	6.5	9.3	9.0	9.4	9.4
Na_2O	2.47	3.81	2.49	4.35	4.54	3.53	3.44	2.59	2.50
K_2O	0.55	0.84	1.04	2.11	2.63	1.52	1.71	0.76	0.98
P_2O_5	0.21	0.33	0.36	0.83	0.94	0.82	0.82	0.37	0.34
Total	100.4	100.2	100.1	100.1	100.4	100.1	99.8	99.6	99.8
LOI	1.85	4.17	2.30	2.02	1.75	1.20	1.94	0.53	0.04
Mg#	22	20	22	22	20	23	25	24	21
Ba	86	409	300	578	678	586	677	149	272
Ce	29.0	44.3	53.5	54.0	28.6	97.7	112.6	43.2	56.5
Co†	57	55	55	31	27	45	37	22	54
Cr†	39	34	36	14	6	11	30	135	52
Cs	1.05	0.33	1.52	0.25	0.29	0.19	0.33	0.88	1.44
Cu	147.1	123.9	74.9	19.6	16.9	9.9	23.6	210.8	190.6
Dy	7.0	7.7	7.3	3.5	2.3	6.4	6.0	8.3	9.2
Er	3.96	4.09	4.13	1.81	1.15	3.06	2.90	4.12	5.34
Eu	1.72	2.00	2.07	1.43	1.10	3.18	2.89	2.58	2.24
Ga	21.6	27.6	22.1	18.8	18.5	20.0	19.7	23.8	22.6
Gd	6.05	7.37	7.21	4.11	3.01	8.75	8.71	8.44	8.57
Hf	4.06	4.86	5.22	5.59	6.61	4.68	5.26	5.88	5.89
Ho	1.39	1.52	1.48	0.67	0.41	1.18	1.09	1.53	1.88
La	11.0	18.6	22.8	19.9	17.4	48.1	52.7	16.6	25.7
Lu	0.52	0.51	0.56	0.22	0.14	0.36	0.36	0.50	0.66
Mo	0.55	1.42	0.83	2.36	2.69	0.86	1.37	0.78	1.43
Nb	9.1	16.0	19.9	56.6	54.3	72.4	80.3	15.1	19.7
Nd	19.4	26.8	29.5	21.1	17.3	49.2	52.8	30.2	31.7
Ni†	35	32	26	8	3	2	16	65	37
Pb	3.90	2.33	6.49	4.73	5.74	3.94	4.40	2.22	5.86
Pr	4.03	5.71	6.80	4.93	4.20	12.04	13.30	6.09	6.98
Rb	19.7	31.9	33.2	27.1	31.2	37.5	46.2	24.4	40.7
Sc†	35	35	31	16	13	24	19	27	36
Sm	5.56	7.12	6.88	4.48	3.38	9.44	9.53	8.12	7.96
Sr	187	298	471	392	188	676	777	313	191
Ta	0.59	0.93	1.17	3.37	2.70	3.81	4.56	0.94	1.16
Tb	1.11	1.22	1.21	0.62	0.43	1.24	1.20	1.42	1.44
Th	2.00	2.57	3.74	2.32	1.42	4.64	5.82	1.87	3.65
U	0.56	0.74	0.97	1.25	1.70	0.98	1.52	0.57	0.89
V†	368	388	350	189	151	277	250	349	353
Y	39.5	42.0	41.5	14.8	7.7	32.4	30.9	44.6	54.7
Yb	3.52	3.68	3.75	1.52	0.98	2.49	2.48	3.48	4.64
Zn†	146	155	116	105	114	102	89	95	147
Zr	148	197	210	250	309	195	224	226	241

Major elements measured from an anhydrous powder post LOI determination, therefore the total is both anhydrous and not equal to 100

Mg# calculated on a cation basis by Mg# = 100 x Mg / (Mg +Fe^{2+}), with FeO = 0.9 x Fe_2O_{3T}

†XRF Powder Briquette analyses, all others solution ICP-MS

Appendix A - Continued

Sample	DMD147	DMD148	DMD149	DMD152	DMD153A	DMD153B	DMD153E	DMD154M	DMD156
TE class.	alkalic	alkalic	alkalic	alkalic	alkalic	alkalic	alkalic	tholeiitic	alkalic
Smp. type	sheet	sheet	sheet	sheet	Lava flow	Lava flow	Lava flow	sheet	sheet
Lat. (°N)	81.091248	81.063544	80.600271	80.497389	81.219785	81.219785	81.221149	81.564941	81.565809
Long. (°W)	85.759936	85.761065	86.247888	90.060132	92.03609	92.03609	92.045623	91.357157	91.355324
SiO_2	49.3	50.1	51.0	51.7	50.8	53.7	61.1	50.2	47.7
TiO_2	2.73	3.24	2.15	1.98	2.68	2.58	3.61	3.70	2.39
Al_2O_3	13.6	12.6	15.3	13.5	14.3	14.8	13.5	13.8	14.1
Fe_2O_{3T}	16.1	16.5	15.9	12.8	13.4	10.8	8.6	15.1	11.0
MnO	0.31	0.27	0.32	0.20	0.11	0.17	0.08	0.27	0.15
MgO	6.14	3.85	5.65	6.11	3.93	4.27	1.97	4.80	10.48
CaO	8.7	7.9	5.8	9.9	10.1	6.4	3.4	7.4	10.0
Na_2O	2.38	2.71	2.76	2.53	3.78	5.79	5.89	3.41	2.57
K_2O	0.44	1.54	0.68	0.97	0.73	1.25	1.21	0.75	0.55
P_2O_5	0.31	1.11	0.21	0.20	0.47	0.50	0.76	0.48	0.52
Total	100.0	99.8	99.9	99.9	100.4	100.3	100.1	100.0	99.5
LOI	1.69	1.56	4.44	1.33	8.83	6.43	3.05	1.85	4.22
Mg#	25	17	23	29	20	25	17	21	45
Ba	137	437	131	180	124	330	222	163	624
Ce	36.5	115.5	37.4	39.6	55.2	69.6	89.3	71.9	82.8
Co†	60	40	63	10	50	42	30	51	58
Cr†	51	38	40	79	329	328	81	50	420
Cs	1.52	2.32	0.93	0.85	1.44	0.39	0.37	0.49	3.11
Cu	118.2	53.2	171.3	112.9	79.8	29.2	28.0	44.3	50.2
Dy	7.1	12.8	6.7	6.1	4.8	4.6	7.1	7.9	4.8
Er	3.97	7.00	3.75	3.44	1.98	1.94	2.73	4.19	2.25
Eu	2.11	3.95	1.60	1.64	2.29	2.13	3.27	2.58	2.20
Ga	21.6	24.0	23.4	20.0	18.9	16.1	16.6	25.2	16.9
Gd	6.77	13.94	6.04	5.78	6.75	6.49	10.71	8.70	6.63
Hf	4.38	9.16	4.84	4.11	5.08	4.76	8.47	6.63	5.01
Ho	1.40	2.51	1.33	1.20	0.82	0.81	1.18	1.53	0.86
La	14.8	47.7	16.8	17.8	27.3	32.9	37.0	32.4	44.1
Lu	0.50	0.87	0.51	0.45	0.21	0.22	0.27	0.52	0.26
Mo	1.15	1.88	0.60	0.75	1.35	1.48	1.46	1.15	2.65
Nb	14.9	31.2	14.1	17.4	32.7	40.4	47.6	32.6	73.7
Nd	23.2	62.0	22.1	22.1	32.1	34.3	50.4	40.0	37.6
Ni†	50	11	64	61	181	170	95	21	309
Pb	24.55	9.19	2.96	4.31	2.84	2.71	3.21	4.89	3.20
Pr	4.86	14.72	4.80	4.93	7.17	8.26	11.49	9.17	9.52
Rb	22.8	49.1	21.7	31.2	10.4	16.4	17.1	39.7	10.2
Sc†	35	29	43	28	32	27	22	26	23
Sm	6.22	13.80	5.84	5.48	7.14	6.97	11.15	9.08	7.22
Sr	195	343	212	266	242	316	312	273	732
Ta	0.87	1.73	0.86	1.03	1.70	2.46	2.81	1.93	4.08
Tb	1.14	2.12	1.08	0.98	0.93	0.89	1.41	1.39	0.94
Th	1.73	5.81	2.26	2.68	2.42	3.67	4.72	5.08	5.30
U	0.45	1.34	0.63	0.73	0.75	0.88	1.05	1.42	1.38
V†	307	188	359	307	257	210	181	312	219
Y	39.3	73.0	35.8	35.1	22.8	22.6	33.7	43.4	23.6
Yb	3.50	6.12	3.34	3.11	1.49	1.52	2.02	3.62	1.84
Zn†	259	162	139	104	111	92	50	115	80
Zr	168	416	188	161	224	212	404	265	225

Major elements measured from an anhydrous powder post LOI determination, therefore the total is both anhydrous and not equal to 100

Mg# calculated on a cation basis by Mg# = 100 x Mg / (Mg +Fe^{2+}), with FeO = 0.9 x Fe_2O_{3T}

†XRF Powder Briquette analyses, all others solution ICP-MS

Appendix A - Continued

Sample	DMD157base	DMD157M	DMD158	DMD159	DMD160	DMD164M	DMD165M	DMD167
TE class.	tholeiitic	tholeiitic	tholeiitic	tholeiitic	tholeiitic	alkalic	alkalic	tholeiitic
Smp. type	sheet	sheet	dyke	dyke	sheet	sheet	sheet	sheet
Lat. (°N)	80.81927	80.81927	80.819045	80.820732	80.344299	79.61772	79.184502	80.12558
Long. (°W)	91.80291	91.80291	91.807955	91.806112	88.481716	85.786806	85.985679	85.687205
SiO_2	50.8	51.0	50.9	51.1	50.7	44.2	45.5	50.2
TiO_2	3.16	2.83	3.27	2.74	2.83	3.44	4.17	2.80
Al_2O_3	15.5	13.6	13.4	13.4	13.3	15.0	15.7	13.2
Fe_2O_{3T}	11.5	15.0	15.2	14.6	16.1	14.3	16.6	16.2
MnO	0.49	0.28	0.25	0.22	0.37	0.50	0.24	0.26
MgO	2.34	4.46	4.39	4.98	5.74	4.69	3.67	5.07
CaO	12.1	9.2	8.5	9.0	6.2	12.5	8.8	7.5
Na_2O	3.35	2.65	2.87	2.59	3.62	2.82	2.89	3.21
K_2O	0.31	0.80	1.00	0.70	0.94	1.48	1.37	1.02
P_2O_5	0.43	0.38	0.35	0.36	0.37	0.67	1.19	0.32
Total	100.0	100.2	100.1	99.7	100.2	99.5	100.1	99.8
LOI	9.01	3.25	2.58	2.75	1.26	5.81	5.40	1.67
Mg#	15	20	20	23	23	22	16	21
Ba	240	215	307	173	277	466	636	486
Ce	53.0	49.8	60.7	49.0	28.8	50.2	64.0	63.8
Co†	42	48	49	35	54	43	49	56
Cr†	46	55	43	88	64	49	92	58
Cs	0.22	0.86	1.63	0.87	0.60	1.34	1.23	1.32
Cu	60.4	56.9	49.9	56.8	37.1	6.8	26.8	183.4
Dy	8.1	7.6	8.3	7.5	4.9	5.7	6.8	8.4
Er	4.56	4.15	4.68	4.10	2.80	2.71	3.27	4.80
Eu	2.48	2.22	2.37	2.17	1.41	3.00	4.00	2.23
Ga	22.4	21.7	23.8	21.5	19.3	22.2	24.3	22.3
Gd	8.02	7.49	8.33	7.26	4.24	6.69	8.32	8.21
Hf	4.95	4.70	6.24	4.59	4.66	3.00	3.60	6.04
Ho	1.61	1.48	1.64	1.45	0.99	1.06	1.27	1.69
La	24.9	22.5	26.7	21.5	7.8	23.4	30.3	28.5
Lu	0.58	0.54	0.62	0.52	0.38	0.32	0.37	0.64
Mo	1.38	1.37	1.20	1.11	1.60	0.93	1.97	1.13
Nb	19.8	18.8	25.7	18.4	16.1	23.7	26.3	29.1
Nd	31.0	28.4	34.3	27.7	14.1	29.9	37.5	34.7
Ni†	33	26	22	25	28	27	32	40
Pb	3.78	3.67	7.11	3.80	16.40	1.28	6.47	3.69
Pr	6.90	6.43	7.79	6.14	2.94	6.52	8.05	8.04
Rb	4.0	28.1	35.7	24.6	22.7	39.4	39.4	37.9
Sc†	40	32	31	29	35	29	34	30
Sm	7.62	6.90	8.17	6.76	4.05	6.88	8.50	7.97
Sr	379	297	279	282	130	436	488	420
Ta	1.14	1.06	1.51	1.08	0.94	1.29	1.49	1.64
Tb	1.29	1.23	1.37	1.20	0.76	1.00	1.20	1.39
Th	2.93	2.76	4.82	2.67	1.25	2.68	2.30	4.40
U	0.84	0.78	1.27	0.76	0.80	0.73	1.36	1.21
V†	405	325	399	337	298	335	310	325
Y	46.1	44.5	47.0	43.7	23.5	30.3	36.5	48.0
Yb	4.04	3.72	4.20	3.64	2.60	2.22	2.62	4.39
Zn†	136	133	143	113	103	61	78	161
Zr	199	190	245	187	181	120	153	236

Major elements measured from an anhydrous powder post LOI determination, therefore the total is both anhydrous and not equal to 100

Mg# calculated on a cation basis by Mg# = 100 x Mg / (Mg + Fe^{2+}), with FeO = 0.9 x Fe_2O_{3T}

†XRF Powder Briquette analyses, all others solution ICP-MS

Appendix A - Continued

Sample	DMD168	DMD169	DMD169M	DMD172	DMD173	DMD174	DMD1	DMD2	DMD4
TE class.	tholeiitic	tholeiitic	tholeiitic	alkalic	alkalic	tholeiitic	tholeiitic	tholeiitic	alkalic
Smp. type	dyke	sheet	sheet	dyke	sheet	sheet	sheet	sheet	sheet
Lat. (°N)	80.160071	80.145786	80.145095	79.984988	80.020558	80.019962	-	78.200791	81.84212
Long. (°W)	85.801735	85.132571	85.127998	85.345178	86.383641	86.401025	-	85.263196	71.4453
SiO_2	50.4	70.0	50.8	47.7	47.2	50.8	51.1	49.7	48.0
TiO_2	2.79	0.25	3.17	3.55	3.34	3.33	2.83	4.14	3.43
Al_2O_3	13.9	15.5	14.1	14.2	14.6	12.7	14.1	13.1	14.9
Fe_2O_{3T}	15.4	1.6	14.8	15.1	14.9	16.5	13.0	14.9	13.6
MnO	0.22	0.04	0.27	0.25	0.22	0.24	0.24	0.23	0.21
MgO	5.46	0.66	2.12	5.38	5.80	4.26	5.16	5.29	7.18
CaO	7.5	0.4	10.7	7.6	8.1	8.4	10.2	7.2	7.0
Na_2O	3.07	3.50	2.59	2.99	4.00	2.60	2.42	2.96	3.97
K_2O	0.91	7.47	1.02	2.27	1.38	1.24	0.63	1.84	1.04
P_2O_5	0.36	0.04	0.39	0.67	0.63	0.41	0.30	0.57	0.57
Total	100.0	99.5	99.9	99.6	100.1	100.4	100*	100*	100*
LOI	3.28	0.87	6.78	1.72	2.15	1.71	4.14	1.65	2.88
Mg#	23	26	11	24	25	18	26	23	31
Ba	193	701	210	1719	450	250	203	549	383
Ce	50.6	14.2	61.2	53.9	49.7	67.2	38.7	59.6	58.6
Co†	52	2	45	50	52	50	61	68	61
Cr†	65	7	28	98	96	54	48	40	33
Cs	1.29	0.48	1.17	0.38	5.98	0.41	1.36	1.23	1.01
Cu	59.2	15.4	199.9	15.7	18.7	197.6	127.6	104.0	22.3
Dy	7.5	1.8	7.9	4.9	5.4	7.9	6.9	8.0	5.9
Er	4.22	1.31	4.70	2.30	2.71	4.45	3.78	4.22	2.82
Eu	2.23	0.29	1.97	2.67	2.77	2.19	2.00	2.63	2.51
Ga	21.8	16.0	22.0	21.6	20.5	21.1	21.1	22.6	24.1
Gd	7.53	1.52	7.38	5.97	6.38	8.11	6.55	8.81	7.43
Hf	4.59	10.78	6.46	3.79	2.93	6.48	4.52	5.15	4.63
Ho	1.50	0.40	1.59	0.88	1.01	1.56	1.37	1.57	1.09
La	23.0	7.7	22.2	20.1	21.5	28.6	17.8	28.0	27.1
Lu	0.53	0.23	0.61	0.27	0.33	0.57	0.53	0.49	0.32
Mo	1.21	4.51	1.85	0.32	0.87	1.71	1.56	2.05	2.24
Nb	18.0	29.5	29.3	24.6	23.0	29.5	16.5	30.8	27.0
Nd	28.4	7.3	29.6	29.0	28.7	33.7	25.6	35.4	34.4
Ni†	32	4	28	20	41	24	49	40	57
Pb	3.89	50.27	8.20	1.22	1.99	5.66	7.47	3.39	1.70
Pr	6.38	1.93	6.63	6.37	6.43	7.74	5.51	7.85	7.71
Rb	34.9	82.0	23.1	21.4	33.3	28.3	20.5	39.9	28.5
Sc†	32	2	40	24	23	28	36	32	21
Sm	6.88	1.59	7.16	6.34	6.65	7.83	6.37	8.48	7.82
Sr	235	18	226	420	389	173	266	329	466
Ta	1.02	2.33	1.54	1.41	1.33	1.49	1.29	2.09	1.79
Tb	1.20	0.28	1.25	0.90	0.98	1.33	1.08	1.39	1.07
Th	2.69	3.08	3.59	2.22	2.54	3.49	2.25	3.07	2.93
U	0.77	1.23	1.28	0.85	0.63	1.09	0.63	0.89	0.96
V†	318	7	422	297	267	353	410	411	295
Y	43.4	8.1	42.2	20.1	28.3	43.6	39.0	43.3	30.2
Yb	3.68	1.47	4.35	1.89	2.21	3.98	3.46	3.60	2.21
Zn†	147	126	105	58	74	134	119	139	106
Zr	183	471	264	151	106	271	179	212	201

Major elements measured from an anhydrous powder post LOI determination, therefore the total is both anhydrous and not equal to 100

Mg# calculated on a cation basis by Mg# = 100 x Mg / (Mg +Fe^{2+}), with FeO = 0.9 x Fe_2O_{3T}

†XRF Powder Briquette analyses, all others solution ICP-MS

*Major- and trace-elements measured at AcmeLab Vancouver and recalculated anhydrous

Appendix A - Continued

Sample	DMD17	DMD20	DMD22	DMD23	DMD24	DMD25	DMD26	DMD27	DMD28	DMD29
TE class.	tholeiitic	alkalic	alkalic	alkalic	alkalic	alkalic	alkalic	alkalic	alkalic	alkalic
Smp. type	sheet	sheet	sheet	sheet	sheet	sheet	sheet	sheet	sheet	sheet
Lat. (°N)	80.05738	81.83218	81.82236	81.85939	-	81.84212	82.00958	82.00894	82.00485	81.823433
Long. (°W)	86.42305	71.53236	71.61621	71.30683	-	71.44615	70.03373	70.00936	69.92056	71.61355
SiO_2	51.5	48.1	48.7	47.0	48.3	46.6	50.0	49.7	50.7	48.0
TiO_2	2.95	3.43	3.37	3.50	3.31	3.40	3.76	3.83	3.38	3.42
Al_2O_3	12.6	14.7	14.7	15.0	14.4	14.8	13.5	13.6	14.3	14.7
Fe_2O_{3T}	15.4	13.6	13.5	14.2	14.0	13.6	14.2	14.3	12.8	12.9
MnO	0.22	0.26	0.20	0.14	0.23	0.18	0.21	0.22	0.17	0.18
MgO	3.96	6.39	6.34	7.16	5.95	6.31	4.72	4.86	5.08	6.21
CaO	8.0	9.5	6.6	8.7	10.3	10.0	9.3	9.4	9.3	10.5
Na_2O	2.79	2.48	3.64	2.63	2.20	3.68	2.83	2.71	2.77	2.48
K_2O	1.30	1.09	2.32	1.12	0.80	0.93	1.12	1.03	0.97	0.97
P_2O_5	0.36	0.58	0.58	0.58	0.55	0.54	0.40	0.41	0.47	0.54
Total	1.3	100*	100*	100*	100*	100*	100*	100*	100*	100*
LOI	0.46	1.88	2.57	2.03	4.83	3.04	1.68	0.78	2.00	1.72
Mg#	18	29	29	30	27	29	22	23	25	29
Ba	262	444	3830	285	274	419	282	238	272	312
Ce	73.7	58.9	58.4	58.9	52.0	55.2	61.3	59.4	62.7	53.8
Co†	71	64	62	63	58	67	91	76	64	66
Cr†	20	32	31	34	30	36	26	25	40	32
Cs	1.65	0.71	14.85	1.63	0.90	24.57	1.66	0.85	0.13	0.36
Cu	196.4	42.9	42.9	18.4	41.5	35.3	41.1	42.0	51.1	43.8
Dy	9.4	5.9	5.7	5.8	5.4	5.2	5.9	5.9	6.1	5.6
Er	5.33	2.60	2.86	2.66	2.56	2.46	2.86	2.83	2.72	2.57
Eu	2.42	2.43	3.02	2.19	2.37	2.30	2.35	2.47	2.43	2.34
Ga	23.7	24.0	21.7	24.6	21.5	26.0	23.7	23.5	24.3	22.7
Gd	9.80	7.15	7.15	7.22	7.04	6.88	7.63	7.38	7.47	7.04
Hf	6.96	4.41	4.27	4.65	4.34	4.28	4.76	4.94	5.07	4.14
Ho	1.96	1.03	1.12	1.06	1.01	1.01	1.12	1.08	1.09	1.03
La	34.5	25.7	26.4	27.3	25.7	24.8	29.9	28.4	30.9	25.5
Lu	0.68	0.32	0.32	0.31	0.31	0.30	0.31	0.32	0.32	0.30
Mo	2.23	1.96	1.88	1.95	1.50	2.05	2.48	2.22	2.42	1.94
Nb	34.7	26.2	26.6	27.3	25.2	24.2	37.7	36.2	40.1	26.1
Nd	40.9	31.7	32.4	32.3	31.0	29.4	33.9	33.3	34.9	31.1
Ni†	35	51	53	56	50	59	32	32	45	58
Pb	7.17	7.09	3.12	1.16	3.23	1.82	3.18	2.92	2.75	3.51
Pr	9.75	7.35	7.70	7.69	7.08	6.89	7.68	7.38	7.90	6.83
Rb	43.8	25.3	43.3	37.0	19.9	24.6	30.9	27.9	18.1	23.4
Sc†	34	20	20	21	18	21	27	26	24	19
Sm	9.35	7.26	7.37	7.15	6.97	6.89	7.68	7.21	7.73	7.06
Sr	262	492	721	487	439	503	483	472	570	509
Ta	2.53	1.77	1.72	1.65	1.77	1.76	2.90	2.53	2.53	1.73
Tb	1.52	1.03	0.98	1.03	0.98	0.96	1.12	1.11	1.08	1.02
Th	5.32	2.94	2.77	3.14	2.98	2.80	3.12	3.17	3.01	2.81
U	1.46	0.90	0.89	0.97	0.97	0.87	0.86	0.97	0.89	0.94
V†	378	293	296	310	266	313	385	380	314	276
Y	52.3	30.2	30.0	30.5	27.3	30.5	30.9	30.5	30.9	29.0
Yb	4.86	2.23	2.24	2.19	2.11	2.05	2.19	2.15	2.18	2.15
Zn†	141	130	126	66	142	134	127	123	138	123
Zr	301	192	191	194	186	195	214	200	230	188

Mg# calculated on a cation basis by Mg# = 100 x Mg / (Mg +Fe^{2+}), with FeO = 0.9 x Fe_2O_{3T}

†XRF Powder Briquette analyses, all others solution ICP-MS

*Major- and trace-elements measured at AcmeLab Vancouver and recalculated anhydrous

Appendix A - Continued

Sample	DMD35
TE class.	tholeiitic
Smp. type	sheet
Lat. (°N)	80.79834
Long. (°W)	94.02957
SiO_2	51.2
TiO_2	2.38
Al_2O_3	14.5
Fe_2O_{3T}	13.3
MnO	0.25
MgO	5.05
CaO	9.7
Na_2O	2.63
K_2O	0.70
P_2O_5	0.24
Total	100*
LOI	0.50
Mg#	25
Ba	183
Ce	31.8
Co†	69
Cr†	29
Cs	1.20
Cu	214.6
Dy	7.2
Er	4.00
Eu	2.10
Ga	20.9
Gd	7.00
Hf	4.33
Ho	1.30
La	13.7
Lu	0.50
Mo	0.89
Nb	10.0
Nd	23.0
Ni†	47
Pb	4.25
Pr	4.70
Rb	22.9
Sc†	33
Sm	6.10
Sr	240
Ta	1.30
Tb	1.10
Th	2.40
U	0.60
V†	333
Y	35.2
Yb	3.60
Zn†	116
Zr	161

Mg# calculated on a cation basis by Mg# = 100 x Mg / (Mg +Fe^{2+}), with FeO = 0.9 x Fe_2O_{3T}

†XRF Powder Briquette analyses, all others solution ICP-MS

*Major- and trace-elements measured at AcmeLab Vancouver and recalculated anhydrous

Appendix B – Detailed sample preparation and analytical methods

B.1 Major-elements

71 volcanic rocks were analysed for major-elements. Samples were sawn into slabs 1 – 2 cm thick that ranged from 60 to 180 g. Great care was taken to saw off all sections of the sample where weathering and veins were evident. The colour of the return water was noted and aided in assessment of alteration level. Rocks that had a green water colour during sawing were deemed high in metasomatic minerals, such as chlorite, and those with a beige colour were deemed to have meteoric alteration, such as hematite. The geochemistry sample blocks were then polished with 400 grit silicon carbide paper, to remove the metallic streak marks accrued during sawing, and rinsed with deionized water. The blocks where covered with Wypall X60 and left to air dry overnight.

The coarse crushing procedure entails double wrapping the blocks with sample bags and hammering them on a steel plate. Powdered sample residue remained on the hammer and the steel plate, requiring a thorough cleaning with water and ethanol between samples. The CASP suite (DMD1 to DMD35) was powdered using a tungsten-carbide milling ring in a Shatterbox 8515 for 90 s. Tungsten contamination occurred in all samples. The UofA suite (DMD100 to -174) was crushed using a Spex alumina ceramic dish for three minutes. Between each sample run, two runs of pure quartz were used for dry cleaning. After the second cleaning run, the dish was washed in water then rinsed with ethanol.

B.2 Trace-elements

Trace-elements from 72 samples were analyzed by on a Thermo Element ICP-MS at the University of Alberta in the Arctic Resources Geochemistry Facility. 100 mg of powdered whole-rock were dissolved in rigorously cleaned Teflon beakers using a 5:1 solution of concentrated HF and HNO_3. SiF_4 is evaporated at 130°C during a 3-stage dry-down where 1 ml concentrated HNO_3 is added between each drying stage. The residual sample brought into a 5000 times dilution in 3% HNO_3 solution, with 10 ppb In internal standard. Trace-elements were analyzed

on a Thermo Element ICP-MS at the University of Alberta in the Arctic Resources Geochemistry Facility. All trace-elements were calibrated using dissolved rock standards BCR-2, BHVO-2, and BIR-1 with various dilution factors. A procedural blank was ran with each 15 samples.

Potential contamination by the alumina dish was assessed by Laser Ablation of a small chip of the ceramic dish itself (Table below). Only the notable elements are tabulated.

Trace-element	Concentration (ppm by Laser ablation)	2SE
Zr	8	12
Ba	24.5	2
Ga	8.4	0.36
Sr	1.26	0.65
Nd	0.124	0.083

B.3 Sr-Nd isotope detailed analytical methods

20 mafic samples and 2 sedimentary rocks from the Sverdrup Basin were analyzed to determine the 87Sr/86Sr and 143Nd/144Nd isotope compositions. Analysis was performed on a Thermo Triton Plus Thermal Ionization Mass Spectrometer (TIMS) at the University of Alberta in the Arctic Resources Geochemistry Facility. Ratios measured on Faraday cups with 10^{11} Ω amplifiers.

B.3.1 Sr

Drydown both Sr and Nd cuts with 1.5 µL of 0.1 M H_3PO_4. Once dried to a single drop, add 3.5 µL of TaF_5, an activator which provides better separation of Rb and Sr. Sample was pipetted onto a Re filament, at 1 A, in 3 drops, being cautious to centre the load and keep the width below 3mm. Loaded filaments were slowly raised to ~ 2 A and held while the H_3PO_4 evaporated. At his point, the TaF_5 has melted that will form a glass once cooled. After H_3PO_4 evaporation is complete, the current was raised until the filament is a dull red glow (~2.5 A) and held for 5-10 s followed by a slow reduction of current until 0 A.

Analysis entailed a slow increase in amperage to 3.2 – 3.5 A (1480 to 1500°C) enables Rb

ionization between 2.0 and 2.5 A (less than 1300°C), mitigating the effect of ^{87}Rb interference on ^{87}Sr. Ratio recording began when $^{88}Sr/^{86}Sr$ was approximately 8.33 reducing the effects of higher temperature fractionation, which preferentially ionizes the lighter ion. Ratios were measured in 20 blocks of 10 ratios, with 4s interval for each measurement. A 10s baseline and an amplifier rotation was programmed between each block

100 ng of Sr standard SRM987 was also loaded and analyzed with each turret, which has accepted ratios of 0.710246 ($^{87}Sr/^{86}Sr$) and 0.0565 ($^{84}Sr/^{86}Sr$) of Jochum et al. (2005). ~ 5ng of Sr gives approximately 2V signal of ^{88}Sr. For samples with high Rb concentrations, an interference correction is applied based on measured $^{87}Rb/^{85}Rb$. All ratios were normalized to the invariant $^{88}Sr/^{86}Sr$ (8.3752) following Thirlwall (1991).

B.3.2 Nd

150-400 ng of sample were dried down with 1.5 µL of 0.1 M H_3PO_4 and 1.0 µL of 1 M HNO_3 was added to help stabilize the emission. With the Re evaporation filament set at 1.5 A, a Parafilm 'wall' was melted onto the filament about the center, creating a 2mm wide zone for iterative sample drop loading and evaporation. This step ensured the load was centred and narrow on the filament. Once loaded, the current was increased and held at 1.8 A to evaporate the H_3PO_4, followed by a 10-20 s dull red glow at around 2.2 A. Two filaments with 200 ng of La Jolla Nd standard were loaded per turret, in the same fashion as the samples, with an accepted ratio of 0.512104 ± 10 (Jochum et al., 2005). Data acquisition by double filament outlined by Thermo (Triton Hardware manual, issue 12 2.3 – 15, 2002). With sample filament loaded into the evaporation slot of the turret, a slow increase of the evaporation filament to 1.5 – 2.0 A and the ionization filament to around 4.5 A creates a stable signal of approximately 4 V of ^{144}Nd.

All ratios were fractionation corrected to the invariant ratio $^{146}Nd/^{144}Nd$ (0.7219). ^{147}Sm interference was corrected by measuring ^{144}Sm. Since ^{142}Nd was not measured, there was no need to correct for ^{142}Ce interference.

References

Thirlwall, M.F., 1991, Long-term reproducibility of multicollector Sr and Nd isotope ratio analysis, *Chemical Geology*, v. 94, p. 85–104.

Jochum, K.P., Nohl, U., Herwig, K., Lammel, E., Stoll, B., and Hofmann, A.W., 2005, GeoReM: A new geochemical database for reference materials and isotopic standards, *Geostandards and Geoanalytical Research*, v. 29, no. 3, p. 333–338.

Appendix C – Published Cretaceous age summary (including the present study)

Table C

Fig 3.8 ID#	Sample	Source	Sample type	Location	Latitude (°N)	Longitude (°W)	Technique	Material	Age Calculation	Age ± 2σ
1	**SE 11/00B**	1	alk basalt	Hansen Point VC. SW (Phillips Inlet)	81.738	85.831 *	Ar/Ar I.H.	wr	Plateau Age	**76.6 ± 3.7**
2	**DMD143D**	2	lava flow	Elles. Audhild Bay	81.39929	90.11736	Ar/Ar I.H.	wr	Plateau Age	**78.4 ± 0.1**
3	**DMD143A**	2	lava flow	Elles. Audhild Bay	81.39863	90.10951	Ar/Ar I.H.	wr	Plateau Age	**78.8 ± 0.1**
4	**AX83-60**	3	Thol lava	Twisted Ridge, Strand Fiord	79.41667	92.28333	Laser Ar-Ar	wr	Plateau Age	**80.7 ± 1.1**
5	**434019**	4	dyke	N Greenland - Peary Land - Harebugt	83.50	34.00 *	Ar/Ar I.H.	wr	Plateau Age	**81.9 ± 1**
6	**SE 16/01**	1	alk basalt	Hansen point VC. NE (Yelverton Bay)	81.738	83.550 *	Ar/Ar I.H.	wr	Plateau Age	**82.3 ± 2**
7	**SE 74/01**	1	basaltic dyke	Hansen point VC. NE (Yelverton Bay)	81.738	82.426 *	Ar/Ar I.H.	wr	Plateau Age	**83.0 ± 1.8**
8	**BND83-016**	3	Thol lava	Bunde Fiord Section AxH	80.53900	94.81000	Laser Ar-Ar	wr	Plateau Age	**83.8 ± 1.2**
9	**434009**	4	mafic dyke	N Greenland - Peary Land - Frigg Fjord	83.50	34.00 *	Ar/Ar I.H.	wr	Isotope correlation age	**85.7 ± 4.7**
10	**PS051-041-1CC**	5	alk basalt	Alpha Ridge - dredged sample	85.51333	174.19000	Ar/Ar I.H.	plag.	Plateau Age	**89 ± 1**
11	**DMD173**	2	mafic sill	Ellesmere - Fosheim penn.	80.02056	86.38364	U-Pb TIMS	zircon/badd	$^{206}Pb/^{238}U$ w.m.	**91.7 ± 1**
12	**DMD169**	2	mafic intrusion	Ellesmere - Fosheim penn.	80.14510	85.12800	Ar/Ar I.H.	bt	Plateau Age	**91.7 ± 0.1**
13	**DMD124**	2	mafic sill	Ellesmere - Fosheim penn.	79.81344	86.41845	U-Pb TIMS	zircon	$^{206}Pb/^{238}U$ w.m.	**91.7 ± 1.1**
14	**SE 79/01**	1	hbld gabbro	Wootton Intrusive complex	82.20511	84.79928	U-Pb TIMS	zircon	$^{206}Pb/^{238}U$ w.m.	**92.2 ± 0.2**
15	**SE 33/01**	1	hbld gabbro	Wootton Intrusive complex	82.06661	85.78460	U-Pb TIMS	zircon	$^{206}Pb/^{238}U$ w.m.	**92.3 ± 0.2**
16	**AX85-074**	3	Thol lava	Artharber Creek Section AxH	80.58700	95.47400	Laser Ar-Ar	wr	Plateau Age	**92.3 ± 1.1**
17	**SE 67/01**	1	basaltic dyke	Hansen point VC. NE (Yelverton Bay)	81.738	82.426 *	Ar/Ar I.H.	wr	Plateau Age	**93.9 ± 1.3**
18	**SE 2/99**	6	Lava flow	Turnabout Gl.	82.15953	68.39447	Ar/Ar I.H.	wr	Plateau Age	**94.1 ± 4.2**
19	**SE 9/4/00**	1	basaltic dyke	Dykes in Pearya Metaseds	81.738	82.453 *	Ar/Ar I.H.	wr	Plateau Age	**94.3 ± 2.8**
20	**EL84-218**	3	sill	Tanquary Fiord Elles	82.33000	66.15250	Laser Ar-Ar	wr	Inverse Isochron	**94.4 ± 2.2**
21	**SE 17/99**	6	Lava flow	Eugenia Gl.	81.48300	76.41700	Ar/Ar I.H.	wr	Plateau Age	**94.4 ± 4.4**
22	**AX85-097**	3	Thol lava	Artharber Creek Section AxH	80.58700	95.47400	Laser Ar-Ar	wr	Plateau Age	**96.1 ± 1.9**
23	**SE 7/2/00**	1	basaltic dyke	Dykes in Pearya Metaseds	81.738	82.061 *	Ar/Ar I.H.	wr	Plateau Age	**96.6 ± 1.6**
24	**EL84-50**	3	sill (same)	Piper Pass - Same unit re-dated	82.21660	68.28333	Laser Ar-Ar	wr	Plateau Age	**97.2 ± 1.4**
25	**SE 15/99**	6	Lava flow	Eugenia Gl.	82.33000	66.15250	Ar/Ar I.H.	wr	Plateau Age	**97.9 ± 4**

*location determined from approximate published map position geolocated on Google Earth; Ar/Ar I.H. -$^{39}Ar/^{40}Ar$ incremental heating; w.m. - weighted mean; wr - whole-rock; badd - baddeleyite; TIMS - Thermo ioniz SHRIMP - sensitive high-resolution ion microprobe. ID# related to figure 3.8, in increasing age. U-Pb age from DMD169 omitted, as Ar/Ar age determination of the same unit is more a reliable estimate of emplaceme

1 – Estrada and Henjes-Kunst, 2013
2 – This study
3 – Villeneuve and Williamson, 2006
4 – Kontak et al., 2001
5 – Jokat et al., 2013
6 – Estrada, 2015
7 – Evenchick et al., 2015
8 – Corfu et al., 2013

Appendix C – *Continued*

Fig 3.8 ID#	Sample	Source	Sample type	Location	Latitude (°N)	Longitude (°W)	Technique	Material	Age Calculation	Age ± 2σ
26	**SE 42/99**	6	Lava flow	Piper Pass	82.14528	67.98681	Ar/Ar I.H.	wr	Plateau Age	**97.9 ± 4**
27	**SE 12/99**	6	Lava flow	Lake Hazen	81.953	70.948 *	Ar/Ar I.H.	wr	Plateau Age	**98.2 ± 4**
28	**C 107586**	6	Lava flow basalt	Mokka Fjord	79.570	87.486 *	Ar/Ar I.H.	wr	Plateau Age	**100.7 ± 5.8**
29	**SE 154/01**	1	basaltic dyke	Dykes in Pearya Metaseds	81.738	83.888 *	Ar/Ar I.H.	wr	Plateau Age	**109.4 ± 3**
30	**DMD154**	2		Ellesmere	81.56494	91.35716	Ar/Ar I.H.	wr	Approx. Plateau Age	**116 ± 3**
31	**DMD147**	2	mafic sill	Ellesmere - otto/hare fjord	81.09125	85.75994	U-Pb TIMS	zircon	$^{206}Pb/^{238}U$ w.m.	**116.8 ± 1.8**
32	**DMD160**	2	mafic sill	Axel Heiber Is. - Schei Penn.	80.34430	88.48172	U-Pb TIMS	zircon	$^{206}Pb/^{238}U$ w.m.	**120.3 ± 0.8**
33	**11EP062A01**	7	diabase sill	Ellef Ringnes Is.	78.82280	103.88130	U-Pb TIMS	badd	Concordia	**120.8 ± 0.8**
34	**DMD145**	2	mafic sill	Ellesmere - otto/hare fjord	81.06050	86.83959	U-Pb TIMS	zircon	$^{206}Pb/^{238}U$ w.m.	**121.1 ± 1.9**
35	**1893**	8	mafic sill	Franz Josef Land - Severnaya borehole	81.14917	64.41167	U-Pb TIMS	badd	$^{206}Pb/^{238}U$ w.m.	**121.5 ± 0.3**
36	**SE 158/01**	1	basaltic dyke	Dykes in Pearya Metaseds	81.738	83.888 *	Ar/Ar I.H.	wr	Plateau Age	**122.0 ± 2.4**
37	**2944**	8	mafic sill	Franz Josef Land - Severnaya + Nagursakaya boreholes	80.77778	47.70833	U-Pb TIMS	zircon	$^{206}Pb/^{238}U$ w.m.	**122.2 ± 1.1**
38	**1902 + 1895 (mean age)**	8	mafic sill	Franz Josef Land - Severnaya borehole	81.14917	64.41167	U-Pb TIMS	zircon	$^{206}Pb/^{238}U$ w.m.	**122.7 ± 0.3**
39	**7A**	8	mafic sill	Svalbard - Linnevatnet sill	78.03374	13.88448	U-Pb TIMS	zircon	$^{206}Pb/^{238}U$ w.m.	**123.9 ± 0.3**
40	**1AX**	8	mafic sill	Svalbard - Diabasodden	78.35920	16.16560	U-Pb TIMS	zircon	$^{206}Pb/^{238}U$ w.m.	**124.5 ± 0.2**
41	**10EP001B01**	7	gabbro (evap dome)	Ellef Ringnes Is.	78.94944	101.01944 *	SHRIMP	zircon	$^{206}Pb/^{238}U$ w.m.	**126.6 ± 1.2**
42	**AX85-037**	3	dyke	Lightfoot River AxH	80.69900	92.30200	Laser Ar-Ar	wr	Plateau Age	**128.2 ± 2.1**

*location determined from approximate published map position geolocated on Google Earth; Ar/Ar I.H. -$^{39}Ar/^{40}Ar$ incremental heating; w.m. - weighted mean; wr - whole-rock; badd - baddeleyite; TIMS - Thermo ioniz
SHRIMP - sensitive high-resolution ion microprobe. ID# related to figure 3.8, in increasing age. U-Pb age from DMD169 omitted, as Ar/Ar age determination of the same unit is more a reliable estimate of emplaceme

1 – Estrada and Henjes-Kunst, 2013
2 – This study
3 – Villeneuve and Williamson, 2006
4 – Kontak et al., 2001
5 – Jokat et al., 2013
6 – Estrada, 2015
7 – Evenchick et al., 2015
8 – Corfu et al., 2013

Appendix D – Detailed analytical methods

D.1 U-Pb

Sample weight varied between 600-800 g. Samples were coarse crushed by hammer and steel plate. To reduce the potential of cross-contamination, the samples were double wrapped in thick plastic sample bags before hammering and all parts were vacuumed between samples. A fine powder was produced after a 3 minute run in a shatterbox, liberating the Zr-bearing minerals while leaving them intact. This fine powder was then mixed in water with a mild detergent to disaggregate clay size particles from grains of interest and then added slowly (300 g/h) to a Wilfley Table, to obtain a heavy mineral separate. The heavy mineral concentrate was then dried, passed through a disposable nylon sieve (70 mesh) and further segregated based on magnetism in a Frantz Isodynamic Separator. The non-magnetic fraction was subsequently separated based on grain density using methylene iodide (3.33 g/cm^3), resulting in a final concentrate that contains the Zr-bearing minerals. Zircon and baddeleyite grains were hand-picked at high magnification using a microscope.

D.2 Ar-Ar

The 5 mg biotite concentrate was hand-picked by microscope. For the whole-rock samples, the alteration rinds and diagenetic veins were sawn off to produce a sample weight of 250 g. These blocks were polished with 400 grit sandpaper to remove markings left by the steel saw blade and sent to the Oregon State University Argon Geochronology Lab. There, the whole-rock samples were crushed and all samples were enclosed in copper foil, sealed in an evacuated quartz tube and placed in the core of a TRIGA reactor for neutron irradiation. Once the ^{39}K has been irradiated to ^{39}Ar, the K/Ar isotopic ratio can be measured in a single analysis using a noble gas mass spectrometer. The biotite sample was measured on an MAP 215-50 mass spectrometer, along with the FCT-NM biotite standard to monitor flux and step heated using a low-blank, double-vacuum Heine furnace. Whole-rock samples were measured on an AEI MS-10S mass spectrometer and heated inductively with a radio frequency coil. Isotopic ratios were analyzed over 38 heating steps (41 for single phase biotite).